POLITECNICO DI TORINO

Master's degree in Biomedical Engineering (Bionanotechnologies)

Master's Thesis

Fighting cancer relapse with remote activation of nanoconstruct: preliminary screening of possible solutions for an extracorporeal circulation set-up

Supervisor:

Prof. Valentina Alice Cauda

Candidate:

Roberto Ruffinello

263370

Academic Year: 2020/2021

Contents

List of Figures

List of Tables

Abstract

Cancer relapse is a leading cause of death nowadays, which brings related health and financial costs. The XtraUS European project, in which this Master Thesis is inserted, aims at developing a device to treat circulating cancer cells in the bloodstream responsible for tumour recurrence. The core idea is the application of an extracorporeal blood circulation technology in which the combination of a stimulus with responsive and targeted nanoconstructs can lead to the formation of toxic species able to kill circulating tumour cells.

The aim of the work is the study of this energetic stimulation on nanoconstructs and its consequences in different static experimental set-up, in order to test an already approved device, but also the disclosure of possible arrangements for the future development of a cartridge for blood treatment. Both experimental studies with an ad-hoc set-up and targeted numerical simulations were run, and results were used to validate experimental data.

The two techniques analysed revealed similar results that permitted to do a first screening of different experimental set-up. As a consequence, a commercially available cartridge and relative silicone tubes tested were abandoned for moving to the polystyrene single well. A deeper investigation on this set-up showed the importance of: solution volume and related height, thicknesses of the material and presence of a cover. Furthermore simulations helped to understand the energy field distribution in the well.

This work represented a preliminary study for the XtraUS European project helping to decide the right path for the development of the upcoming technology. The future perspectives are represented by the dynamic condition testing on the already studied single well as well as in alternatives settings.

1 Introduction

1.1 XtraUS European Project

The present Master Thesis is inserted in the context of the European Project – XtraUS, which focuses on the prevention of cancer relapse and on the development of an early cure of recurrence. Nowadays, many patients unfortunately get into primary tumour recurrence because their tumour is not completely remitted and they require further treatments that have consequences on their health and related costs. A major role in the disease relapse is played by circulating tumour cells (CTCs) in the blood stream, which have been considered a crucial factor in metastasis, recurrence and a primary cause of deaths for cancer (Lin, 2018). However, CTCs main challenge is their low number among all the other cells in the blood stream and lymphatic system, which makes them difficult to detect using conventional laboratory tests. For this reason, trying to fight these cancer cells has huge impact not only on cancer relapse prevention and health, but also on financial costs, quality of life and overall cancer treatment expenditure.

XtraUS project aims at validating a breakthrough technology to fight CTCs in the bloodstream by the application of an extracorporeal blood circulation set-up combined with a novel stimuli-responsive, targeted and non-immunogenic nanoconstruct, remotely activated against CTCs. The result is a personalized and translational approach, with the following advantages: high-target specificity and reduced side effects to both human tissues and blood. They represent the step forward with respect to conventional CTCs treatments, because they offer high effectiveness and safety for the proposed technology, essential requirements for the development and consequent validation of a new biomedical technology. Moreover, the first treatment offered to patients for their primary tumour disease can be made efficacious and permanent, in combination with a reduction of all associated costs.

1.2 Extracorporeal circulation techniques: parameters study

As a starting point, technologies and devices currently available in clinics for the extracorporeal treatment and/or circulation of blood were analysed, in order to obtain technical parameters that can be useful for the following sizing and development of the device/cartridge for the project. Strategies for blood extracorporeal circulation can be grouped into four categories: haemodialysis, cardiopulmonary bypass, apheresis and autotransfusion. For all the technologies, a brief scheme of the circuit and main parameters will be discussed in this section.

1.2.1 Haemodialysis

Haemodialysis is the process of nephropathic patient blood purification using a device called "artificial kidney". The patient is connected to the device via two different needles, one for the extraction and one for the re-entry of the blood; they can be inserted in a peripheral zone on the arm, or centrally though a venous catheter in the right atrium. The extracted blood, through a peristaltic pump with fixed flow rate, reaches the dialyser where the purification occurs thanks to the semi-permeable membrane that separates the blood from the dialysate.

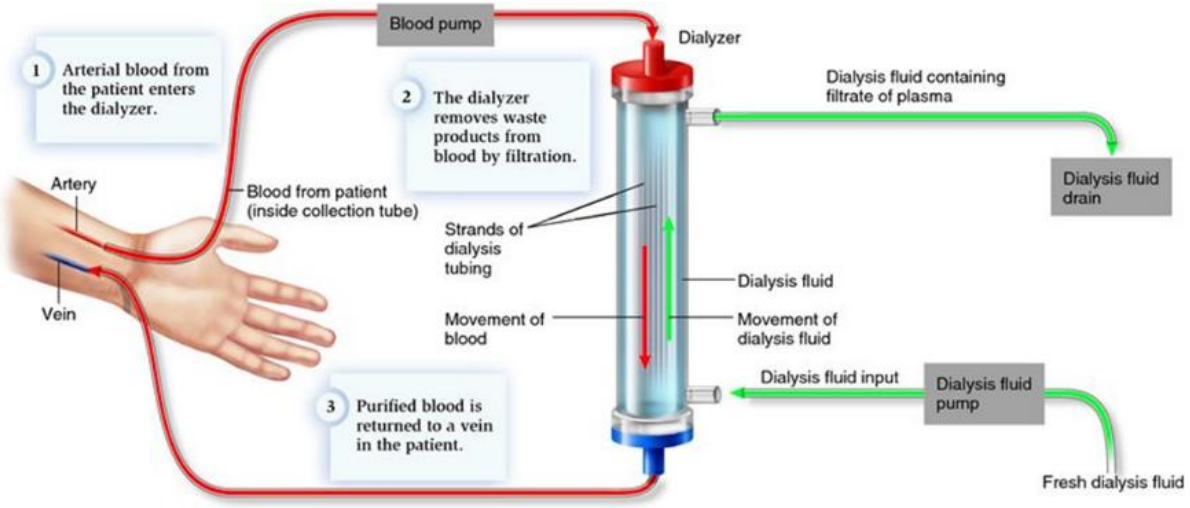

Figure 1.1: Scheme of haemodialysis circuit (BiologyForums, 2020).

The device consists in two circuits: the haematic side (red pipes in Figure 1.1) made of disposable materials, and the dialysate side (green pipes in Figure 1.1), which is embedded in the machine and its study is out of the scope of this research. A focus on the blood side of the device is shown in Figure 1.2, which is composed by arterial delivery line, sensors for the monitoring of arterial and venous pressure, peristaltic pump, heparin pump or syringe, dialyser, venous return line, air bubble detector and automatic clamp for interrupting the flow on venous return line (Misra, 2005).

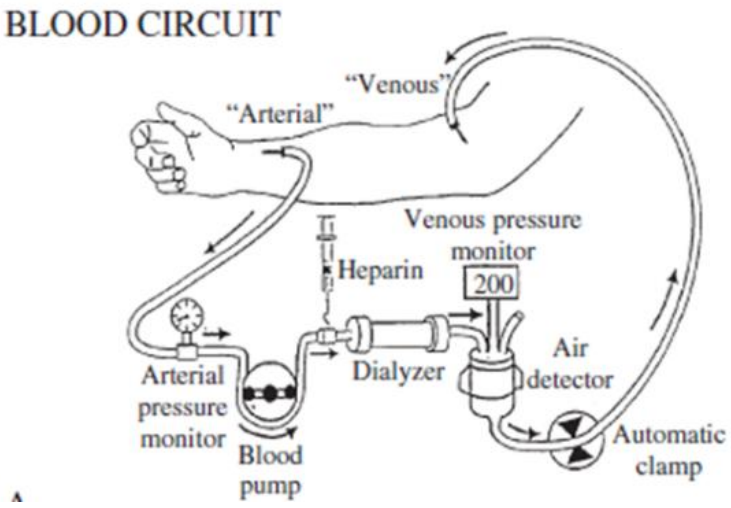

Figure 1.2: Scheme of the blood side of haemodialysis circuit (Misra, 2005).

The circuit's tubes materials must be biocompatible, haemocompatible and non-toxic, for these reasons most used materials are: silicon, poly(vinyl chloride) (PVC) and Tygon. Silicon is used mainly for the pump segment of the tube for many reasons: mechanical, minimization of clot formation risk and geometry maintenance upon temperature. Unfortunately, it is more expensive than PVC, in fact the latter is used for all the blood lines, with the drawbacks of possible phthalates release. Finally, Tygon is a polymeric material whose composition is not well described because it is a particular brand, for this reason not commonly used (Misra, 2005) (Ippoliti, 2019).

Table 1.1: List of bloodlines with identification data, abbreviation, internal diameter and thickness (adapted from (Ravagli, 2018)).

Manufacturer	Model Name	Composition Information (from Package)	Abbreviation	Internal Diameter (mm)	Thickness (mm)
B.Braun Avitum AG (Germany)	A/V Set	DEHP-FREE PVC	BB	4.83	1.00
Bellco (Italy), now part of Medtronic (USA)	Extracorporeal Bloodlines	PVC V 326-1/F	BE	4.37	1.20
Gambro Dasco S.p.a (Italy), now part of Baxter (USA)	ArtiSet	DEHP-FREE	BG	4.27	1.17
Fresenius Medical Care (Germany)	LifeLine Beta AV-Set	-	FC	4.1	1.17

	ONLINEplus BVM 5008-R				
EffeEmme Fabbricazioni Medicali (Italy)	DiaLine	DEHP-FREE	FM	4.9	1
GAMA Group (Czech Republic)	Standardline DIS 06-16 UNIV	DEHP-FREE (pump segment)	GA	4.5	1.17
NIPRO Corporation (Japan)	NIPRO Set	DEHP-FREE	NI	4.33	1.13
ANGIPLAST PVT. LTD. (India)	Blood Line for Haemodialysis	-	-	4.8	2
Perfect Medical Co. Ltd. (Taiwan)	Hemodialysis Blood Tubing Set	Non-DEHP, Medical grade PVC Tubing	-	4.6	2.2
Tradewinds (Taiwan)	Hemodialysis Blood Tubing Set-1	-	-	4.6	2.2

Table 1.1 shows some of the main tubes manufactures with important characteristics: the most useful for this research is the internal diameter, which has a range between 4.1 and 4.9 mm.

Blood flow rates have differences depending on the country in which haemodialysis is performed, but they are always between 200 and 400 mL/min (Misra, 2005) (Chang, 2016), and time of treatments are around 4 hours per 3 treatments a week following guidelines for haemodialysis (Table 1.2).

Table 1.2: List of blood flow rate and time of treatment for haemodialysis extracted from literature research.

Bibliographic reference	Blood flow rate (mL/min)	Time of treatment (h)
(Chang, 2016)	250 ± 32	5
(Hassell, 2001)	200, 300, 400	3.7 ± 0.4
(Rafik, 2018)	250, 350	4

1.2.2 Cardiopulmonary bypass

Cardiopulmonary bypass (CPB), also known as extracorporeal circulation (ECC), is the technique in which the heart-lung machine temporarily replaces heart and lungs functions during cardiac surgery procedures, in order to maintain the circulation of blood and oxygenation

content of the patient's body. The blood is collected before it reaches the right side of the heart and it is directed towards an oxygenator through cannulas and tubes, to finally be reinjected into the patient's arterial system.

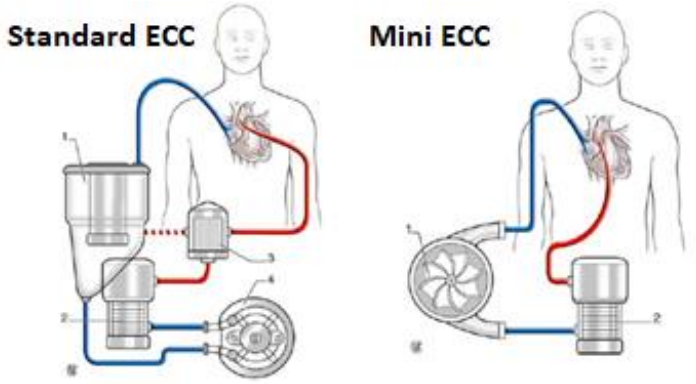

Figure 1.3: Standard ECC (1. Venous reservoir, 2. Oxygenator, 3. Arterial filter, 4. Roller pump). Mini ECC (1. Centrifuge pump, 2. Oxygenator) (Alexandre, 2010).

Minimal extra-corporeal circulation (MECC) was born for reducing trigger volume and air-blood contact to lower inflammation response, but the core idea of the circuit is the same. In details, a CPB circuit is composed by a pump (roller or centrifugal), cannulas that connect patient and circuit, an oxygenator and tubing.

Most diffused blood tubing materials are PVC, that offers durability and acceptable haemolysis rate, and silicone, mostly used in the pump segment (Sarkar, 2017) (Washington, DC: U.S. Patent No. 7,291,124, 2007). In a typical commercialized tubing set for blood handling system (Washington, DC: U.S. Patent No. 7,291,124, 2007), venus, arterial and pump line have dimensions of ½ and 5/8 inches (12.7 and 15.88 mm respectively). In order to improve interconnections between the different components of the set, the inventors proposed a reduction in internal diameters up to 3/8 inches (9.53 mm).

Table 1.3 and Table 1.4, based on clinical studies, show inner diameters of tubing and CPB time used for conventional ECC (Table 1.3) and mini ECC (Table 1.4).

Table 1.3: List of tubing ID and time of treatment for standard ECC extracted from literature research.

Bibliographic reference	Tubing ID	CPB time (min)
(Bennett, 2013), (Santambrogio, 2009), (Junior, 2017)	½ inches = 12.7 mm	68
(Santambrogio, 2009),	3/8 inches = 9.53 mm	87 – 90

(Junior, 2017), **(Wippermann, 2005)**		

Table 1.4: List of tubing ID and time of treatment for mini ECC extracted from literature research.

Bibliographic reference	Tubing ID	CPB time (min)
(Wiesenack, 2004)	3/8 inches = 9.53 mm	79 – 86
(Golab, 2007), **(Hickey, 2006)**	¼ inches = 6.35 mm	76 – 91
(Hickey, 2006)	3/16 inches = 4.76 mm	/
(Hickey, 2006)	1/8 inches = 3.18 mm	/

Flow rates values depend on the context of use of the technology and many other factors, among which the most important is the body surface area. Following guidelines for normothermic patients to approximate a normal cardiac index, the blood flow rates are between 2.2 and 2.5 L/min/m^2 (Alexandre, 2010) (Murphy, 2009).

1.2.3 Apheresis

Apheresis is an extracorporeal medical technology in which the blood of a person is flowed through an apparatus that separates out one particular constituent in order to treat it, and then returns the treated blood to the circulation. Depending on the component collection, we can distinguish between plasmapheresis, erythrocytapheresis, plateletpheresis and leukapheresis.

The most used blood tubing material is PVC (U.S. Patent No. 11/662,354, 2008) and dimensions are around 3 mm of internal diameter (Washington, DC: U.S Patent No. 3,489,145., 1970). Blood flow rates used are between 50 and 100 mL/min (Mustieles, 2020) and times of treatment between 3 and 6 hours.

A specific leukapheresis approach called photopheresis is currently approved by FDA for the treatment of Cutaneous T-cell lymphoma (CTCL) and in this case the blood is extracorporeally exposed to the combination of UV radiation and a small molecule that acts as photosensitizer (Figure 1.4). This kind of treatment results to be very similar to the one proposed in the XtraUS project, so that a specific focus on this technology will be considered in this dissertation.

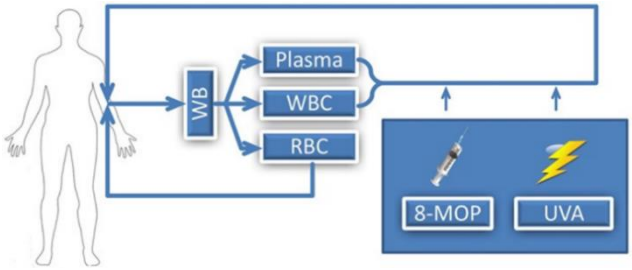

Figure 1.4: Scheme of Extracorporeal Photopheresis treatment (Cho, 2018).

The photopheresis blood tubing (from COBE Spectra essential guide) have dimensions of 0.113 inches (2.87 mm) and a list of studies reporting information about flow rates and times of treatment are summarized in Table 1.5.

Table 1.5: List of flow rates and time of treatment values for photopheresis, extracted from literature research.

Bibliographic reference	Device	Flow rate (mL/min)	Time of treatment (min)
(Edelson R. B., 1987)	Therakos	/	270
(Garban, 2012)	COBE Spectra	/	180
(Schooneman, 2003)	Therakos UVAR XTS	/	180
(Piccirillo N. P., 2018)	COBE Spectra OPTIA Spectra	40	/
(Piccirillo N. P., 2019)	Therakos Cellex	30/40	94
(Rangarajan, 2013)	Therakos Cellex	5/50	60-205
(Klassen, 2010)	Therakos UVAR XTS Therakos CELLEX	/	180 75/100

1.2.4 Autotransfusion

Autotransfusion is a process where a person receives his own blood for a transfusion, instead of banked allogenic blood. It is usually carried out during surgical procedures using a device for blood recover.

The circuit starts with a double lumen cannula for blood sampling from the surgical site and anticoagulant addition. The blood is then filtered to remove large debris and collected in a reservoir. Erythrocytes are separated by centrifugation and returned to the patient with high haematocrit.

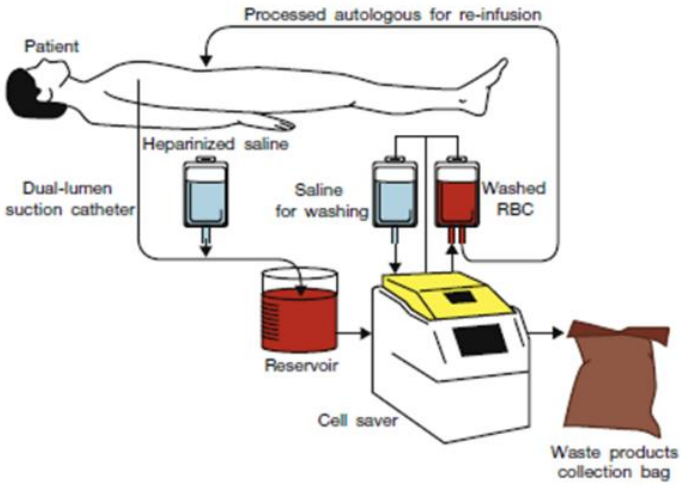

Figure 1.5: Scheme of autotransfusion treatment (Swift, 2019).

Tubing are in PVC and dimensions are between ¼ and 3/8 inches, 6.35 and 9.53 mm respectively (from XTRA brochure). Table 1.6, built from a literature research, shows flow rate values in the range 200 – 600 mL/min and times of treatment in the order of minutes.

Table 1.6: List of devices, flow rates and time of autotransfusion treatment extracted, extracted from literature research.

Bibliographic reference	Device	Flow rate (mL/min)	Time of treatment (min)
(Serrick, 2003)	Autolog	250 – 600	3.8
(Serrick, 2003), **(Warnock, 1982)**	Sequestra	300	6.1
(Serrick, 2003), **(Warnock, 1982)**	Cell Saver	300	4.4 8 – 10
(Serrick, 2003), **(Wang, 2012)**	CATS	210	10
(Serrick, 2003)	BRAT	200	6.1
(Yarham, 2011)	XTRA	350 – 400	/

To conclude this section, Table 1.7 summarizes the ranges of most useful parameters regarding extracorporeal circulation technologies.

Table 1.7: Summary of parameters ranges for extracorporeal circulation technologies.

	Tubing materials	***Tubing ID (mm)***	***Blood flow rate (mL/min)***	***Time of treatment (min)***
Hemodialysis	PVC Silicone	4.1 – 4.9	200 – 400	240 – 300
ECC	PVC Silicone	3.18 – 12.7	2200 – 2500	68 – 91
Apheresis	PVC	2.87 – 3.18	5 – 100	75 – 360
Autotransfusion	PVC	6.35 – 9.53	200 – 600	3.8 – 10

As a conclusion of this starting research: apheresis, and in particular photopheresis, resulted to be the most interesting treatment because it is very close to the aim of this project. Hence, a more detailed investigation on this technology will be presented in the following sections.

1.3 Extracorporeal photopheresis

In this section, an overview on extracorporeal photopheresis (ECP) technology will be presented, in order to understand the basic principles and gain information about technical aspects, with a special focus on the sterile cassette in which the irradiation occurs.

1.3.1 Procedure

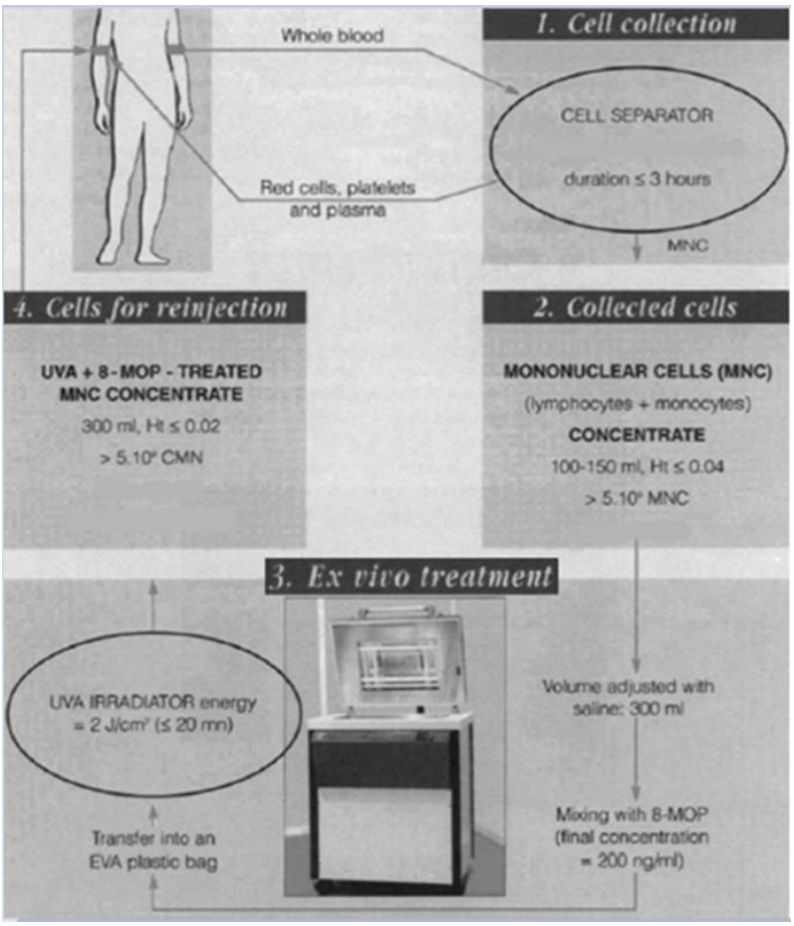

Figure 1.6: Scheme of the off-line ECP technique (adapted from (Schooneman, 2003)).

ECP is a three-steps procedure (Schooneman, 2003) (Knobler R. &., 2003), as described in detail on the following.

1. **Leukapheresis**: the blood is extracted from the patient by intravenous access and mixed with heparin or acid citrate dextrose (ACD), which is a solution of citric acid, sodium citrate and dextrose in water. Their functions are: anticoagulation along the extracorporeal circuit and prevention of clot formation inside the extracorporeal tubes, allowing a continuous and not obstructed flow of the treated blood. Then, mononuclear white blood cells (WBC) are separated from red blood cells (RBC) and plasma through

centrifugation inside a Centrifuge Bowl, leading to the formation of a leukocyte-enriched solution called buffy coat.

2. **Photoactivation**: WBCs undergo the following processes.
    2.1 Dilution with saline solution (NaCl in water), added with a volume in the range of 100 – 300 ml. The main function is to keep final haematocrit fraction in the collected WBCs below 2.5 ± 1 %, because RBCs can interfere and block UVA radiation on WBCs, thus decreasing the efficacy of the process.
    2.2 Mixing with photosensitizer 8 – MOP (8 – methoxypsoralen).
    2.3 Collection in a separate plastic bag (off-line technique) or made to flow in a sterile cassette (in-line technique),
    2.4 Irradiation by ultraviolet A light (UV-A: 315 - 400 nm) at irradiance of 1.5 – 2 J/cm^2 per WBC. During this step, 8-MOP is photoactivated by UVA and mechanisms of action take place inducing diseased WBCs to apoptosis.
3. **Reinfusion**: all blood components with the treated WBCs are returned to the patient.

Leukapheresis is repeated for a predetermined number of cycles (3 – 6), depending on patient's haematocrit and body weight, with the purpose of obtaining the right volume of buffy coat. Photoactivation and reinfusion are applied just one time at the end of leukapheresis cycles.

1.3.2 8-MOP: the photosensitizer

8-MOP (Methoxsalen, 8-Methoxypsoralen) is a naturally photoactive organic compound that belongs to psoralens. It is found in plants and the chemical structure is the following.

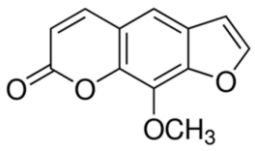

Figure 1.7: 8-MOP chemical structure.

Besides the use in ECP, it was exploited in photochemotherapy as phototoxic drug to treat cutaneous diseases. The maximum photoactivation activity is in the UVA range 330 – 360 nm with irradiance uniformity, both in horizontal and vertical direction. Metabolism is easy and rapid because approximately 95% of the drug is excreted in the urine within 24 hours after the injection. The conservation should be done at temperature of 25 °C, with excursion permitted in the range 15 – 30 °C (rxlist, 2020).

Two kinds of administrations are possible (Knobler R. &., 2003):

- Oral administration is the old and yet surpassed method based on 10 mg capsules. The maximum photoactivation effect occurs at 1.5 – 6 hours after the administration with a high individual variability, for this reason UVA irradiation is made after about 2 hours the drug has been administered. The dosage recommended to reach a minimum concentration in blood of 60 ng/mL after 1.5 hours is 60 – 200 ng/mL. Unfortunately, this kind of administration brings many side effects such as nausea, gastrointestinal toxicity, and unpredictable intaken amount of drug in blood due to high individual absorption variability.
- Extracorporeal administration is the currently used method, approved by FDA in 1999, based on a liquid formulation of 8-MOP called UVADEX (produced by Therakos), which is added directly to the collected buffy coat before irradiation.

1.3.3 Mechanisms of action and side effects

Although ECP has been in clinical use for more than 30 years, the precise mechanisms of action are not yet fully elucidated and it is still and area of ongoing research. Principle modes of action emerged from experimental data are briefly summarized below (Goussetis, 2012) (Knobler R. B., 2009) (Knobler R. B.-P., 2014).

1. The combination of 8-MOP and UVA induces psoralen-mediated DNA crosslinks with pyrimidine bases in nucleated cells, which causes the proliferative arrest by apoptosis within 48 hours after the irradiation. Given that only a small percentage (5 – 10 %) of the total blood lymphocytes are treated in a single procedure, the beneficial effects of ECP could not be attributed only to cell death.
2. During the treatment, monocytes differentiate towards dendritic cells that are capable to recognise and attack reinfused apoptotic lymphocytes that present particular antigens.
3. Immunomodulatory effect due to the migration of dendritic cells to lymph nodes and subsequent activation of a specific immune response against the particular population of diseased T lymphocytes.

Besides mechanisms of action of ECP, adverse effects should be taken into account in order to understand the therapy tolerability. The most important side effect was related to the oral 8-MOP administration, which caused nausea, and it was eliminated when extracorporeal administration was introduced (Knobler R. &., 2003). Additionally, rare cases of hypotension were reported (Knobler R. B., 2009), and a few patients may experience mild anaemia and/or

thrombocytopenia (Knobler R. B.-P., 2014). It should be noted that some patients are not suitable for ECP treatment, including those with: high sensitivity to psoralens, comorbidities that may result in photosensitivity, aphakia, pregnancy and low haematocrit values.

In conclusion, ECP treatment is considered well tolerated from World Health Organization, that declared the absence of III (severe) and IV (potentially life threatening) side effects. Efficacy and safety of this treatment justify its worldwide expansion and make it advantageous respect other chemotherapeutic and immunosuppressive agents.

1.3.4 Clinical applications

After FDA approval in 1988, many international organizations have produced clinical guidelines on ECP applications, schedule times, duration, response assessments and recommendations. In particular, the literature shows a high number of guidelines and works on CTCL treatment, which demonstrate its major efficacy against that disease with respect to others. Some relevant examples are the following:

1. the European Organization for Research and Treatment of Cancer (EORTC) in 2006 recommended ECP for the first - line treatment of Mycosis Fungoides (MF) and Sézary Syndrome (SS), the most common expressions of CTCL;
2. The UK Photopheresis Expert Group in 2008 recommended ECP for the treatment of patients with stage - III CTCL.

Moreover, ECP has shown promising efficacy against many other difficult-treating diseases, both dermatological and non - dermatological ones, such as Graft versus Host Disease (GVHD), autoimmune diseases like Chron disease, non cutaneous T – cell lymphoma, organ transplant rejection and type 1 diabetes mellitus. Some related guidelines are the following:

1. German, Austrian, Swiss consensus conference on ECP: in 2011 recommended ECP as second - line therapy for chronic GVHD in steroid - refractory patients;
2. British Photodermatology Group and UK Skin Lymphoma Group: supported ECP in cardiac rejection;
3. American Society for Apheresis (ASFA): in 2013 suggested ECP to be appropriate in lung transplant rejection.

This versatility towards other different diseases is due to its safeness and absence of significant side - effects, infections and toxicity (differently from the corresponding standard therapies),

so that it can be applied even to very low body weight or critical conditions of patients (Knobler R. B.-P., 2014).

There are still some unresolved issues not addressed by the guidelines, including the determination of leukocyte count at the time of WBCs extraction and the relation between number of extracted cells and patient response. Additionally, the absence of well – defined treatment schedule (frequency) and duration, which are mostly based on clinical response; contraindication in patients with total leucocyte count below 1 x 10^6/mL and the relatively high cost are other controversial arguments (Perotti, 2015).

1.3.5 Clinical applications: focus on Cutaneous T-Cell Lymphoma (CTCL)

CTCL is a group of tumours of the immune system developing the accumulation of malignant T – cell population, initially circulating along the peripheral blood, towards the cutaneous environment. Curative therapies are not available and treatments objectives are long term remission or palliation. ECP is one of them and it is applied as alternative to skin – directed psoralen and UVA treatment (PUVA) because safer and recommended as first – line treatment for SS CTCL. It can be used as monotherapy or more efficacious in combination with other therapies to increase complete responses and remissions. When ECP is used as monotherapy, there are some characteristics identifying the best responding patients: WBC count lower than 20.000 mm^{-3}, killer cells activity close to normal, number of cytotoxic T – cells close to normal and plaques not covering more than 10 – 15% of the total skin surface. On the other hand, ECP can be applied in synergistic combination with chemotherapy, biological responding modifiers (e.g. interferon IFNα-2b) or irradiation techniques (e.g. PUVA or total skin electro beam therapy-TSEB) (Knobler R. &., 2003).

For the treatment schedule, ASFA guidelines represents the reference point, even if there is not a clear shared optimal therapy schedule. Some guidelines recommend a starting schedule of one cycle (i.e. two consecutive days) every 2 weeks for the first 3 months, then reduction to once monthly; while other guidelines recommend one cycle every 2 – 4 weeks, followed by a cycle every 4 – 8 weeks in case of complete response. Based on clinical experience, it has been recognized that an increased frequency of treatment could give benefit in patients with worsening diseases (Knobler R. B.-P., 2014).

Regarding the treatment duration, the recommendations are at least 6 months, with differences between responding and not responding patients: in the first, treatment must not be stopped and

must be prolonged for more than 2 years, while in the latter, ECP must be stopped as monotherapy and combined with other therapies (Knobler R. B.-P., 2014).

Response assessment should be performed every 3 months and it is recommended to wait for at least 6 – 12 months of treatment before concluding that ECP is not effective, because responses can be observed after a relatively long time after first treatment (Knobler R. B.-P., 2014).

An exhaustive list of recommendations, treatment regime and monitoring for the variety of T – cell mediated diseases is reported in Table 1.8.

Table 1.8: Recommendations on the use of ECP in different diseases (Knobler R. B.-P., 2014).

Condition	Patient selection	Treatment schedule	Maintenance treatment	Response assessment
Cutaneous T-cell lymphoma (mycosis fungoides, Sézary syndrome)	First-line treatment in erythrodermic stage IIIA or IIIB, or stage IVA1-IVA2	One cycle every 2 weeks initially, then every 3–4 weeks Continue treatment for 6–12 months for response evaluation	Treatment should not be stopped, prolonged for >2 years (treatment intervals up to 8 weeks)	To be performed every 3 months Wait for at least 6 months of treatment before concluding that ECP is not effective
Chronic graft-versus-host disease	Second-line therapy individual clinical settings may justify first-line treatment	One cycle every 1–2 weeks for 0–12 weeks	After 12 weeks, treatment intervals could possibly be increased by 1 week every 3 months	Disease should be monitored according to the NIH guidelines
Acute graft-versus-host disease	Second-line therapy in pts refractory to corticosteroids (2 mg/kg/day) and calcineurin inhibitors	Weekly basis, two to three treatments per week	Discontinue ECP in patients with CR No evidence that maintenance is beneficial	Every 7 days with staging according to published criteria
Solid organ transplantation (lung)	Salvage therapy for lung transplant rejection when conventional therapies do not produce an adequate response	One cycle every 2 weeks for the first 2 months, then once monthly for 2 months (total of 6)	If clinical stabilization occurs with ECP, long-term continuation might be warranted to maintain the clinical response	Pulmonary function test (FEV1 value) Successful treatment defined as FEV1 stabilization or slowing decline
Scleroderma	Second-line or adjuvant therapy in mono- or combination therapy ECP should be considered to treat skin, but not organ, involvement	One cycle every 4 weeks for 12 months	Increase the intervals by 1 week every 3 months based on clinical course	Clinically and photographically using validated scoring systems
Atopic dermatitis	Second-line and if >12 months' duration; SCORAD >45; refractory in the last year to all the three-first-line therapies (topical steroids, calcineurin inhibitors and phototherapy) or to one-second-line therapy (systemic steroids, cyclosporine)	One cycle every 2 weeks for 12 weeks	Intervals depending on the individual response of a patient, that is, every 4 weeks for another 3 months; at maximal response treatment should be tapered to one treatment cycle every 6–12 weeks	SCORAD assessment every 2 weeks for the first 12 weeks, and thereafter every 4 weeks or at longer intervals
Crohn's disease	Moderate to severe steroid-dependent disease, refractory or intolerant to immunosuppressive and anti-TNF agents	One cycle every 2 weeks for 12–24 weeks	No data available	Crohn's Disease Activity Index Score
Miscellaneous dermatological diseases(pemphigus, epidermolysis bullosa acquisita, erosive oral lichen planus)	Recalcitrant to conventional systemic therapies	One cycle every 2–4 weeks for 12 weeks then one cycle every 4 weeks	Treatment tapering by increasing intervals by 1 week every 3 months	Clinically and photographically using validated scoring systems and autoantibody titre, at least in the case of pemphigus vulgaris.

CR, complete response; ECP, extracorporeal photopheresis; FEV1, forced expiratory volume in 1 s; NIH, National Institutes of Health; SCORAD, SCORing Atopic Dermatitis; TNF, tumour necrosis factor.

1.3.6 Technical aspects

This section will enter in detail about the sterile cassette in which the photoactivation of 8 – MOP takes place.

First, it is essential to distinguish between two main ECP methods already mentioned before: off – line or open technique, in which collection and irradiation are carried out in two different devices, and in – line or closed method, where all stages are integrated and automated in the same device (Schooneman, 2003). The second method overcomes the potential risks of infections, contaminations and re-infusion errors (Knobler R. B.-P., 2014), and it is the most interesting regarding the blood irradiation in a dynamic fashion. The best example of this method is represented by the Therakos® Cellex® Photopheresis System, whose irradiation chamber is shown schematically in Figure 1.8.

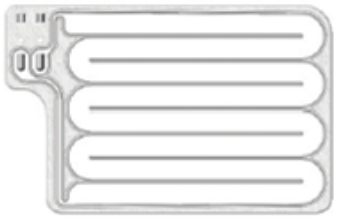

Figure 1.8: Photoactivation Module from Cellex Operators Manual.

In order to better understand how the irradiation takes place during the continuous flow of the WBCs concentrate, a study on patents related to the irradiation chamber was conducted and the information gained are exposed below.

The first patent was dated back to 1988 and exposed the irradiation chamber for a photoactivation patient treatment system (Washington, DC: U.S. Patent No. 4,737,140, 1988). Figure 1.9 shows an overall view of the system containing chamber, recirculation pump and photoactivating light source array.

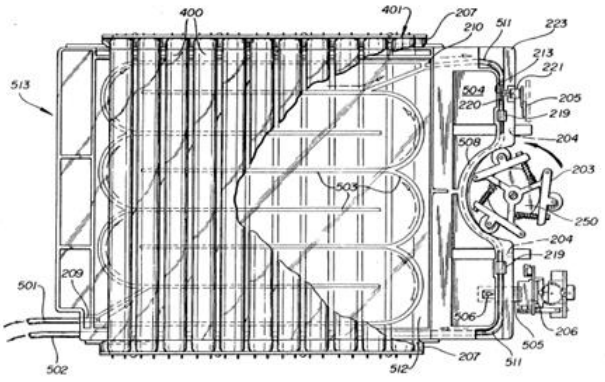

Figure 1.9: Front view of irradiation chamber mating with pump and light source (Washington, DC: U.S. Patent No. 4,737,140, 1988).

Comparing Figure 1.8 and Figure 1.9, it is clear that nowadays chamber maintains the same shape proposed at the beginning.

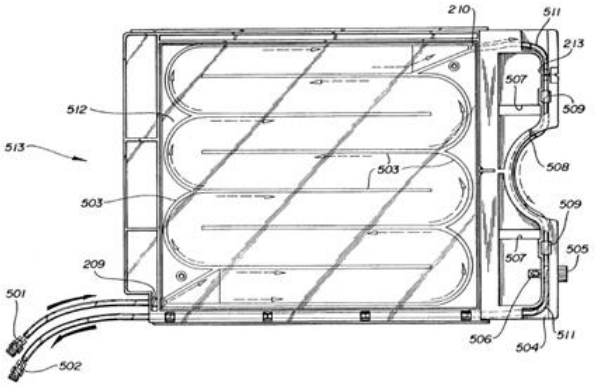

Figure 1.10: Side view of the irradiation chamber (Washington, DC: U.S. Patent No. 4,737,140, 1988).

Figure 1.10 shows the chamber, whose main characteristics are the following:

- It is composed by a flat plate irradiator in which leukocytes-enriched blood flows.
- The plate contains a thin cavity (thickness: 0.04 inches = 1.02 mm) which offers a large surface area and reduce self-shielding effect.
- The cavity has a serpentine pathway that avoid or minimize stagnant areas of flow.
- The outlet tubing passes through a recirculation pump, which permits recirculation of fluids creating peristaltic flow, and incorporates a thermocouple for monitoring of fluid temperature.
- Materials used must be transparent to the wavelength of radiation (e.g. polycarbonate).

Some additional information can be obtained from another patent published in 2004 regarding an irradiation chamber for treatment of blood cells by exposure to electromagnetic radiation, such as UV light (U. S. Patent No. 10/742,343, 2004). The chamber is composed by two plates,

one with partitions extending from its surface and the other with recesses that joined together form a serpentine pathway (Figure 1.11). The so-formed channel has a rectangular cross-section with long side the distance between partition and short side the distance between the plates. The optimized number of channels range is 6 – 8 and favourable materials for the realization of the invention are polycarbonate or acrylic.

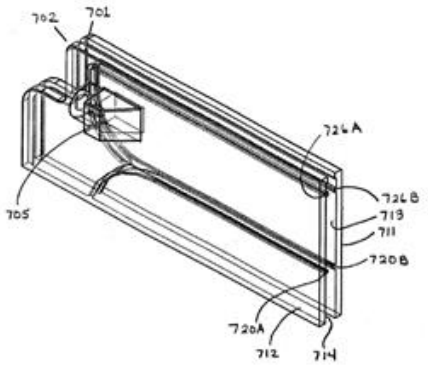

Figure 1.11: Cut-away of a section of the two plates before being joined together (U. S. Patent No. 10/742,343, 2004).

The UV light array assembly for the irradiation of the chamber has the following features:

- One, or preferably two lines of radiation sources;
- The chamber is positioned between the rows of sources so that the irradiation comes from both sides of the cavity;
- The sources should be chosen in order to offer a constant illumination over the entire radiation cavity and examples are phosphorus bulbs or fluorescent tubes.

An illustration of this system is reported in Figure 1.12 (Washington, DC: U.S. Patent No. 4,737,140, 1988).

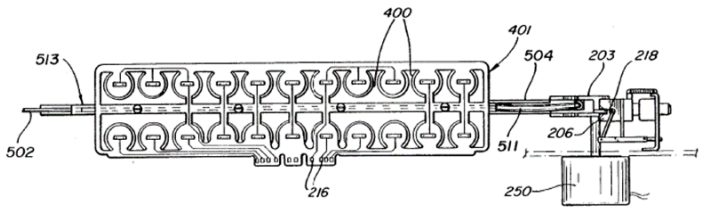

Figure 1.12: Light array assembly with the chamber that slides in the middle of the two light rows (Washington, DC: U.S. Patent No. 4,737,140, 1988).

Finally, from Cellex Operator's Manual some relevant information about the photoactivation module (Figure 1.8) can be gathered: it is a disposable, thin, sterile fluid pathway made by acrylic material that is inserted between the two rows of UV-A lamps in a vertical orientation.

Regarding flow rates used, for collection and reinfusion the range is 30 – 40 mL/min, while the irradiation module achieves 100 mL/min.

In conclusion, nowadays the chamber in which irradiation and 8 – MOP activation take place remain similar to the first system arrangement engaged for this purpose. For this reason, a collaboration with Therakos, nowadays acquired by Mallinckrodt Pharmaceuticals, was started in order to obtain the cartridge to be tested in our laboratory and understand if it can be suitable for our goals or used as starting point for future modifications.

1.4 Extracorporeal photopheresis validation

The aim of this section is to understand how ECP has been validated through in vitro, in vivo and clinical studies, in order to plan possible preparatory tests for a future validation of the novel technique proposed by the project.

1.4.1 In vitro studies

In vitro studies are based on cell lines that represent in vitro models of diseases, and ECP technique is applied on these cells in a plastic container and not through a dynamic closed circuit.

In order to overcome some of the mentioned problems of 8 – MOP, namely the potential risks of carcinogenesis and the lack of specificity, some researchers tried to modify the ECP technique with porphyrin precursors, that form an intermediate product in the heme biosynthetic pathway, resulting to be a photosensitizer. In 2007, Akita et al. used HUT – 78 cell line, derived from human Sézary Syndrome (SS), to investigate combination of porphyrin precursor (ALA, 5-aminolevulinic acid) and PUVA for antitumor effect (Akita, 2007). In the same direction, in 2014, Čunderlíková and co-workers tested two porphyrin precursors (ALA and HAL, his exylester) on two human T – cell lymphoma cell lines: Jurkat and Karpas 299. In both studies, the cell suspension was irradiated with UV-A and a non – irradiated solution was used as control. Therapy effect was studied evaluating in-vitro proliferation by MTT assay, and apoptosis was assessed by fluorescence microscopy, studying nuclear morphology after staining with Hoechst and Propidium Iodide (PI). Karpas cells resulted to be more resistant to treatment (Čunderlíková, 2014) and the main differences between standard ECP and porphyrin-mediated one are visible in cell death mechanism: 8 – MOP induces mainly apoptosis, while HAL – mediated cell death resulted to be a combination of apoptosis and necrosis, moreover it depends on parameters such as HAL concentration and UVA irradiation time.

Finally, a recent work published in 2019 proposed to study and quantify the influence of different components of WBCs concentrate on treatment efficacy (Laulhé, 2019). They used an immortalized Jurkat cell line because it offers many advantages, namely cell homogeneity, pathological composition from human T-cell lymphoma, spontaneous proliferation, and similar apoptosis kinetics with respect to peripheral blood mononuclear cells (PBMCs). The components of the irradiated solution are very close to the real procedure: Jurkat cells, ACD-A as anticoagulant, RBC to obtain the right haematocrit and a solution composed by plasma and NaCl. The apoptosis assessment is done by double staining with Annexin-V conjugated with fluorescein isothiocyanate (FITC) and PI to distinguish necrotic from apoptotic cells, while proliferation assay is based on automated cell counting at day 0 and 3 after the treatment.

In conclusion, the use of cell lines instead of human cells from patients' blood avoids the variability in treatment response and the need of mitogen – induced proliferation, leading to a standardized treatment and precise analysis. On the other hand, cell lines are only a representation of diseased cells and they lack the possibility to study consequences of the treatment at immune system level, which is necessary for understanding ECP mechanisms of action. A brief summary of the most important aspects emerging from in vitro studies is reported in Table 1.9.

Table 1.9: Summary of cell lines, types of treatment and condition, controls and analysis for in vitro studies.

Bibliographic reference	Cell line	Sensitizer	Treatments	Controls	Irradiation regime	Treatment condition	Analysis
(Akita, 2007)	HUT –78	8-MOP, ALA	8-MOP+UVA, ALA+UVA, ALA+8-MOP+UVA	Non irradiated cells	Intensity:1 J/cm^2	Static	MTT assay
(Čunderlíková, 2014)	JURKAT, KARPAS 299	8-MOP, HAL	HAL+8-MOP, UVA alone, HAL+UVA, 8-MOP+UVA, HAL+8-MOP+UVA	Non irradiated cells and irradiated without sensitizer	Time: 5 and 10 min	Static (well plates)	MTT assay , Nuclear morphology
(Laulhé, 2019)	JURKAT	8-MOP	8-MOP only, 8-MOP+UVA	Non irradiated cells	Intensity: 2, 3, 4 J/cm^2	Static (plastic bag)	Cell counting, Annexin V-FITC and PI

1.4.2 In vivo studies

In vivo studies are based on animal models of T-cell mediated diseases and their main objective is to clarify ECP mechanisms of action. In literature, no examples of animals treated directly through an ECP machine have been founded, but only extracorporeal circulation (ECC) applied on animal models are reported, such as the study proposed by Luo et al., that try to overcome the systemic inflammatory response of the treated body caused by ECC (Luo, 2015).

On the other hand, the basic principle of animal models for ECP is a bit different and it is well described in Figure 1.13. The starting point for building such a model is the production of a strong immune response in the animal, in this case obtained by the inoculation of sheep RBCs in syngeneic mice. The activated lymphocytes, responsible for the immune response and concentrated in the spleen, are then extracted, treated with ECP (8 – MOP and UV – A radiation in a Petri dish), and finally re-injected into syngeneic recipient mice. As a result, when these mice are again exposed to RBCs of the sheep, they do not show any immune response, confirming the inactivation of T-cells due to the ECP treatment (Edelson R. L., 1988).

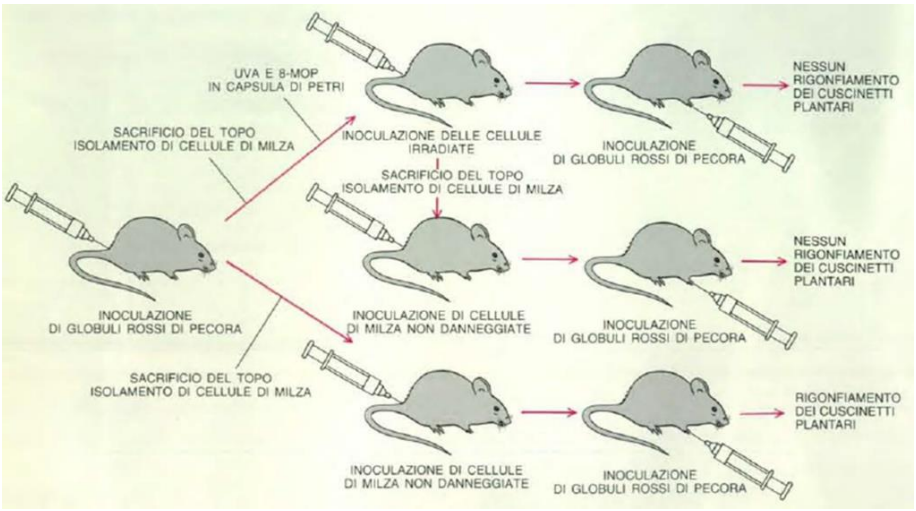

Figure 1.13: Animal models for ECP in vivo studies.

Following the same principle, in 1993 Iperen et al. developed a model of contact hypersensitivity (CHS), a T-cell mediated immune response, in Wistar-derived rats, using dinitrofluorobenzene (DNFB) applied in ventral skin. Half of the animals were sacrificed and cells from their lymph nodes extracted, let to form culture suspension that were then incubated with 8 – MOP and irradiated with UV-A for 1 hour. After the treatment, cells were re-injected intravenously into remaining rats and the final challenge with DNFB was done in the left ear, leaving the right as a control. The analysis of treatment effects were based on the measurement of both ear thickness 24 hours after the treatment, evaluating the swelling percent between them.

They observed the immune suppressive effect of the ECP treatment due to production of regulatory T – cells (Iperen, 1993).

Another important model for ECP is represented by allografts, as reported by George and co-workers in 2008, who used a CBA/CaJ mice as recipient of abdominal cardiac allograft from C57BL/6J donors. In this study, splenocytes of receivers' mice were treated by ECP before the allograft, using as control treatment the same procedure without the UV-A irradiation (only 8-MOP). Treatment analysis was performed by palpation through abdominal wall to assess the correct transplanted heart function up to death. The prolonged survival over time in ECP-treated recipient mice was due to immunosuppressive activity by $CD4^+$ and $CD25^+$ cells towards alloreactive T cells (George, 2008).

More recently, many GVHD animal models were developed, such as murine BALB/c that was used by Budde et al. for bone marrow transplantation (BMT). They treated GVHD affected mice splenocytes by ECP and subsequently transplanted them into a second cohort of GVHD affected mice. The control animals received only PBS without treated cells. Treatment analysis were performed through flow cytometry of splenocytes, extracted from sacrificed treated mice, and animals' survival rate. The two indexes showed a higher survival of ECP treated mice with respect to the control (Budde, 2014).

Many others similar ECP animal models can be found in the literature and a final summary table is reported below (Table 1.10). It shows the studies previously described and some others examples, in order to gain information about ECP treatment and its analysis. Unfortunately, animal studies showed non-uniform conditions in cell treatment, UV irradiation, solution and container used.

Table 1.10: Summary on ECP animal models, types of treatment and analysis.

Bibliographic reference	Animal model	Disease	First treatment	Second treatment	Analysis
(Iperen, 1993)	Albino Wistar rats	Elicited CHS	Sensitization and challenge with DNFB	Challenge in ECP treated rats with DNFB	Ear swelling
(Maeda, 2005)	C3H/He, BALB/c mice	Elicited CHS	Sensitization with DNFB	Sensitization and challenge in ECP syngeneic treated mice	Ear swelling and distribution of ECP treated cells in recipient organs

(George, 2008)	CBA/CaJ, C57BL/6J mice	Cardiac allograft rejection	Cardiac allograft on ECP-treated mice	Adoptive transfer of ECP produced cells and cardiac allograft	Palpation, measure of T-reg cells by flow cytometry and survival rate
(Gatza, 2008)	C3H.SW, B6 mice	GvHD	Bone marrow allogenic and syngeneic graft	BM allograft and ECP from 2^{nd} to 1^{st} cohort	Histopathologic analysis and survival time after BMT
(Budde, 2014)	BALB/c, C57BL/6J mice	GvHD	Bone marrow allograft	ECP from 1^{st} to 2^{nd} cohort	Measure of T-reg cells by flow cytometry and survival rate

1.4.3 Clinical studies

Clinical studies on ECP comprise all studies on human patients from the first published in 1987 by Edelson et al. onwards. The first clinical study involved 41 patients with CTCL that underwent ECP with oral 8-MOP administration and UVA exposure in a 1-mm thick sterile cassette, using as a control the same blood cells not exposed to light. The analysis performed by the group were the determination of lymphocyte viability (trypan blue exclusion), proliferative capacity of T cells (triated thymidine incorporation after stimulation with mitogens) and evaluation of T-cell subsets (indirect immunofluorescence) (Edelson R. B., 1987).

During the last decades, many protocols were proposed for ECP validation, which is required for clinical application of this technique, even if the best validation protocol has not yet been established. Few studies addressed this problem, as it is described in the following.

In 2003, Jacob et al. proposed to use as parameter the antiproliferative effect of ECP measured by the quantification of ^{3}H incorporated-thymidine into newly synthetized DNA. They applied an off-line ECP technique on 16 patients with CTCL and GVHD using mononuclear cells collected before and after UVA irradiation. Furthermore, they defined a threshold of 70% of proliferative inhibition 3 days after the process to consider it normal (Jacob, 2003). The same parameter was used some years later from Evrad and co-workers on 34 patients with CTCL and GVHD, even though they proposed a flow cytometric method with CFSE (5,6-carboxyfluorescein diacetate succinimidyl ester) labelling for obtaining information about the

degree of proliferative inhibition. The results of these two techniques are similar, but the CFSE method represents a good alternative because it overcomes the problems of cost and safety related to triated thymidine (Evrard, 2010).

At this time point, animal studies had elucidated apoptosis to be the main ECP mechanism of action and the need for a test evaluating the lymphocytic apoptosis emerged in clinical studies. Following this requirement, Taverna et al. in 2015 suggested to measure mononuclear cells apoptosis generated by ECP as additional validation parameter. They obtained mononuclear cells from 13 patients with GVHD and tested them with Annexin V-FITC in association with PI staining, getting percentage of apoptosis between 70 % and 85 % at 48 hours after the treatment. Additionally, they set a threshold to define suitable ECP procedure at 15% of apoptosis at day 1 after culture. It should be noted that evaluating apoptosis is less time consuming and easier, in fact Annexin labelling requires only 15 minutes with respect to the days required for mitogens proliferation induction (Taverna, 2015). Moreover, CFSE and Annexin-V both require flow cytometer analysis, but proliferative cells can also be evaluated by tetrazolium salt (WST-1) method that does not require it, as reported by Chieregato et al. They applied the ECP procedure on 6 patients with GVHD and compared results from different assays. Quantification of CFSE and Annexin-V by flow cytometer permits to measure more parameters simultaneously (proliferation, apoptosis, viability, morphology) even if they both require the flow cytometer apparatus. On the other hand, WST-1 assay does not require it and it is an easy and rapid method, even if there is still a need to define a minimum threshold for apoptosis evaluation based on this technique (Chieregato, 2015).

Table 1.11 summarizes the characteristics of these studies regarding samples, control, disease treated and types of tests applied on the sample.

Table 1.11: Summary of samples, disease, applied ECP, controls and analysis for in vivo studies.

Bibliographic reference	Sample	Disease	ECP technique	Irradiation regime	Controls	Analysis
(Edelson R. B., 1987)	Leukocyte-enriched blood	CTCL	In-line (closed)	Time: 270 min Intensity: 2 J/cm^2	Non irradiated solution	Trypan blue exclusion, ^{3}H-thymidine incorporation, indirect immunofluorescence
(Jacob, 2003)	PBMCs	CTCL, GVHD	Off-line (open)	Intensity: 2 J/cm^2	Non irradiated solution, cells cultured without mitogen	^{3}H-thymidine incorporation
(Evrard, 2010)	PBMCs	CTCL, GVHD	Off-line (open)	Intensity: 2 J/cm^2	Non irradiated solution, cells cultured without mitogen	^{3}H-thymidine incorporation, CFSE labelling
(Taverna, 2015)	PBMCs	GVHD	Off-line (open)	Intensity: 2 J/cm^2	Non irradiated solution, cells cultured without mitogen, cells from healthy donors	Annexin V-FITC with PI staining, CFSE labelling
(Chieregato, 2015)	PBMCs	GVHD	Off-line (open)	Time: 10 min Intensity: 2 J/cm^2	Non irradiated solution	Annexin V/7-AAD staining, CFSE labelling, WST-1 assay

2 Ultrasounds application and methods of study

After the review on different aspects of ECP, which is based on the photodynamic therapy (PDT) approach, the novel proposal of XtraUS project is based on the most recently developed sonodynamic therapy (SDT). This method, originated form PDT, combines ultrasounds and a molecule activated by them called sonosensitizer (Canavese, 2018). In this section, the basic physics of ultrasounds and their interaction with fluids and nanoparticles will be discussed, including methods for the study of these interaction effects.

2.1 Basics of ultrasound

Ultrasound is a mechanical pressure wave propagating longitudinally in a continuous medium and characterized by frequencies higher than the upper audible limit (approximately 20 KHz) (Shibaguchi, 2011).

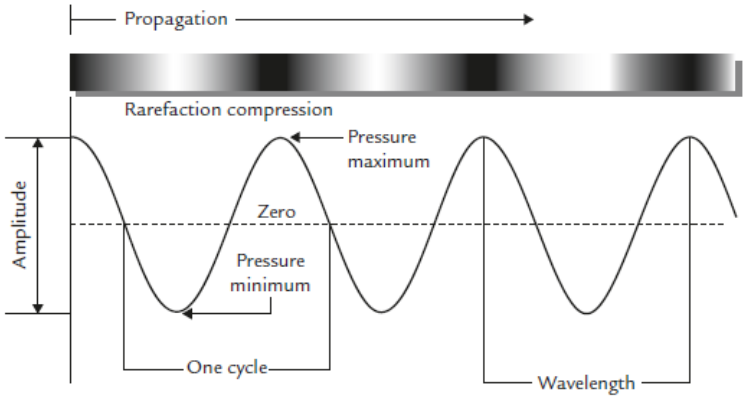

Figure 2.1: Schematic representation of the US wave propagating in a continuous way (Cheng-Huang Su, 2008).

It is usually generated by an ultrasonic transducer, made of piezoelectric material, which is excited at the proper frequency by a generator and it is able to transform electric signal into mechanical displacement (Canavese, 2018). The relationship between frequency (f) expressed in Hz, wavelength (λ) expressed in meters and sound velocity (c) in m/s is the following:

$$\lambda = \frac{c}{f} \tag{2.1}$$

Sound velocity depends on the physical properties of the material where the sound propagates:

$$c = \sqrt{\frac{E}{\rho}} \tag{2.2}$$

Where E (N/m^2) is the young modulus of the material and ρ (kg/m^3) is the mass density. A reference point is the sound speed in air at 20°C and pressure of 1 atmosphere, which is 344 m/s.

The parameter that describes the propagation of ultrasounds in different materials is the acoustic impedance (Z). It represents the resistance of the material to the passage of sound wave and its valued depends on material c and ρ. It is described by the following equation:

$$Z = \rho c \tag{2.3}$$

When US encounter an interface between two different materials characterized by Z_1 (the first material) and Z_2 (the second material), the wave can be reflected or transmitted, following the Transmission (T) and Reflection (R) coefficients:

$$R = \frac{Z_2 - Z_1}{Z_2 + Z_1} \tag{2.4}$$

$$T = \frac{2Z_2}{Z_2 + Z_1} \tag{2.5}$$

The higher the difference in acoustic impedance between two materials, the higher the reflection. For instance, water is characterized by high acoustic impedance with respect to a gas, which show very low acoustic impedance. Thus, a coupling gel is necessary between the ultrasound transducer and the aqueous medium in order to minimize the air present and the related reflection.

Finally, ultrasounds can be applied either in a continuous or in a pulsed waveform. In the latter application, the wave is identified by the Duty Cycle (DC), described as follow:

$$DC = \frac{\tau_p}{\tau_s} \tag{2.6}$$

Where τ_p is the pulse length, namely the duration of the pulse, and τ_s is the time between two consecutive pulses.

2.2 Acoustic cavitation

Transmission of ultrasound wave in liquids can lead to thermal effects, mainly an increase in temperature, but also non-thermal effects, which can be considered a complex set of processes, including microstreaming, radiation forces and acoustic cavitation (Canavese, 2018), the most important for the purpose of this project. Acoustic cavitation is a phenomenon that involves formation, growth and subsequent collapse of gas bubbles (Shibaguchi, 2011), due to a time-

varying, usually sinusoidal, pressure applied to the liquid, corresponding to expansion and contraction phases.

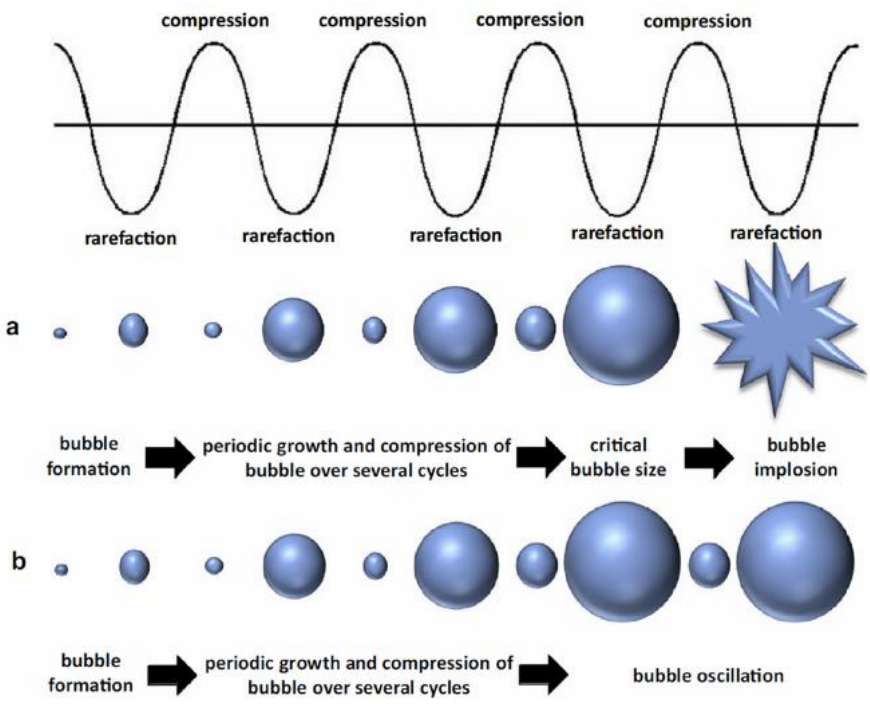

Figure 2.2: Schematic representation of transient (a) and stable (b) cavitation resulting from the application of US (Vyas, 2019).

A first distinction can be made between transient (Figure 2.2a) and stable (Figure 2.2b) cavitation: the stable one is characterized by permanent bubbles that oscillate for many cycles of pressure variation. On the other hand, transient bubbles generally disappear after few cycles because they expand to many times their original size and finally collapse violently (Neppiras, 1980). During such collapse, it is observed the generation of very high temperatures (above 5000 K) and pressures (above 800 atm), corresponding to the release of high energy. Thus, they behave as particular micro reactors, and if the liquid in which the bubbles collapse occurs is water, they are capable to induce water thermal dissociation into hydroxyl radicals (HO·) and hydrogen atoms (H·), as described by the following reaction:

$$H_2O \rightarrow H\cdot + HO\cdot \qquad (2.7)$$

Moreover, considering that usually water is air-saturated, the reaction (2.7) is usually accompanied by the cleavage of dissolved oxygen, O_2.

$$O_2 \rightarrow O\cdot + O\cdot \qquad (2.8)$$

The cleavage product and radicals can recombine and generate other types of radicals, leading to the formation of several reactive oxygen species (ROS), within which some examples are

explained in Eq. (2.9) - (2.12) below (McMurray, 1999). The result is a final oxidative stress environment, that is fatal for cells, including cancer cells (Canavese, 2018).

$$HO\cdot + HO\cdot \rightarrow H_2O_2 \quad (2.9)$$

$$H\cdot + O_2 \rightarrow HOO\cdot \quad (2.10)$$

$$H\cdot + H\cdot \rightarrow H_2 \quad (2.11)$$

$$H\cdot + HOO\cdot \rightarrow H_2O_2 \quad (2.12)$$

Within different radicals, the hydroxyl one is considered one of the strongest, due to its highest reduction potential and its capability to react with several biological molecules (Vighetto, 2019), thus its presence in sonicated medium has been deeply studied in this Master Thesis.

The presence of nanoparticles (NPs) in the sonicated solution can help the above process because of their surface roughness and porosity, which provide nucleation sites for cavitation bubbles. As a result, the cavitation threshold is lowered and NPs can be applied as sonosensitizer in the SDT approach. Figure 2.3 summarizes the role of NPs in the SDT, underlying the cytotoxic effects of acoustic cavitation.

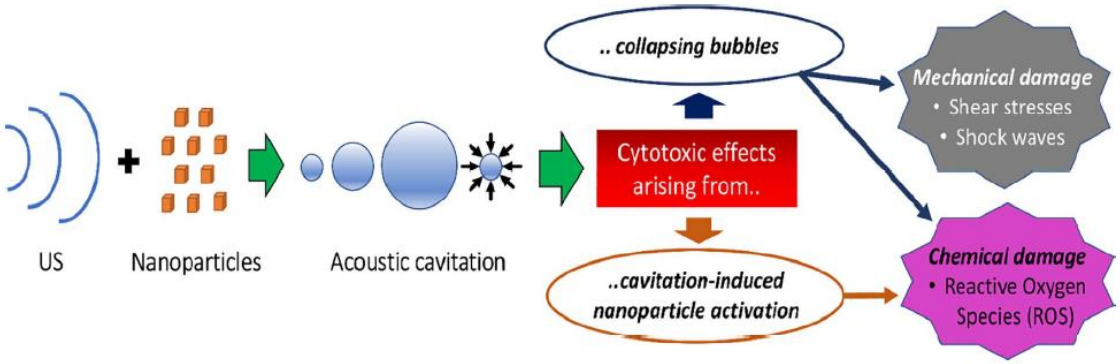

Figure 2.3: Mechanisms of action for SDT: combination of US and NPs leads to acoustic cavitation. The result is a combination of several cytotoxic effects including mechanical and chemical damages (Canavese, 2018).

Different types of NPs are applied nowadays in nanomedicine, including Zinc Oxide (ZnO), which has become particularly interesting thanks to its biocompatibility, multifunctional properties (from optical to piezoelectric ones) and some intrinsic anticancer characteristics. In particular, ZnO is widely used for its cytotoxicity related to production of ROS and Zn^{2+} ions release both in anticancer treatments and antimicrobial applications (Racca, 2020).

In conclusion, ultrasound cavitation and consequent ROS production has emerged as a tool for cancer therapeutic applications: the evaluation of ROS presence in sonicated solutions has been provided in this Master Thesis by two different methods: Sonochemiluminescence (SCL) of

Luminol solution and Electron Paramagnetic Resonance (EPR) Spectroscopy, followed by a final comparison between them.

2.3 Sonochemiluminescence of Luminol

Luminol alkaline solutions represent a qualitative and fast method for studying cavitation and subsequent ROS formation. These solutions are capable of emitting visible light when ultrasounds are applied and cavitation occurs, through a process known as sonochemiluminescence (SCL), in which the sono-generated HO· radicals chemically react with Luminol.

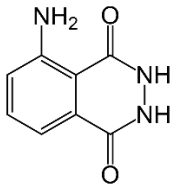

Figure 2.4: Luminol chemical structure.

The Luminol molecule, to show luminescence, must be previously activated with an oxidant, such as hydrogen peroxide (H_2O_2) and hydroxide ions (OH^-) in a water-based solution. The mechanism of SCL is shown in Figure 2.5 and briefly explained in the following.

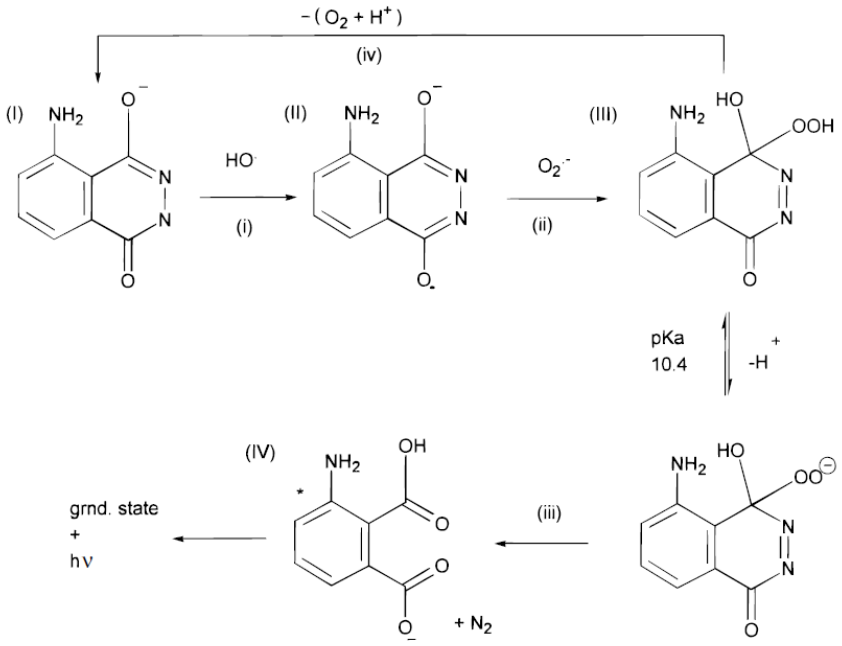

Figure 2.5: Reaction pathways of Luminol Sonogenerated Chemiluminescence (McMurray, 1999).

The step (i) of the pathway is Luminol oxidation by the hydroxide ion (OH·) coming from the cleavage of water (Eq. (2.7)), to form the diazaquinone radical anion (II). This anion subsequently reacts in step (ii) with the oxygen (O_2^-) coming from the dissociation of the

hydrogen peroxide. The organic peroxide which is formed is a weak and very unstable acid, characterized by two forms: the neutral form and the monoanion form. The first one decomposes via reaction (iv) and give rise to the starting material (I), while the monoanion form tends to lose the nitrogen (N_2) via step (iii). The product of this process is the aminophthalate monoanion acid (IV), a light-emitting species with electrons in an excited state. It is the final relaxation of this acid from the excited state to the ground state which is accompanied by the emission of a photon visible in the blue light (ν = 430 nm) (McMurray, 1999). Unfortunately, the effect of chemiluminescence is weak and hardly to be seen with the naked eye, therefore digital camera with long exposure times are essential for SCL detection (Corzo, 2018). Furthermore, as reported by McMurray et al., the light emission is highly influenced by concentration of H_2O_2 and solution pH (McMurray, 1999), for this reason, a starting literature research was conducted for obtaining information regarding volumes and concentrations of Luminol solutions components and video camera acquisition set-up.

Table 2.1: List of information from experimental studies on SCL of Luminol.

Bibliographic reference	**US transducer position**	**Luminol solution**			**Video camera**	
		Volume	**[Luminol]**	**Other species**	**Setting**	**Position**
(McMurray, 1999)	Inside the solution	100 mL	1 mM	H_3PO_4: 0.1 M, H_2O_2: 0.1 mM, EDTA: 0.1 mM	/	/
(Rooze, 2011)	Inside the solution	250 mL	50 mM	Na_2CO_3: 0.1 M	ISO 3200, f 5.0, T_{exp} = 3 min	In front of the container
(Rivas, 2012)	Bottom of the chamber	250 µL	0.1 mM	NaOH: 0.1 M	ISO 1250, f 5.0, T_{exp} = 1 min	Above the container
(Corzo, 2018)	Inside the solution	15 mL	1 mM	Na_2CO_3 0.01 M H_2O_2: 0.2 mM CCl_4: 20 µL	/	Bottom and side of the vessel

Table 2.1 above shows that Sodium hydroxide (NaOH), Sodium carbonate (Na_2CO_3) or Phosphoric acid (H_3PO_4) can be used for the formulation of alkaline solution, while for Luminol activation the choice is H_2O_2, even if not reported from all the papers. In fact, it has been studied that SCL can also occur in the absence of H_2O_2 because the oxygen necessary for the progression of the reaction pathway can be produced directly from dissociation of HOO·,

coming from reaction (2.10), and some H_2O_2 is generated internally from reaction (2.12). Thus, a sufficient quantity of O_2 could be present for emission of light through SCL, even if at lower intensities with respect to the case in which H_2O_2 is added to the solution (McMurray, 1999).

Other species present in the solutions, namely Ethylenediaminetetraacetic acid (EDTA) and Carbon tetrachloride (CCl_4), are used for specific study purposes: EDTA as a chelating agent for the suppression of background luminescence due to presence of transition metal cations, and CCl_4 for the enhancement of light emission. Furthermore, Luminol concentration has a range between 0.1 mM and 50 mM and solution volumes show differences related to the different size of the containers. Regarding the digital cameras applied in image acquisition, they can be placed in front of the container or above it, using exposure times in the order of 1-3 minutes and different ISO and f-number.

It is clear that several experimental set-ups are used in literature for SCL experiments, hence different starting tests were conducted in this Thesis in order to obtain the better one for the purpose of this project. After that, Luminol solution characteristics have been kept unchanged for all the experiments, while some changes have been made regarding the acquisition.

2.4 Electron Paramagnetic Resonance Spectroscopy

Electron Paramagnetic Resonance (EPR) is a spectroscopy technique that measures energy differences between states of a particular species due to the absorption of energy from an electromagnetic radiation. The differences measured by EPR spectroscopy are due to the interaction between unpaired electrons in the species under study, such as the hydroxyl radical, and a magnetic field produced by a magnet in the EPR instrument. Unpaired electrons can be oriented by the magnetic field following the so-called Zeeman Effect. Every electron is characterized by a magnetic moment that can be aligned with or against the magnetic field, generating two different energy levels. Then, the combination of the applied magnetic field and an electromagnetic radiation (in the microwave range) leads to the absorption of energy by unpaired electrons (Hawkins, 2014).

$$\Delta E = h\nu = g\mu_B B_0 \qquad (2.13)$$

Eq. (2.13) above describes the absorption of energy (ΔE) at the base of EPR, which is proportional to the product of Planck's constant (h) and the radiation frequency (ν). From quantum mechanics, this product is also equal to the product of three elements: the g-factor,

which depends on the radical nature (g = 2.0023 for a free electron), the Bohr magneton, which is the natural unit of electronic magnetic moment, and the applied magnetic field B_0.

In order to obtain the absorption spectra, the microwave field is applied with constant frequency, due to technical and construction reasons, while the magnetic field is scanned over a range of intensity values. When the electrons energy difference (created by the scanned magnetic field) matches the energy of the microwave, the unpaired electrons can move between the two states and the absorption peak is measured.

The problem of many ROS, including the already mentioned hydroxyl radical, is the very short half-life, limited to few nanoseconds, which makes them unsuitable for EPR analytical measurements. Thus, this technique is usually coupled with spin traps that are chemicals that bind covalently with free radicals and stabilize them for a longer time period (around 2-3 hours) so that they can be detected by EPR. In the case of OH·, OOH· (Hydroperoxyl) and CH_3· (Methyl) radicals detection, the spin trap molecule used is 5,5-Dimethyl-1-Pyrroline-N-oxide (DMPO). It is dispersed in the sample before the application of US and it is capable to bind to the short-lived radicals produced during cavitation, leading to a spin adduct stable for many minutes, as it is shown in Figure 2.6.

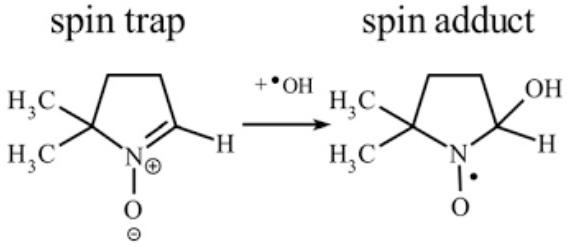

Figure 2.6: Chemical structure of the spin trap molecule (DMPO) before (left) and after the OH· radical encounter (right).

The instrument permits to study the presence of this novel molecule (DMPO-OH) in the sample, through the spectrum acquired. As reported by Hawkins et al., depending on the nature of the radical under study, the spectrum can contain different number of peaks (Hawkins, 2014). Regarding the DMPO-OH spectrum, it is composed by four peaks, related to the hyperfine coupling, which is the interaction between the free electron and the surrounding nuclei. In this case, only the Nitrogen and the Hydrogen are close enough to produce this phenomenon, while all the other nuclei are too distant. This interaction leads to a splitting of the spectrum in N components or peaks, following the Eq. (2.14):

$$N = 2nl + 1 \qquad (2.14)$$

Where l is the nuclear spin of the nucleus in question (1/2 for H and 1 for N) and n is the number of such nuclei (Hawkins, 2014) (Davies, 2016). Thus, the Hydrogen nucleus produces a splitting into two components and the Nitrogen nucleus in the DMPO molecule causes a successive split of those two components into 3 elements. Moreover, two lines occur at the same frequency and field values so that their superposition gives the final spectrum of 4 peaks with an intensity distribution of 1 : 2 : 2 : 1, as it is depicted in Figure 2.7.

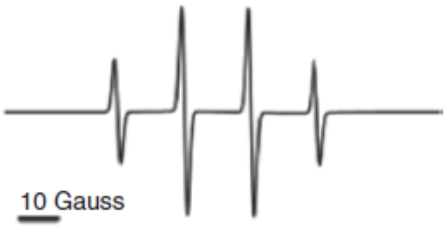

Figure 2.7: Shape of the EPR spectrum for the DMPO-OH construct.

Finally, the integrated intensity, i.e. the area beneath the absorption curve, is proportional to the concentration of the spin adduct, and thus to the concentration of the radical that has been evaluated.

In conclusion, the EPR technique permits to obtain absorption spectra for a specific ROS, but also quantitative information resulting from it, namely the number of radicals present in the sample and their concentration.

2.5 Numerical simulations

The numerical simulations represent a powerful tool for the study of the interaction between different physical parameters, for this reason they are very interesting for the purpose of the project and the present Master Thesis, because they can help to investigate the interaction between US, fluid flows and NPs.

The simulations of the distribution of the acoustic pressure field has emerged in the last two decades for studying sonochemical reactors and predicting cavitation events inside them (Tudela, 2014). The majority of the works rely on linear-based models for the simplicity in the equations and boundary conditions: some examples are represented by the following works, where the authors characterized sonochemical reactors by comparing numerical simulations and experimental results coming from classical physical methods, such as calorimetry and thermal probes. Saez et al. characterized the sonoreactor by 2D simulations of the pressure field propagation at different US intensities (Saez, 2005), while Klima et al. implemented a 3D

simulation to obtain the intensity distribution within the reactor and showed that the energy distribution strongly depends on the reactor shape (Klima, 2007). Following the previous studies, Kim and co-workers simulated pressure and temperature profiles of four solvents using different US powers and irradiation times: they observed the increase in the gap between minimum and maximum pressure by increasing the US intensity (Kim, 2009). All the previously mentioned works treated the solid boundaries of the reactor as infinite rigid or soft walls, but when the solution is not directly sonicated by the US source, it is important to take into account the sonoreactor walls deformation (Tudela, 2014). This was done by Yasui et al., who numerically calculated the spatial distribution of acoustic amplitude in a reactor taking into account the acoustic emission from the walls and they demonstrated that thin glass walls acted as soft boundaries, while thick glass walls acted as solid boundaries. Moreover, they also investigated the effect of the liquid height on the acoustic field, showing differences in the presence of pressure nodes or antinodes at the vibrating plate (Yasui, 2007). As mentioned before, all the above-mentioned works followed linear approaches to solve an actually non-linear acoustic field, due to the formation, growth and collapse of cavitating bubbles. Despite the complexity of this phenomenon, a few research groups also tried to simulate non-linearity in sonoreactors, such as Louisnard and co-workers (Louisnard, 2012) that coupled bubble dynamics, energy dissipation and non-linear attenuation of the acoustic waves. In more recent works, acoustic cavitation is investigated by the parallelism between sonochemical activity, studied by the SCL of Luminol, and the validation of the acoustic pressure field using numerical simulations. Kauer et al. investigated the influence of the presence of a solid material in the sonoreactor on cavitation activity by using 2D simulations. The latter were important to observe a modification of the acoustic pressure amplitude distribution at the sample surface, due to reflections and absorptions of the wave energy (Kauer, 2017). Similarly, Tiong and co-workers showed good correlations between the SCL patterns and the acoustic pressure field at different US frequencies and they observed an increase in the maximum acoustic pressure by increasing the irradiation intensity (Tiong, 2017).

The works presented until this point only analysed static conditions, however moving to the dynamic ones with the coupling of the acoustic field and the fluid flows, such as in microfluidics, the acoustofluidics approach must be considered. It offers several possibilities, among which the manipulation of both fluids and particles, in particular, the acoustophoretic approach permits to focus particles by forming a standing wave inside a medium with the particles suspended. Many works in this field apply numerical simulations for studying the

pressure field and the particle motion under a fluid flow: Muller et al. performed a numerical analysis on a 2D rectangular channel cross section subjected to US resonance and they obtained particle velocities as a function of particle diameter, geometry and viscosity (Muller, 2012). The same model was extended by Spigarelli et al. that performed particle tracing with different channel aspect ratios (Spigarelli, 2020). A full 3D numerical simulation was reported by Skov et al., which took into account many physical parameters, namely the transducer, the silicon base, the fluid with bulk and boundary layers, the lid and the microparticles suspended. They demonstrated similarities between simulations and previous experiments regarding acoustic radiation forces, velocities and trajectories (Skov, 2019).

As it emerged from the previous literature research, the state of the art for the numerical simulations in the acoustic field is represented by a comparison between numerical and experimental results. For this reason, in the context of this project, the numerical simulations were used for the initial investigation of the ultrasound field distribution in the experimental set-up tested with the other techniques previously described, using an approach similar to Tiong et al. (Tiong, 2017) and Yasui et al. (Yasui, 2007).

The model used in this Master Thesis was developed by Spigarelli et al. (Spigarelli, 2020) for an acoustophoretic device, and it was simplified and slightly modified for the purpose of the present work. In details, this model is based on the perturbation theory, which permits to decompose the properties that describe the phenomenon in series of orders (zeroth, first and second order, for acoustophoresis). The acoustic perturbations represent slight deviations from the equilibrium values of pressure and velocity; however, for the initial investigation of the US field in the domain in static conditions, it was decided to leave out the velocity field and to focus only on the pressure field, whose perturbation series was decided to stop at the first order field, as it is described by the following equation:

$$p = p_0 + p_1 \tag{2.15}$$

In the equation (2.15), the zeroth order (p_0) represents the pressure equilibrium state of the fluid at which the first order pressure perturbation (p_1) is added. This first order field is simulated by solving the harmonic linearized Helmholtz equation in the frequency domain, which can be written in the following form:

$$\nabla^2 p = -\frac{\omega^2}{c^2} p \tag{2.16}$$

Where ω is the angular frequency, p is the harmonic pressure field and c is the sound speed in water. The solution is the sound pressure p that represents the acoustic variations with respect to the ambient equilibrium pressure.

The simulated domain is represented only by the fluid inside the container, while the solid material of the container, the interface between the water and the material above it, and the actuation by the US transducer are described by specific boundary conditions, explained in details in the “Materials and Methods” section. Moreover, the fluid is considered homogeneous and isotropic, and the entropy is conserved due to adiabatic assumption (Spigarelli, 2020), as for many acoustic applications. However, considering the specific ultrasound application, damping can take place through interaction with surrounding solid materials and viscous boundary layer at walls.

To conclude this brief theoretical introduction, the choice of this work was to simulate the most studied set-up, namely the single well environment, in order to clarify some results obtained in the experiments and analyse the pressure energy distribution and the impact of experimental parameters on it.

3 Materials and Methods

3.1 Sonochemiluminescence experiments

The experimental set-up for sonochemiluminescence (SCL) experiments was characterized by the ultrasound transducer, the container with the Luminol solution and the digital camera fixed on a tripod, in order to frame the solution inside the container.

The basic components for the Luminol solution were made ready in advance and subsequently the right volume of solution was always prepared just before conducting the experiments and it was used within 4 hours from the preparation. First of all, sodium hydroxide (NaOH, Sigma-Aldrich) was dissolved in double distilled water in order to obtain 1 L of solution at a concentration of 0.1 M, which was kept in a glass tank in the laboratory. The solution pH was measured with a pH-meter (VWR) to be sure we have obtained an alkaline solution (pH = 12). Secondly, H_2O_2 (30%) was diluted in double distilled water in order to obtain a concentration of 0.02 M and stored in glass bottle. Then, for every SCL experiment, the necessary aliquots of NaOH and H_2O_2 were withdrawn from these stock bottles and mixed in a Falcon with the other components for obtaining the concentrations explained in the following.

- NaOH, added in the necessary volume for the experiments.
- H_2O_2, added in the proper volume for obtaining a concentration of $5 \cdot 10^{-4}$ M.
- Luminol 97 % (Sigma-Aldrich), which was kept in the fridge at 4°C, was added in order to obtain a concentration of 80 mM.
- Nanoparticles (NPs): withdrawn from a previously prepared water suspension for obtaining a final concentration of 200 μg/mL. Different types of NPs available in the laboratory were applied: Titanium dioxide functionalized with aminopropyl groups (TiO_2-NH_2), Zinc oxide functionalized with aminopropyl groups (ZnO-NH_2), developed by the TrojanNanoHorse Research group, and Zinc oxide (ZnO, IoLiTec) coming from a commercial nano-powder, characterized by an average particle size of 20 nm and a purity of 99.5 %.

The Luminol alkaline solution so prepared was always mixed in the Falcon by agitation, for some seconds, and sonication in the US bath, for 1-2 minutes (depending on the volume), for a good dispersion of all the different components. In conclusion, due to the Luminol reactivity with light exposure, the falcon containing the solution was always covered with an aluminium sheet.

The ultrasound transducer used for this purpose is the LipoZero G39 (Globus), a commercially available and approved medical device, used to generate unfocused US waves for aesthetic purposes and treatments, such as liporeduction and cutaneous flaw.

Figure 3.1: Body (left) and head with the US transducer (right) of the LipoZero device.

As depicted in Figure 3.1 above, the instrument is composed by two elements: the body that can be connected with the plug to fully operate and it contains a screen reporting the parameters for the sonication, and the head, which contains piezoelectric crystals that vibrate and generate US at the set frequency. The parameters used for the sonication are reported in the following:

- Duty cycle (DC): 100 %
- Frequencies: 150 KHz, 526 KHz, 1 MHz, 3 MHz
- Output power: 100 % (corresponding to 3 W/cm^2)
- Sonication time: 1-2 min

Several containers were filled with the Luminol solution and placed on the transducer's surface:

- A polystyrene (PS) single well coming from a 24-well plate (Nunc™ Non-Treated Multidishes) (Figure 3.2a);
- A PS petri dish (Falcon®) (Figure 3.2b);
- The PMMA cartridge of the Therakos® Cellex Photopheresis system, tested both in the original configuration (closed channel, Figure 3.2c) and without the top plate (open channel);
- Portion of the silicon tubes coming from the Therakos® Cellex Photopheresis system (Figure 3.2d).

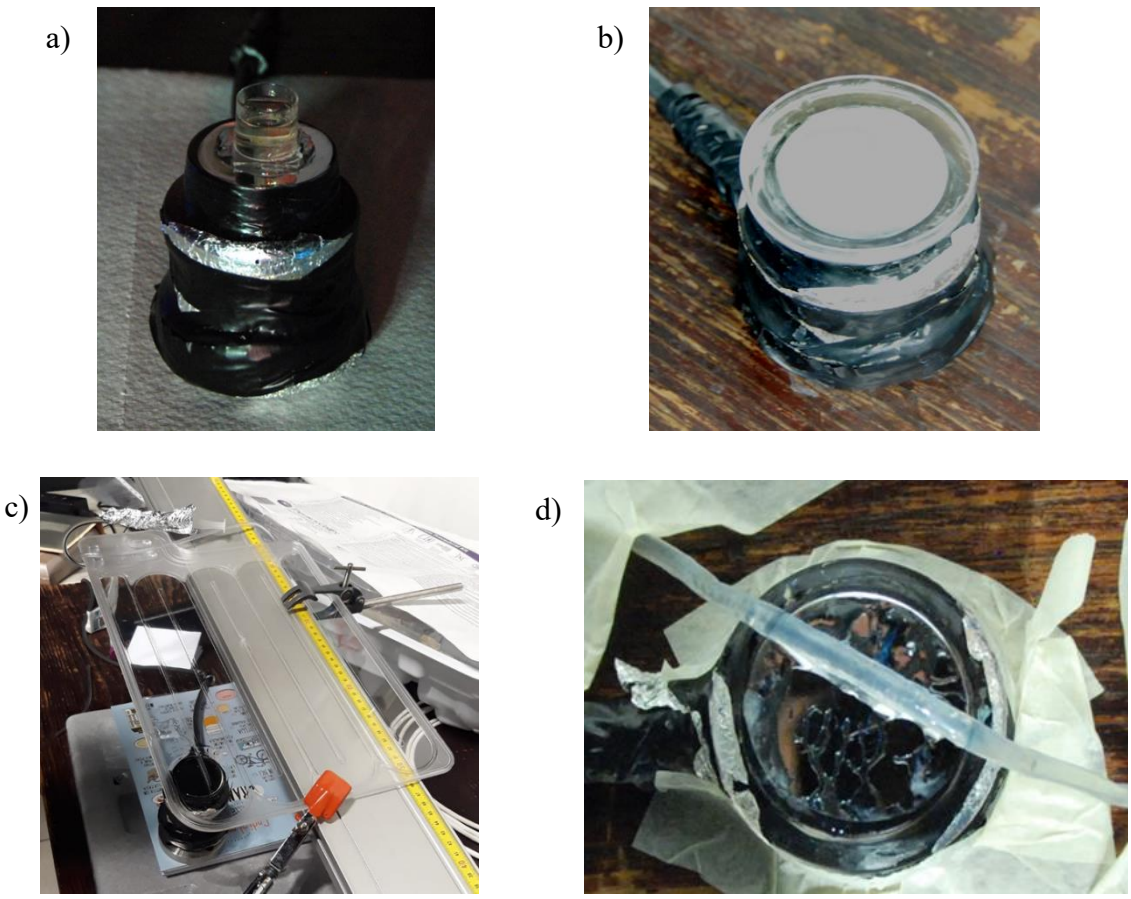

Figure 3.2: Containers used for SCL experiments: a) single well, b) petri dish, c) cartridge in the original configuration placed on the inclined plane, d) single tube held it fixed by tape on the US transducer plane.

In every experiment where the container was in contact with the US transducer, a thin layer of coupling gel (ELvation) was applied for the correct transmission of US waves.

Luminol SCL in a single PS well was evaluated under a wide range of experimental conditions: different liquid heights, presence and absence of covers made of different materials, different irradiation frequencies and distances of the well from the transducer. The main geometrical features of the single well useful for the experiments, extracted from the datasheet, are reported here: bottom diameter = 15.5 mm, top diameter = 16.3 mm. Thus, the average diameter is 15.9 mm. Moreover, the average bottom thickness is 1.77 mm, calculated as average among different measures made with a calibre.

The cover materials used, whose sound characterization is exposed in the Results section, are the following:

- A thin layer of Polydimethylsiloxane (PDMS);
- Polystyrene (PS), represented by the bottom of a second well;

- Squared Borosilicate glass for microscopy (Prestige);
- PMMA, represented by a small part of one plate of the Cellex cartridge;
- Ethylene propylene diene monomer rubber (EPDM rubber), a sound absorbing material;
- A thin layer of cork;
- A thin layer of expanded PS.

They were always placed on the free surface of the sonicated solution in order to simulate a closed environment. For this purpose, the well was completely filled with Luminol solution (V = 3 mL) and the cover was gently placed on it. The only exception is represented by the PDMS cover, which was cut in the same round shape of the well and placed inside it, on the free surface of 2 mL of solution. Furthermore, in order to study the effect of the well distance from the transducer, different kinds of spacer have been used:

- A layer of coupling gel with a thickness of ~ 1 cm. For this purpose, the gel has been confined using cylinders without the bases of two types: a smaller one made of plastic (Figure 3.3 left), completely in contact with the transducer, and a bigger one made of rubber (Figure 3.3 right), which can be inserted around the transducer so that it is not in contact with the latter. Due to the viscous characteristics of the gel, the same layer was also obtained without any object for the confinement.

Figure 3.3: Small (left) and big (right) cylinder used for the confinement of the layer of coupling gel.

- A tank much bigger than the transducer was filled with water. The transducer was fixed at the bottom of the tank (Figure 3.4 left) and the well was kept at different distances from it using a support with arms, so that the bottom of the well was in contact with the free surface of water (Figure 3.4 right).

Figure 3.4: Transducer fixed in the bottom of the tank used for the creation of the distance with water (left) and arrangement of the well with arms on the free surface of water (right).

The digital camera used for the acquisition of SCL images was a Nikon D80 model, set on the manual setting with the following characteristics: ISO 1250, f/4, exposure time = 1 – 2 min. These settings were the ones with best results, obtained after a first study on the best acquisition set-up, reported in the Results section. The camera was placed in different positions depending on the purpose of the study: above, next to or diagonally with respect to the container.

To perform the sonication and related SCL image acquisition, the experimental set-up was built in a dark room, trying to remove every possible light source from the environment. The US irradiation and the video-camera acquisition were started and ended at the same time, so that the acquisition time was always equal to the sonication time.

The SCL images acquired with the digital camera were analysed using the open source ImageJ software, a Java image processing and analysis program. In particular, the jpeg images acquired are colour images in 24 bit, in which every pixel display a value in the range 0 – 255 ($2^8 = 256$ values) for each of the three channels: Red, Green and Blue. Due to the Luminol emission in the blue light, a deep study on the Blue value was carried out in the analysis, which was performed on Region of Interest (ROI) identified on each image. The parameters used for the comparisons between different pictures are the following:

- Intensity profile, which displays a "column average plot", where the X-axis represents the horizontal distance through the ROI selected and the Y-axis the vertically averaged pixel intensity. The used ROI included also background areas in order to visualize the different shape of the SCL profile between the luminescent pixels and the dark ones.
- Intensity statistics (mean and max values of the pixels in the ROI), obtained through the RGB Measure tool. In this case, the ROI included just the actual luminescent pixels.

3.2 Electron Paramagnetic Resonance experiments

The experimental set-up for EPR measurements is characterized by the US transducer (LipoZero), the container with the solution, and the EPR spectrometer (EMXNano X-Band spectrometer from Bruker).

The containers used for these experiments were the ones with most interesting results obtained in the previous SCL experiments, namely the PS single well from the 24 well-plate (Nunc™) and the cartridge of the Therakos® Cellex Photopheresis system, both in the original configuration (closed channel) and without the top plate (open channel).

The parameters set on the LipoZero device and used for the sonication were the following: DC = 100%, frequency = 1 MHz, output power = 100% (corresponding to 3 W/cm^2), sonication time = 1 min.

The evaluation of ROS production was provided by the EPR spectroscopy assisted by a spin-trapping technique. For this purpose the solution in the containers was composed by the following elements:

- Double distilled water,
- 5,5-dimethyl-L-pyrroline-N-oxide (DMPO, Sigma), previously prepared in 1% v/v, was added in order to obtain a final concentration of 10% v/v,
- Commercial ZnO NPs, in a concentration of 200 μg/mL. They were added only in the samples called “ZnO”, and not in the control ones.

To perform the sonication, the container was filled with 2 or 3 mL of solution, depending on the sample, and it was placed on the surface of the transducer by interposing a thin layer of coupling gel. After the irradiation, the sample was immediately transferred into a quartz microcapillary tube and positioned into the EPR cavity. For the spectra acquisition, the following parameters were set on the machine:

- Centre field: 3426 G,
- Sweep width: 100 G,
- Sweep time: 60 s,
- Sample g-factor: 2.00000,
- Number of scans: 10.

After the acquisition, the spectra were processed using the Bruker Xenon software (Bruker) for the correction of the baseline and subsequent analysis were performed using the Bruker SpinFit software.

3.3 Temperature measurements

The temperature increase in the solution inside the single well and in the 1-cm thick gel layer used as spacer, were recorded using a temperature sensor. Different experimental set-up were tested, namely different volumes (1, 2, 3 mL), presence/absence of different covers (PS, EPDM rubber, PMMA, cork) and well distancing from the transducer by a thick gel layer. The irradiation characteristics of the LipoZero device tested were the following: DC = 100 %, frequencies = 526 KHz, 1 MHz, output power = 100 % (corresponding to 3 W/cm^2), sonication time = 1 min.

For conducting the experiments, the single well was filled with the proper volume of double distilled water that simulated the Luminol solution and it was positioned on the US transducer. The initial temperature was measured and then, after 1 min of sonication, the temperature was measured again. It should be noted that when the US were turned off, the temperature kept increasing for some seconds before starting to decrease, so the maximum value reached in this amount of time was took as final temperature value.

3.4 Numerical Simulations

The numerical simulation were implemented using a model that described only the fluid inside the single well. A list of the main parameters used for the simulation is reported in the following table.

Table 3.1: Parameters used for the simulation of the well filled with water. The water parameters are taken from (Spigarelli, 2020).

Parameter	Symbol	Value
Well radius	r	0.008 [m]
Liquid height	H	0.005, 0.01, 0.015 [m]
Frequency of actuation	f	$1.00 \cdot 10^6$ [Hz]
Speed of sound in water	c_0	1497 [m/s]
Density of water	ρ_0	998 [kg/m^3]
Dynamic viscosity of water	μ_0	$8.9 \cdot 10^{-4}$ [Pa·s]
Bulk viscosity of water	μ_b	$2.4852 \cdot 10^{-3}$ [Pa·s]

Inward displacement	I_0	$3.13 \cdot 10^{-8}$ [m]

The fluid model chosen was the viscous one, described by speed of sound (c_0), density (ρ_0), dynamic viscosity (μ_0) and bulk viscosity (μ_b). The initial value for the pressure in the domain is set to be 0 Pa, and the actuation of the fluid through the bottom side of the well is modelled using a harmonically oscillating boundary condition. In particular, this condition adds an inward normal displacement assumed to be harmonically oscillating, whose value takes into account the presence of the polystyrene bottom thickness. For this purpose, the polystyrene sound attenuation coefficient α was calculated using the following formula (Takagi, 2007):

$$\propto = \frac{k\gamma^2\rho}{2C_p^2V}T\omega^2 \qquad (3.1)$$

Where k (thermal conductivity), γ (thermal expansion coefficient), ρ (material density), C_p (heat capacity) and V (sound velocity) referred to the PS, while T is the reference temperature and ω is the angular frequency of sound. Using the values reported by Spigarelli et al. (Spigarelli, 2020), α resulted to be 0.108 cm^{-1}. This value was used to calculate the actual intensity that reaches the fluid inside the well, through the following formula:

$$I(x) = I_0 e^{-2\propto x} \qquad (3.2)$$

Where I_0 (3 W/cm^2) is the intensity corresponding to 100% of power set in the LipoZero device, and x (1.7 mm) corresponds to the bottom thickness of the well. The so calculated intensity, that takes into account the passage in the PS bottom thickness, is 2.89 W/cm^2. Finally, this value (I) was used in equation (3.3) below, for the calculation of the displacement (s) of water molecules, due to the US transducer actuation.

$$I = \frac{P^2}{2\rho c} = \frac{(c\rho\omega s)^2}{2\rho c} \qquad (3.3)$$

$$s = \sqrt{\frac{2I}{\rho c\omega^2}} \qquad (3.4)$$

Equation (3.4) is derived from Equation (3.3), in which P represents the wave pressure amplitude, ρ is the water density, c is sound velocity in water and ω is the angular frequency. The obtained value for s, namely $3.13 \cdot 10^{-8}$ m, was set as inward normal displacement (I_0, Table 3.1) on the bottom boundary, for the US actuation of the fluid.

The lateral walls are modelled by impedance boundary conditions, represented by the specific acoustic impedance of the external domain, in this case the PS, whose acoustic impedance value is reported in the Results section (Single well: influence of experimental parameters, Influence of the cover).

The interface between the water and the overlying material is modelled by another impedance boundary condition, represented by the specific acoustic impedance of the external domain. In this case, different external domains were used for the study of the effect of air and other materials (EPDM, cork, PS, glass) on the propagation of US in the domain. Their acoustic impedance values are reported in the Results section (Single well: influence of experimental parameters, Influence of the cover).

The geometry was modified with respect to the starting model developed by Spigarelli et al. (Spigarelli, 2020), in order to obtain a cylinder that resemble the well, characterized by a base radius of 0.008 m (r) and an height (H) that corresponds to the liquid volume. In order to study the effect of the liquid height, three different H values were simulated: 0.005 m, 0.01 m, and 0.015 m, corresponding to 1 mL, 2 mL and 3 mL. Then, for the study of the effect of the cover, the H value was fixed at 0.015 m (corresponding to 3 mL) and the impedance boundary condition on the top was set to simulate the actual acoustic impedance of the cover's material.

The results of the simulations show the acoustic pressure field and the intensity magnitude distribution in the domain. Moreover, some post-processing variables were calculated: the average viscous power dissipation density in the domain, for the analysis of the energy losses due to viscosity; the average intensity magnitude in the domain; and the absorption coefficient for normal incidence on the top side of the domain, for the evaluation of the cover's energy absorption.

Regarding the mesh, the dimensions were decided to have a good balance between the precision of the results and the computational time required. The boundaries were discretized using extremely fine element size, while the bulk domain was discretized using extra fine element size. This choice was in line with the starting model regarding the distinction between the boundaries and the bulk: in the firsts the values vary faster and the results should be more detailed, while in the second the use of slightly bigger elements should not interfere with the outcome. The 3D mesh obtained for the well with a liquid height H = 0.01 m and used for the simulations is shown in Figure 3.5 below.

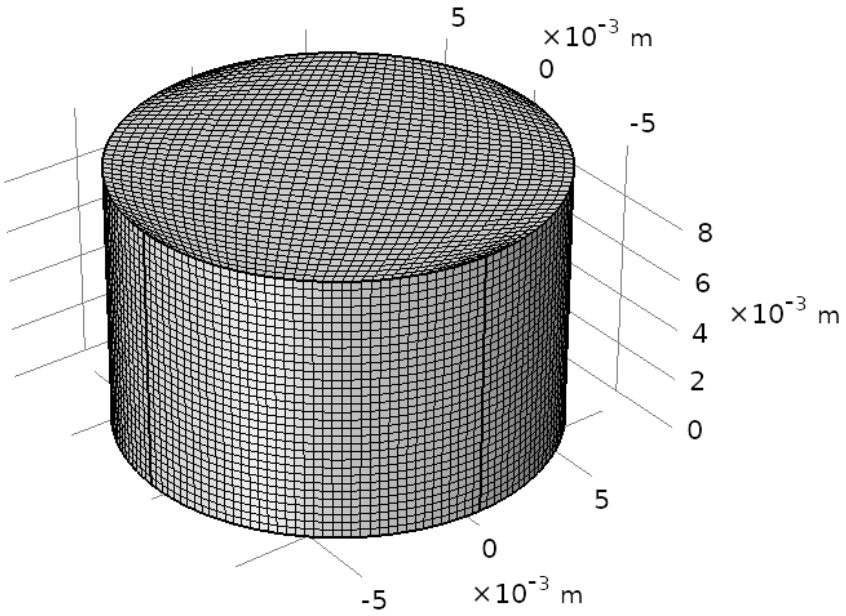

Figure 3.5: 3D mesh used for the simulations: well with 2 mL of solution, corresponding to H = 0.01 m.

4 Results and Discussion

4.1 Sonochemiluminescence experiments

4.1.1 Single well

The investigation of SCL started from a simple system, represented by the PS single well, in order to analyse different video camera acquisition set-up and understand which could be the best one. For this purpose, the same solution (V = 1.9 mL) composed only by NaOH, Luminol and H_2O_2 was used for all the tests.

Table 4.1: Comparison between different acquisition set-ups on the video camera.

Acquisition set-up	Images	Comment
ISO = 1600 f / 4.5 T_{exp} = 1 min	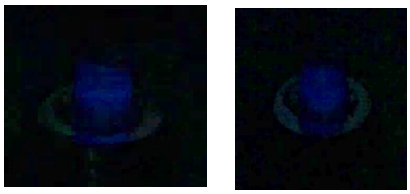	/
ISO = 1000 f / 4.5 T_{exp} = 2 min		Solution already sonicated 2 min
ISO = 1250 f / 4 T_{exp} = 2 min	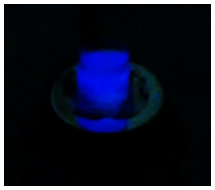	Solution already sonicated 4 min

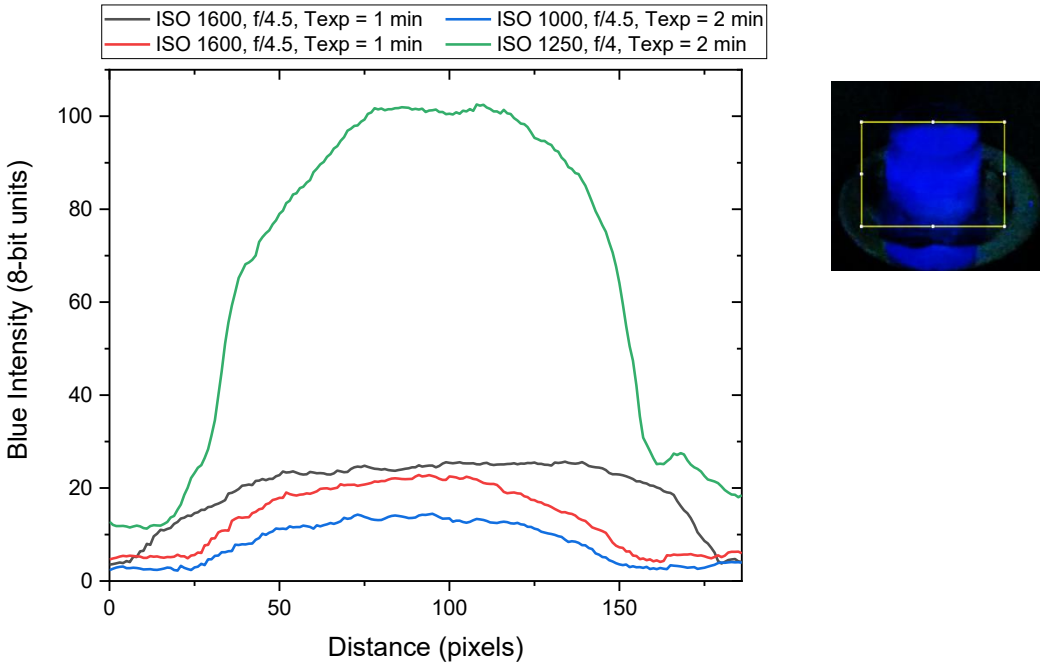

Figure 4.1: Blue intensity profiles of the three different acquisition set-up tested (left) and ROI selected for the analysis (right).

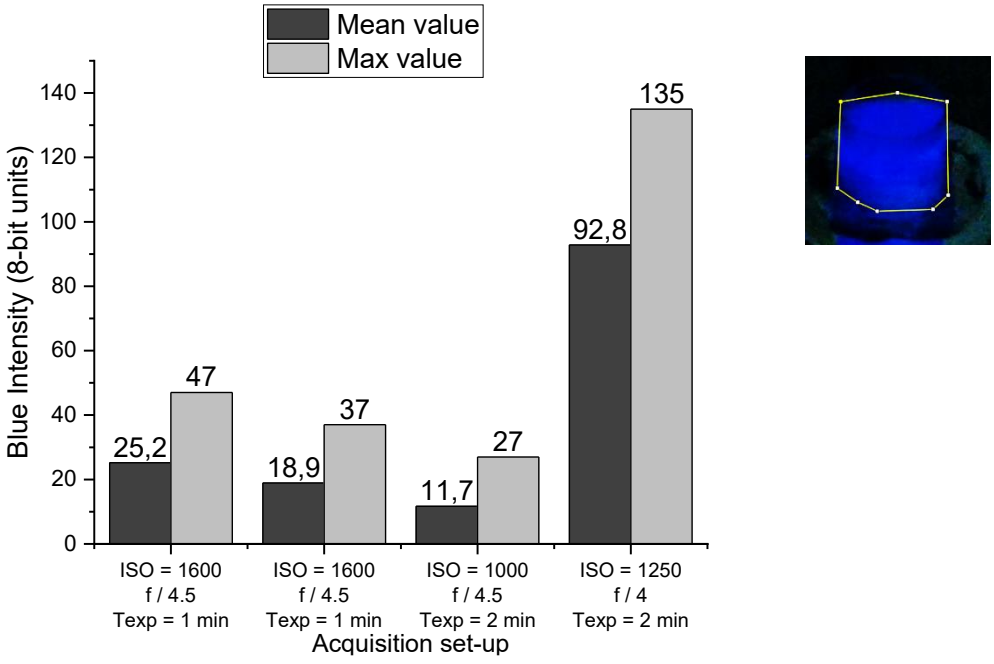

Figure 4.2: Blue intensity statistics for the three different acquisition set-up tested (left) and ROI selected for the analysis (right).

From the intensity profiles (Figure 4.1), the green curve (representing the set-up ISO 1250, f/4, T_{exp} = 2 min) shows the highest values of intensity, while the others set-ups share similar and lower profiles. Regarding the statistics (Figure 4.2), the first and second samples share the same camera set-ups even if the second one shows slightly lower values, probably due to the fact that the solution was already sonicated. The setting with the lowest ISO value (ISO = 1000) also

shows the lowest intensities, even if the exposure time is 2 minutes and the last set-up (ISO 1250, f/4, T_{exp} = 2 min) is characterized by the highest intensity statistics. It should be remembered that the solution used for these tests was always the same, for this reason sonicated more than one time. Finally, the best set-up identified here (ISO 1250, f/4, T_{exp} = 2 min) was kept as reference and maintained in the following experiments regarding the ISO value, while f-number and T_{exp} were slightly modified in some experiments.

Thereafter, a preliminary test on the effects of Luminol SCL by three kinds of NPs was conducted.

Table 4.2: Comparison between solutions with and without different types of NPs. Acquisition set-up: ISO 1250, f/4, T_{exp} = 2 min.

Solution	Volume (mL)	Image	Comment
Luminol solution (without NPs)	1.9	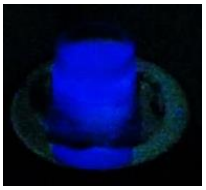	Solution already sonicated 4 min
Luminol solution + TiO_2-NH_2	2	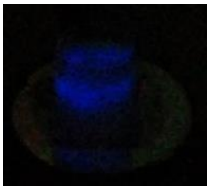	/
Luminol solution + ZnO_2-NH_2	2	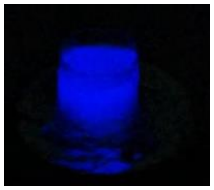	/
Luminol solution + ZnO	2	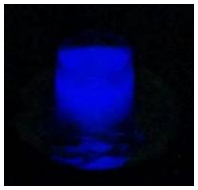	/

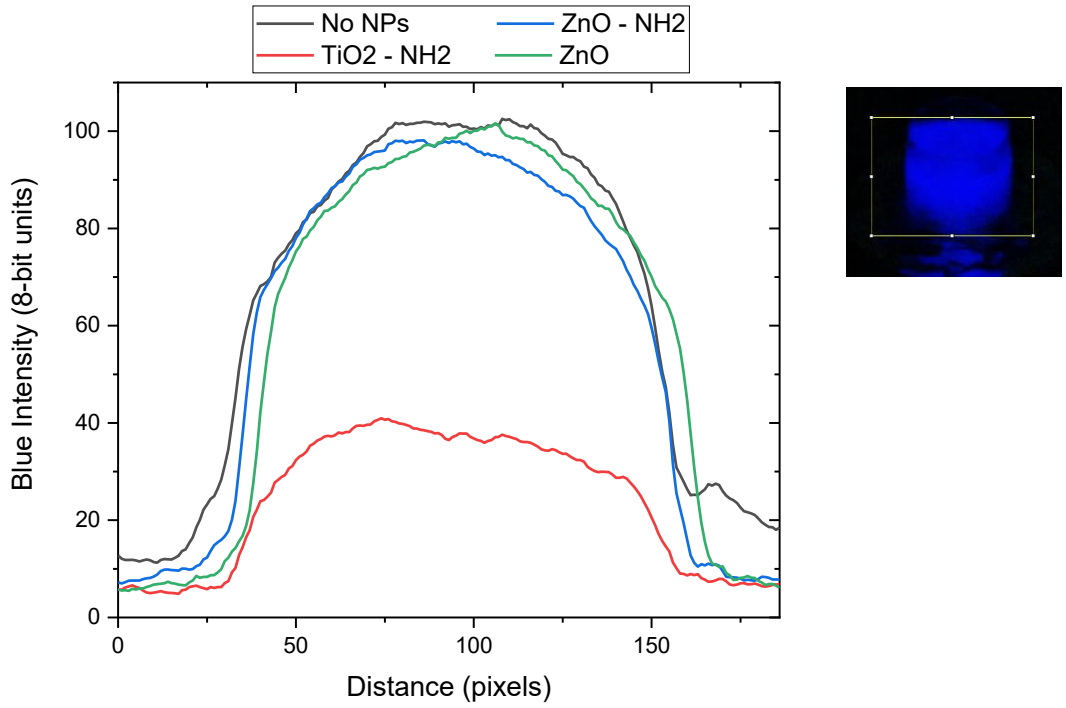

Figure 4.3: Blue intensity profiles of the samples with and without NPs (left) and ROI selected for the analysis (right).

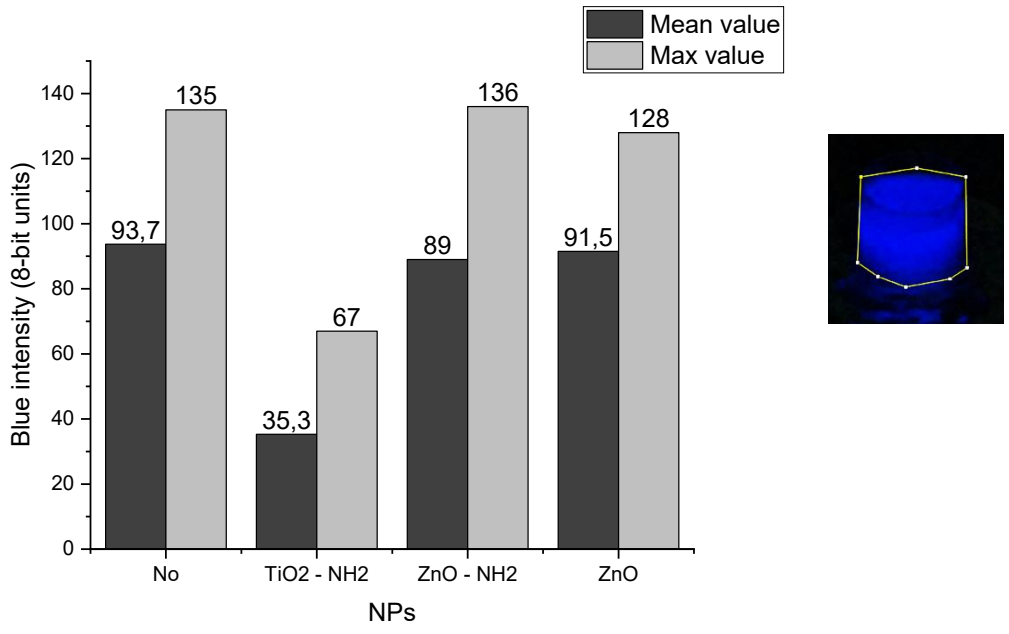

Figure 4.4: Blue intensity statistics of the samples with and without NPs (left) and ROI selected for the analysis (right).

Surprisingly, the solution without NPs shows a profile (Figure 4.3, black line) comparable to solutions with ZnO NPs (Figure 4.3, blue and green lines). Comparing the three different NPs used: TiO_2 shows the lowest profile, while ZnO-NH_2 and ZnO have similar profiles. For this reason, the best ROS production may be related to the presence of ZnO NPs. Moreover, the solutions without NPs and with ZnO NPs are comparable regarding all statistics values (Figure

4.4), which are better than the values of the solution containing TiO_2. It should be noted that the solution without NPs is the same presented in the previous experiment of the single well, already sonicated 4 minutes, and it has been reported here for comparisons with solutions containing different NPs, that were not sonicated before. It can be concluded that the best results were obtained with ZnO NPs, for this reason it has been decided to use only them in the following experiments, in particular the commercial ZnO ones, also due to higher availability in the laboratory and lower production costs.

4.1.2 Petri dish

The petri dish was used for the investigation of the number of possible sonication cycles using the same Luminol solution and the duration of the solution under light exposure. For these experiments, a volume of 5 mL was used and the acquisition set-up was the following: ISO 1250, f/4.8, T_{exp} = 1 min.

Table 4.3: Sonication cycles of the same Luminol solution in a petri dish.

US application cycle (T = 1 min)	**Image**	**US application cycle (T = 1 min)**	**Image**
1		4	
2	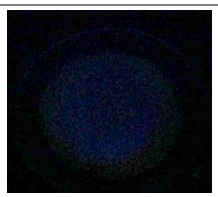	5	
3		6	

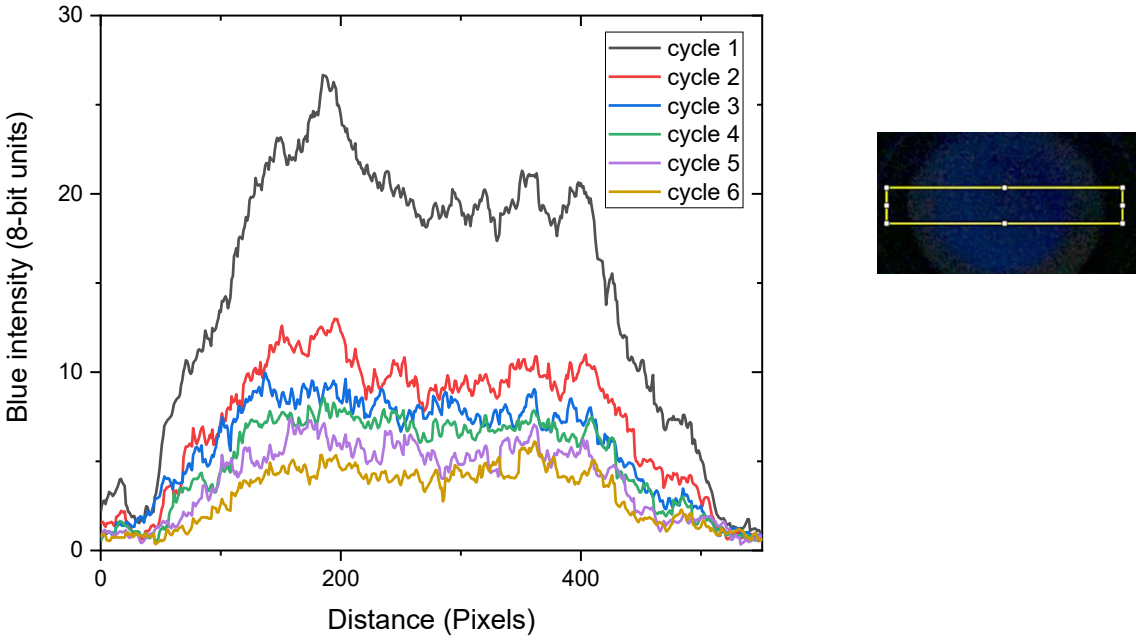

Figure 4.5: Blue intensity profiles of the six consecutive sonication cycles (left) and ROI selected for the analysis (right).

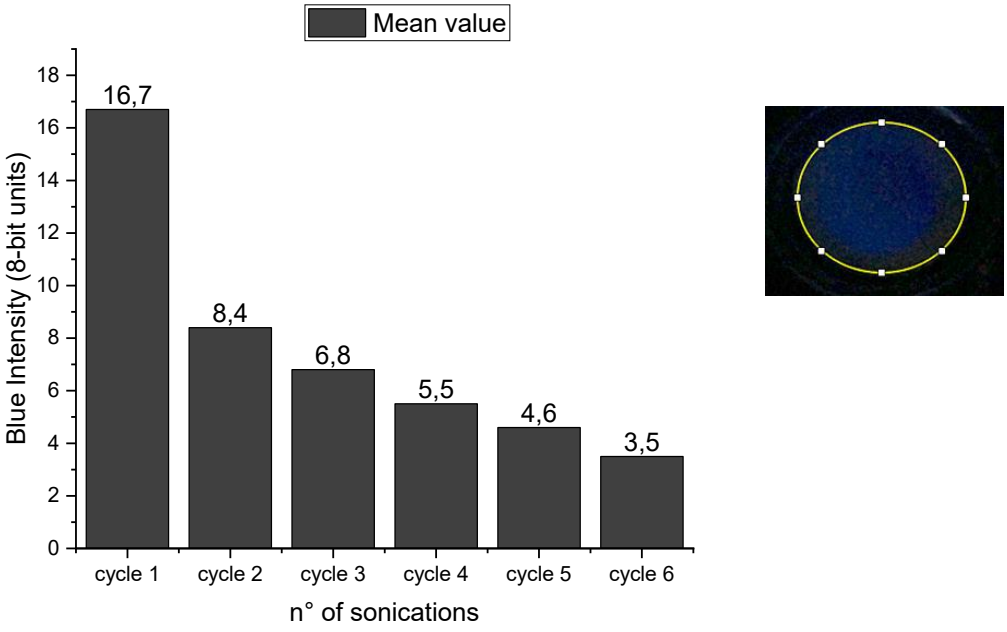

Figure 4.6: Blue intensity statistics of the six sonication cycles (left) and ROI selected for the analysis (right).

As it was expected, the blue profiles (Figure 4.5) and the intensity statistics (Figure 4.6) confirm that in the same solution the produced SCL decreases proportionally to the number of applied sonications, due to a decreasing number of available (not already reacted) Luminol and ROS molecules to generate SCL. In particular, the higher difference is observable between the first

and the second sonication cycle, while after that the decrease of SCL intensity is less pronounced.

Table 4.4: Duration of the solution under light exposure.

Duration of exposure to light (min)	Type of light	Image
/	Dark	
25	Outdoor light	
25 (outdoor) + 5	Indoor light	

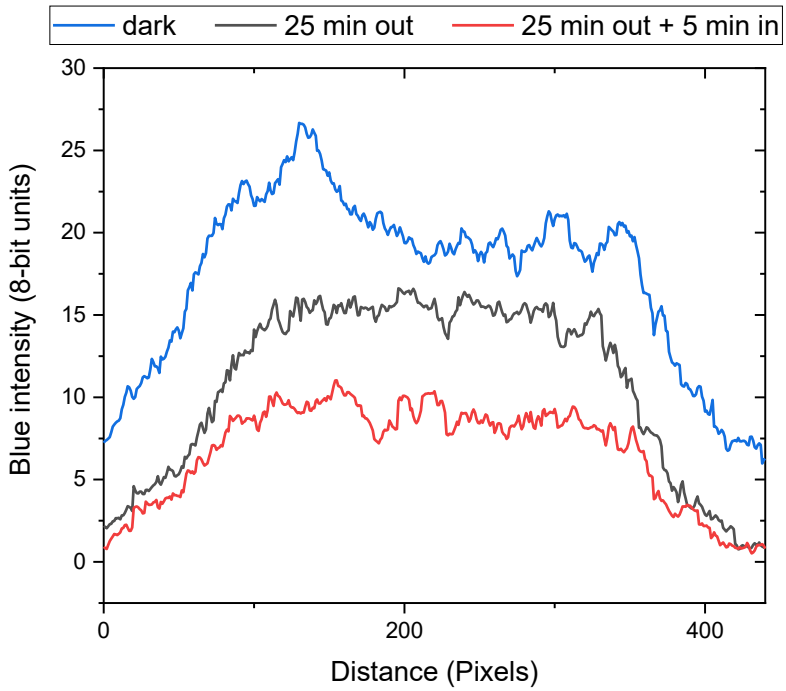

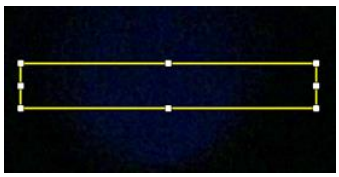

Figure 4.7: Blue intensity profiles of samples with different time exposure to light (left) and ROI selected for the analysis (right).

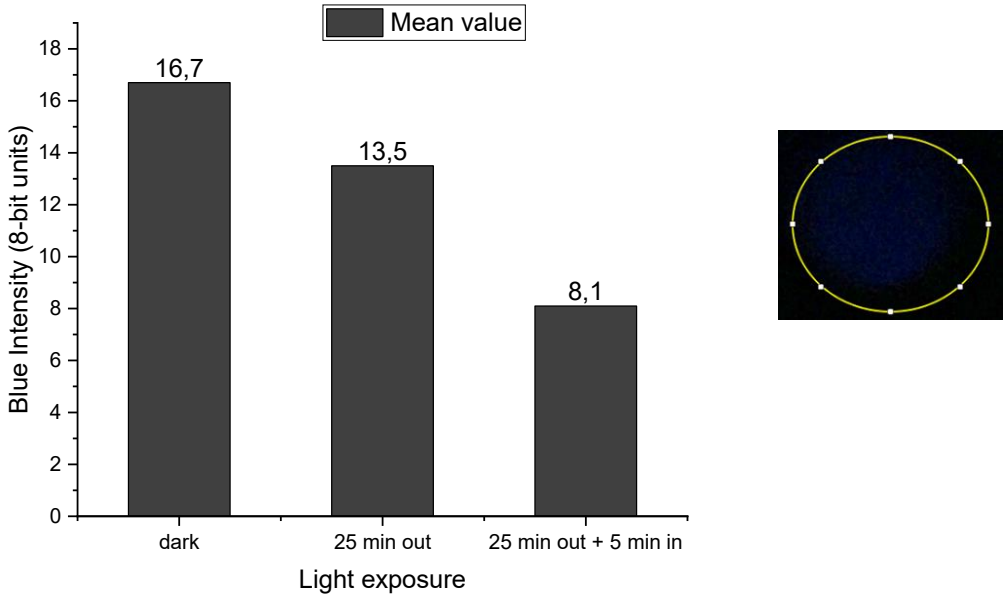

Figure 4.8: Blue intensity mean values of samples with different time exposure to light (left) and ROI selected for the analysis (right).

The analysis confirms the hypothesis that SCL reaction is reduced if the molecules of the Luminol solution are previously exposed to light, maybe due to the development of a certain photoactivation process: the SCL intensity profile of the 25 minutes light exposed solution is lower than the solution sonicated once in the previous study (reported here as "dark" sample, Figure 4.7). Moreover, after the second light exposure the SCL intensity decreases clearly (Figure 4.8). It must be remarked that after the second exposure, the solution is also subjected to a second cycle of sonication, which contributes to the SCL reduction. It can be noticed that the intensity of the sample "25 min out + 5 min in" (Figure 4.8) is close to the intensity of the sample "cycle 2" of the previous experiment (Figure 4.6), therefore it seems that two US treatments to the solution have a similar effect of a ~ 30 minutes light exposure.

Due to these conclusions, the falcon containing the fresh Luminol solution for the experiments was always covered with an aluminium sheet in order to reduce its reaction with light, and the sample solution was always changed within 2-3 cycles of sonication in order to be able to make right comparisons between different experimental set-ups.

4.1.3 Single well: influence of experimental parameters

Previous experiments of SCL showed best results in the single well set-up, for this reason it has been decided to deeply analyse this condition. More in details, the objective of this section is to study the influence of different experimental parameters on the SCL obtained in a single

well, namely the liquid height in the well, the presence of covers made of different materials, the frequency applied by the US transducer and the distance of the well from the transducer.

Influence of the liquid height

For studying the influence of the liquid height, the well was filled with different volumes (range 1 – 2 mL), corresponding to different liquid heights, calculated with the following formula:

$$H = \frac{V_{sol}}{\pi \cdot r_{well}^2} \qquad (4.1)$$

Table 4.5: Influence of the liquid height in the SCL in a single well.

Volume (mL)	Liquid height (mm)	Images	
		Control (NO ZnO)	ZnO
2	10.078	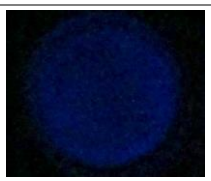	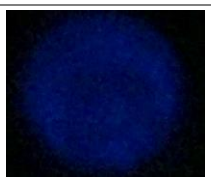
1.9	9.574		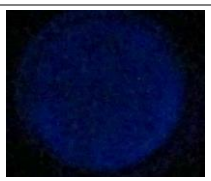
1.8	9.070	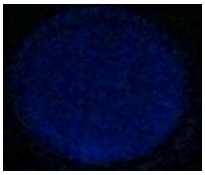	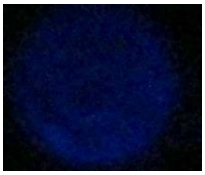
1.7	8.566	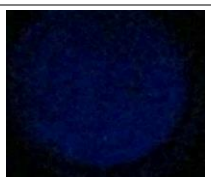	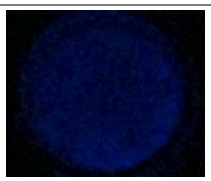
1.6	8.062	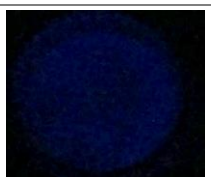	

1.5	7.558	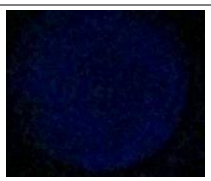	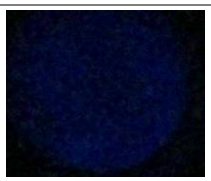
1.4	7.054		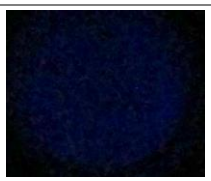
1.3	6.551		
1.2	6.047		
1.1	5.543		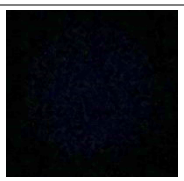
1	5.039		

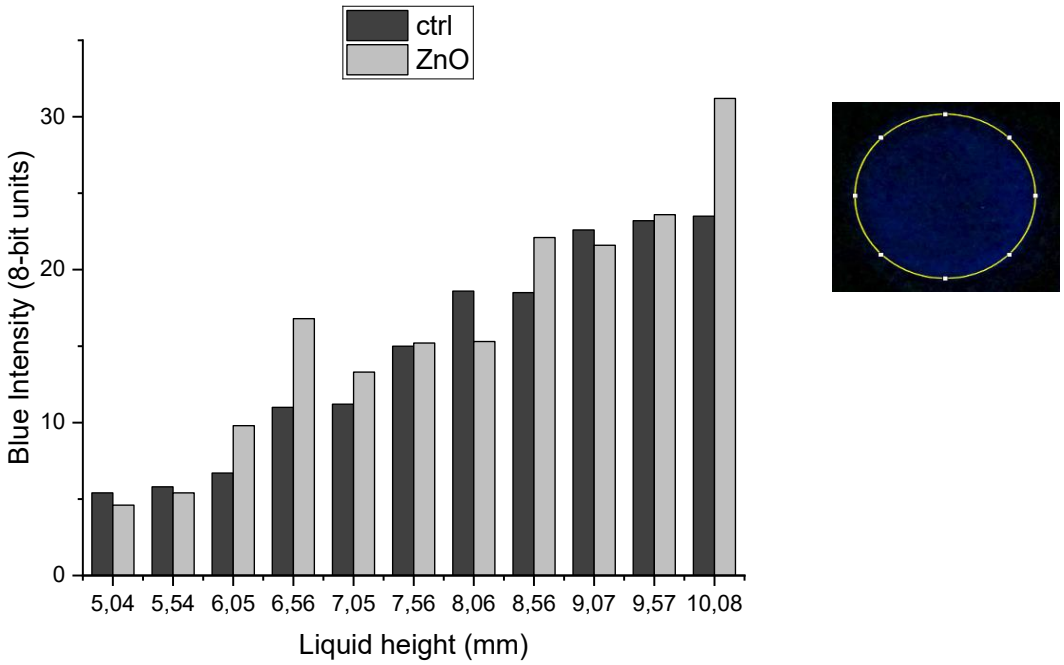

Figure 4.9: Blue Intensity mean values for the samples with different liquid heights tested (left) and ROI selected for the analysis (right).

For these samples it was decided to show only the mean intensity values and not the profiles, because it was more significant and less confusing. As it was expected, the detected blue light intensity produced by the SCL phenomenon results to increase by increasing the solution volume (height), since the amount of Luminol (together with the other reagents) increases: this means that more molecules react, more emit light. In particular, it can be observed from Figure 4.9 that the increase follows a general monotonic linearity for both the ZnO and the control solution. For some heights, there are slight differences from this linear and monotonic behaviour, represented by higher or lower increments with respect to the linear one: this fact can be related to unavoidable experimental errors and different light conditions of the environment. Unfortunately, from this kind of experiment it was not possible to associate the particular trend to specific physical phenomena (such as resonance), and also attribute specific SCL variations to a certain range of volumes, because they do not follow a regular behaviour.

By comparing the mean values of the control and the ZnO solutions, it can be observed that globally the SCL intensity generated by the ZnO solution is higher than the control one, as expected by the increased radicals production thanks to the NPs; in particular, the difference is clear in the sample with 2 mL as volume (Figure 4.9, 10 mm of liquid height). This behaviour does not occur for all the samples, but in seven out of eleven, therefore, it can be concluded that the commercial ZnO NPs applied can help to produce radicals, but without a strong enhancement.

It has been chosen to use a minimum volume of 1 mL, since the previously higher sonicated volumes already confirmed the expected behaviour, and because for values equal or lower than 1 mL, it is more and more difficult to have a detectable SCL. Additionally, from the pictures in Table 4.5, it can be observed a higher SCL at the lateral surfaces of the well with respect to the SCL detected in the centre: this effect could be caused by a stronger US field at the sides of the well, which produces more cavitation and so more hydroxyl radicals reacting with the Luminol molecules. A software simulation on the US field distribution could be useful to clarify this hypothesis.

Influence of the distance from the transducer

In this section, the results of the effect of the well distance from the transducer are discussed. In Table 4.6 below, there are two different references (Ctrl_1 and Ctrl_2) used for the analysis because images were obtained in two different days.

Table 4.6: Results of the samples with spacer: gel. A layer of 1 cm thickness was obtained using different objects for the gel confinement: small cylinder, big cylinder or no object (unconfined samples).

Volume (mL)	Spacer	Image	Comment
2	/	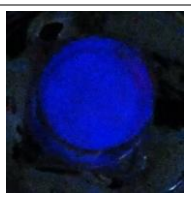	Ctrl_1
2	Gel (small cylinder) ~ 1 cm	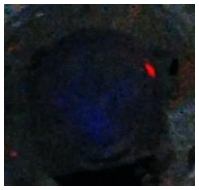	/
2	Gel (unconfined) ~ 1 cm	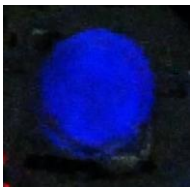	/
2	Gel (unconfined) ~ 1 cm	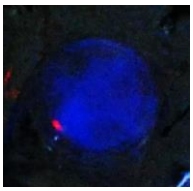	Solution already sonicated 1 min

2	/	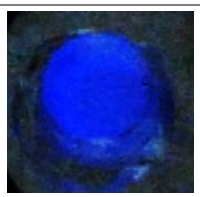	Ctrl_2
2	Gel (big cylinder) ~ 1 cm	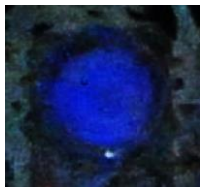	/

Table 4.7: Results of the samples with spacer: water.

Volume (mL)	Spacer	Image	Comment
2	Water (~ 1 mm)	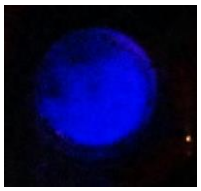	/
2	Water (1 cm)	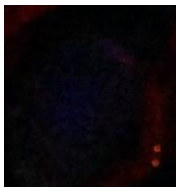	/
2	Water (2.4 cm)		/
2	Water (3.7 cm)	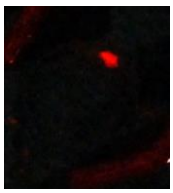	Solution already sonicated 1 min
2	Water (6 cm)		Solution already sonicated 1 min

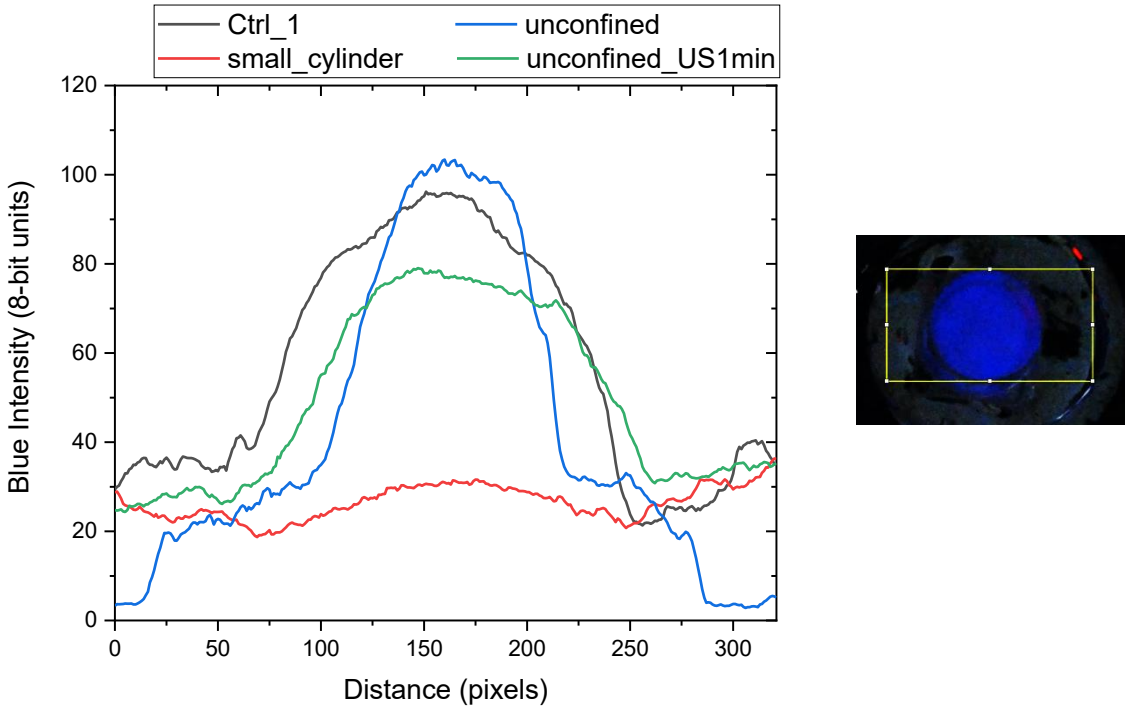

Figure 4.10: Blue intensity profiles of the samples with spacer gel that refer to Ctrl_1 (left) and ROI selected for the analysis (right).

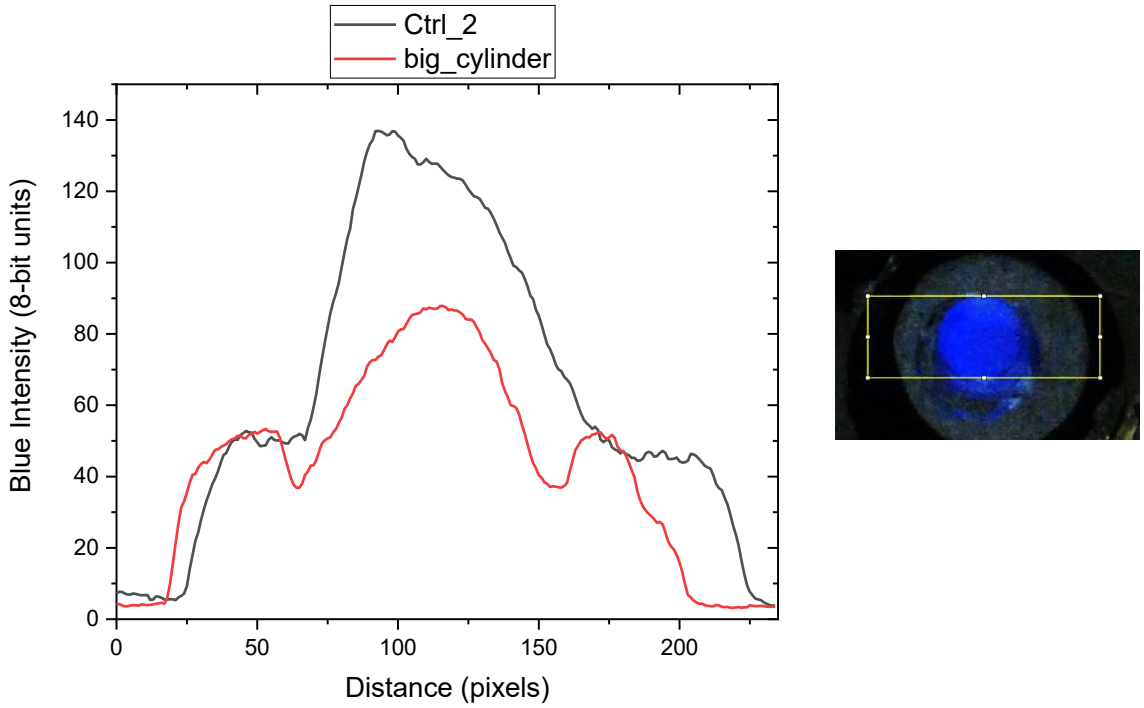

Figure 4.11: Blue intensity profiles of the sample with spacer gel that refer to Ctrl_2 (left) and ROI selected for the analysis (right).

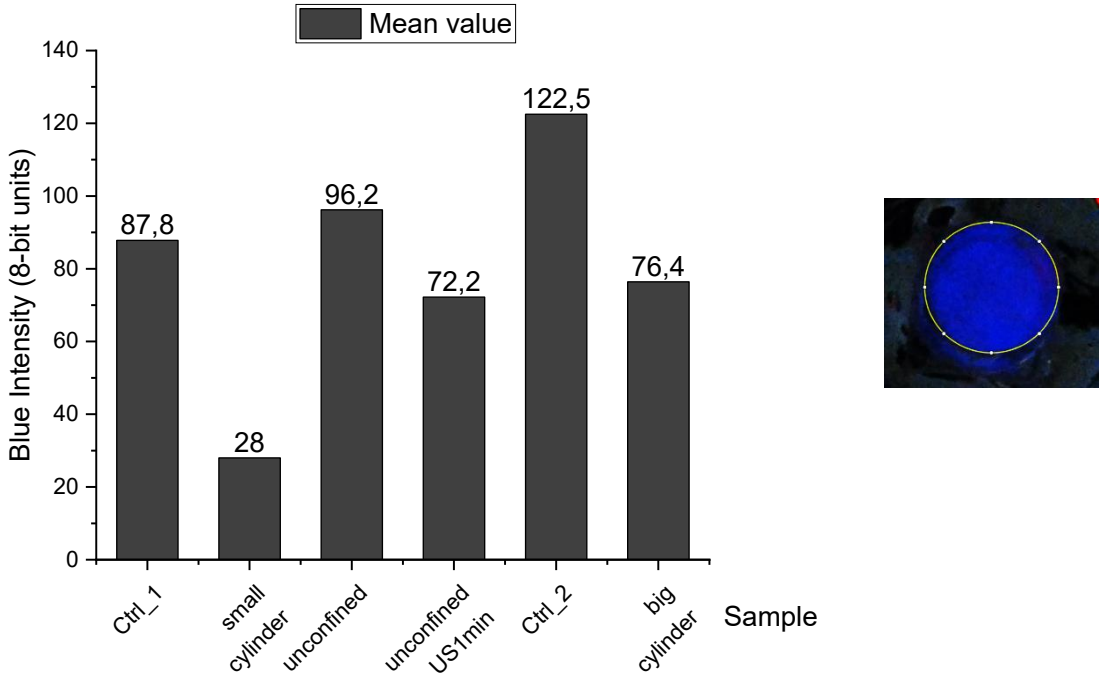

Figure 4.12: Blue intensity mean values of the samples with spacer gel: small cylinder, unconfined, unconfined_US1min refer to Ctrl_1, big cylinder refers to Ctrl_2 (left). ROI selected for the analysis (right).

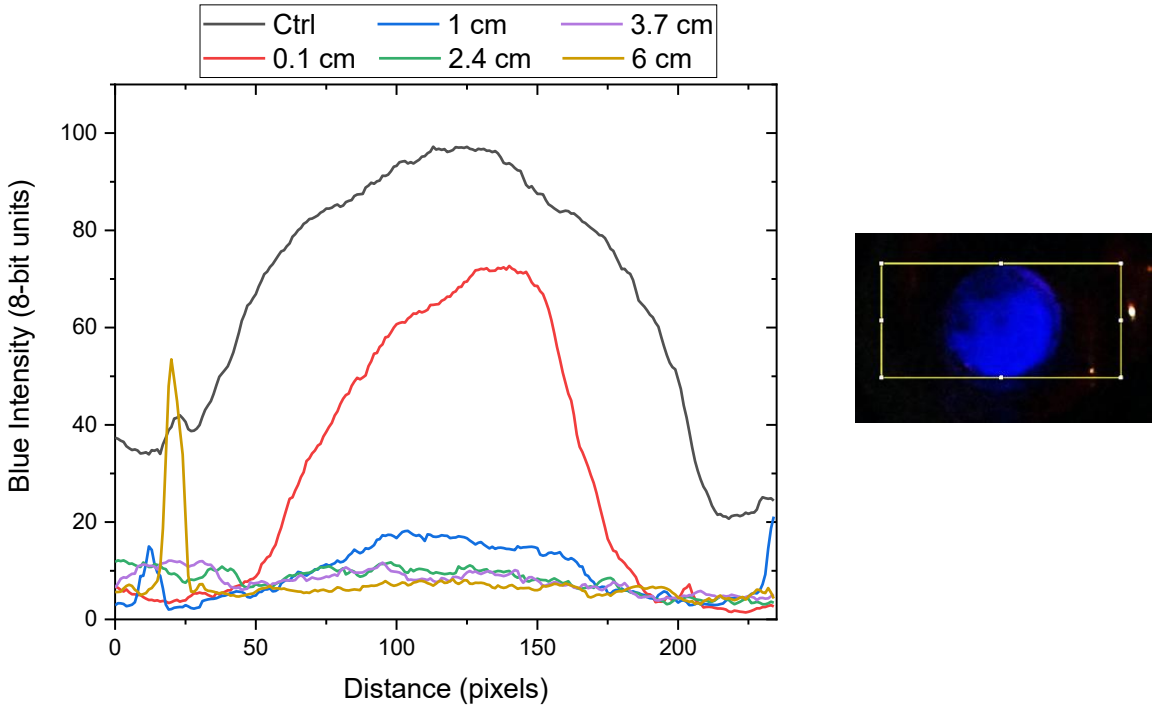

Figure 4.13: Blue intensity profiles of the samples with spacer water (left) and ROI selected for the analysis (right).

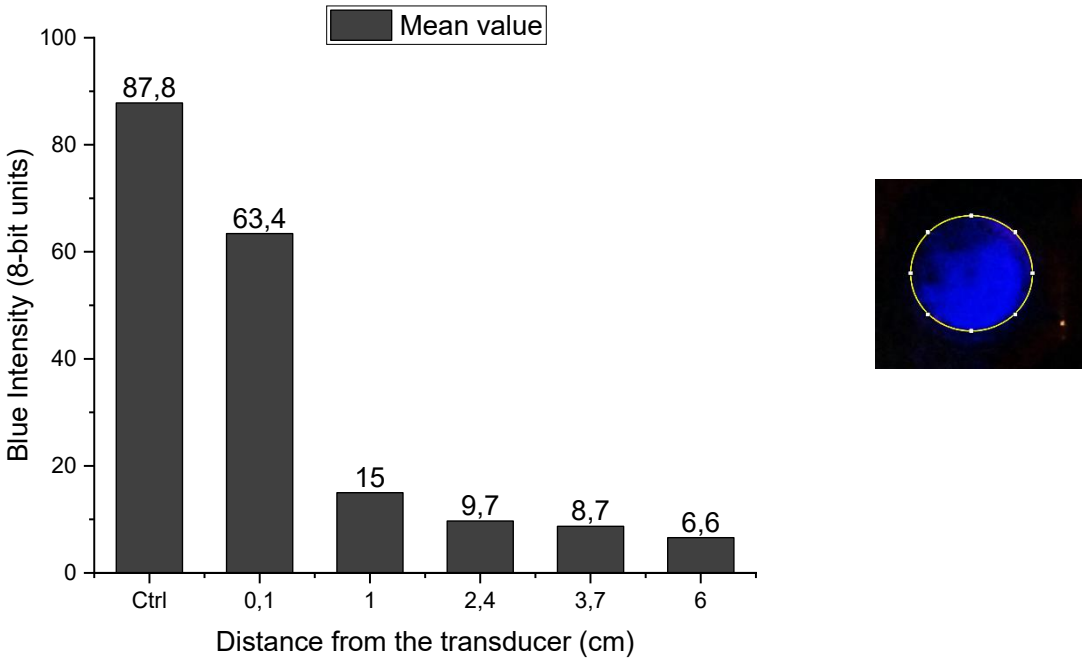

Figure 4.14: Blue intensity mean values of the samples with spacer water (left) and ROI selected for the analysis (right).

Regarding the use of the coupling gel as spacer, it is clear that the materials used for the confinement of the gel have huge impact on the SCL results: using the small cylinder, which is completely in contact with the transducer, intensity profiles and mean values are much lower with respect to the control (difference of 60 units between Ctrl_1 and small_cylinder, Figure 4.12). When the big cylinder was used, results obtained were a bit better, showing a difference of 46 units (big_cylinder with respect to Ctrl_2, Figure 4.12). The better results were obtained when the layer of coupling gel was free: surprisingly in this set-up the mean intensity value is higher with respect to the control (Figure 4.12, unconfined with respect to Ctrl_1). As a first conclusion, the presence of an additional material on the transducer is related to the US wave energy absorbance, for this reason it is better to avoid its presence on the transducer. Moreover, it should be noticed that a thick gel layer heats up and can dampen the US wave, with a related modification of the viscosity of the coupling medium and consequently alteration of the propagation of US.

In the case of using water as spacer, it is clear the reduction of SCL with the distance from the transducer (Figure 4.13, Figure 4.14). SCL can be observed only when the well is very close to the transducer (Table 4.7, distance = ~ 1 mm), while at 1-cm distance it is already hard to be seen, with a reduction of 72 units with respect to the control. In this experiments the presence of a big system with additional elements inside of it, impossible to remove, is related to a big

energy dispersion: for this reason it is not the better set-up for the distancing from the transducer.

Influence of the cover

In this section, SCL in a single well was investigated in the presence and absence of covers made of different materials. Table 4.8 below shows the sound characterization of these materials, with the calculation of acoustic impedance (Z) and reflection (R) and transmission (T) coefficients for the interface between the Luminol solution and the cover. For parameters whose value is not unique, it is reported a range of possible values found in the literature, and the mean of this range is used for the calculation.

Table 4.8: Acoustic characterization of materials used as covers for studying their effect on SCL.

Material	Density (kg/m^3)	Sound speed (m/s)	Acoustic Impedance ($\cdot 10^6$ Rayl)	R	T	Bibliographic reference
Water	998	1497	1.5	/	/	(Spigarelli, 2020)
Air	1.3	343	0.000446	-1.0	0.0	(Sabri, 2013)
PDMS	1000	1076 - 1119	1.076 – 1.119	-0.2	0.8	(Xu, 2020) (Guillermic, 2019) (Tsou, 2008)
PS	1050	2350	2.5	0.2	1.2	(Spigarelli, 2020) (Beekers, 2018)
Glass (borosilicate)	2510	5710	14.3	0.8	1.8	(Beekers, 2018)
PMMA	1200	2757	3.3	0.4	1.4	(Beekers, 2018)
EPDM (sound absorbing)	900 - 2000	279	0.25 – 0.56	-0.6	0.4	(Hawass, 2015) (Fei, 2018)
Cork	100 - 250	500	0.05 – 0.125	-0.9	0.1	(Berardi, 2015)
Expanded PS	15 - 100	2350	0.035 – 0.24	-0.8	0.2	(Horvath, 1994) (Lakatos, 2013)

It should be taken into account that, in this section, images were acquired in two different ways, due to the type of cover present on the solution: for the transparent materials (PDMS, PS, glass, PMMA) images were acquired from the top of the well, while for the non-transparent materials (EPDM, cork, expanded PS) images were acquired from one side of the well. For this reason, the background of these last images (Table 4.10) is much brighter with respect to the others (Table 4.9) and it was deleted for the construction of the profile. Moreover, for PS and PMMA

covers, images were acquired also from one side and their SCL values are higher with respect to the images acquired from the top, due to the different environmental light (different laboratory) and related background luminescence.

Table 4.9: Influence of the covers on the SCL in a single well, images acquired from the top of the well.

Volume (mL)	Cover	Image	Comment
3	Air (Ctrl)	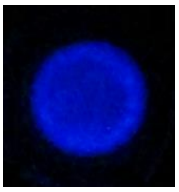	Solution already sonicated 60 s
2	PDMS		Solution already sonicated 90 s
3	PS		/
3	Glass (borosilicate)	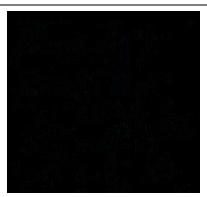	T_{exp} = 45 s (problem with the camera)
3	PMMA	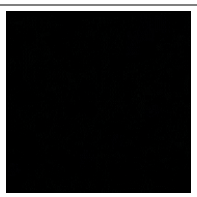	/

Table 4.10: Influence of the covers on the SCL in a single well, images acquired from one side of the well.

Volume (mL)	Cover	Image	Comment
3	Air (Ctrl)		Solution already sonicated 60 s
3	EPDM (sound absorbing)		/
3	PMMA	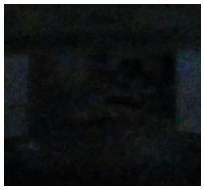	/
3	PS		/
3	Cork	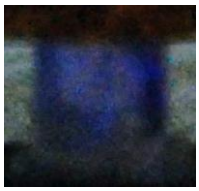	/
3	Expanded PS		/

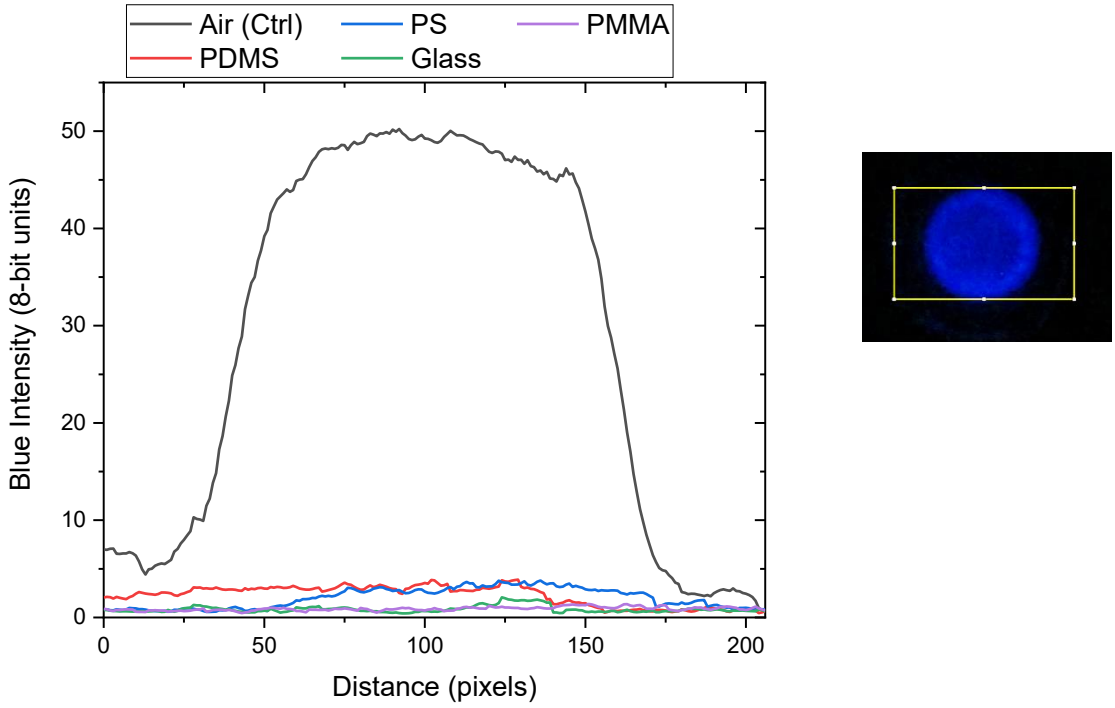

Figure 4.15: Blue intensity profiles of samples reported in Table 4.9 (left) and ROI selected for the analysis (right).

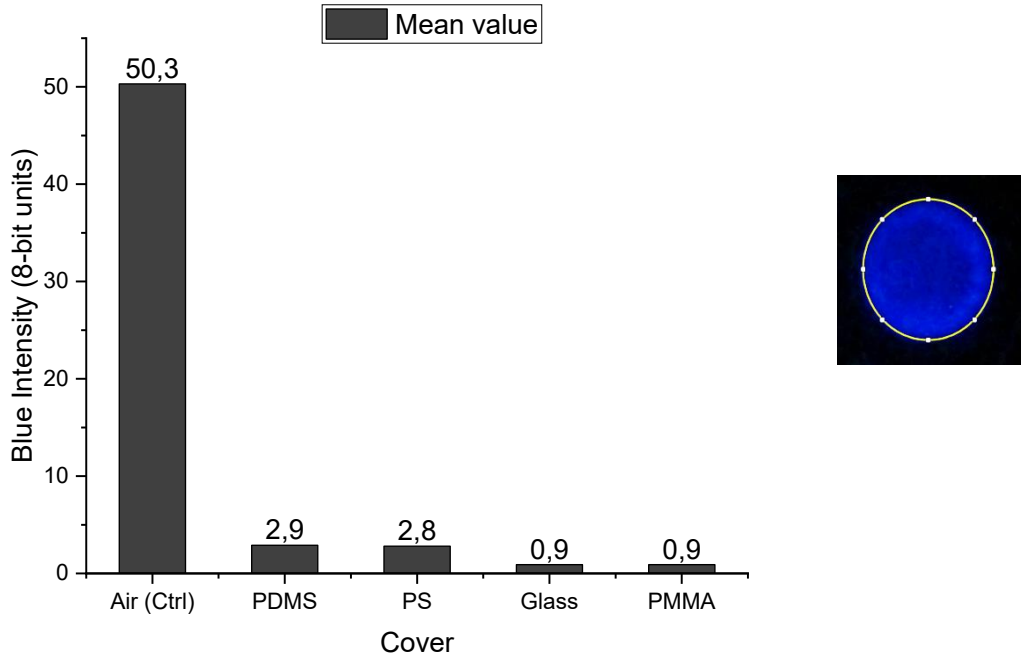

Figure 4.16: Blue intensity mean value of samples reported in Table 4.9 (left) and ROI selected for the analysis (right).

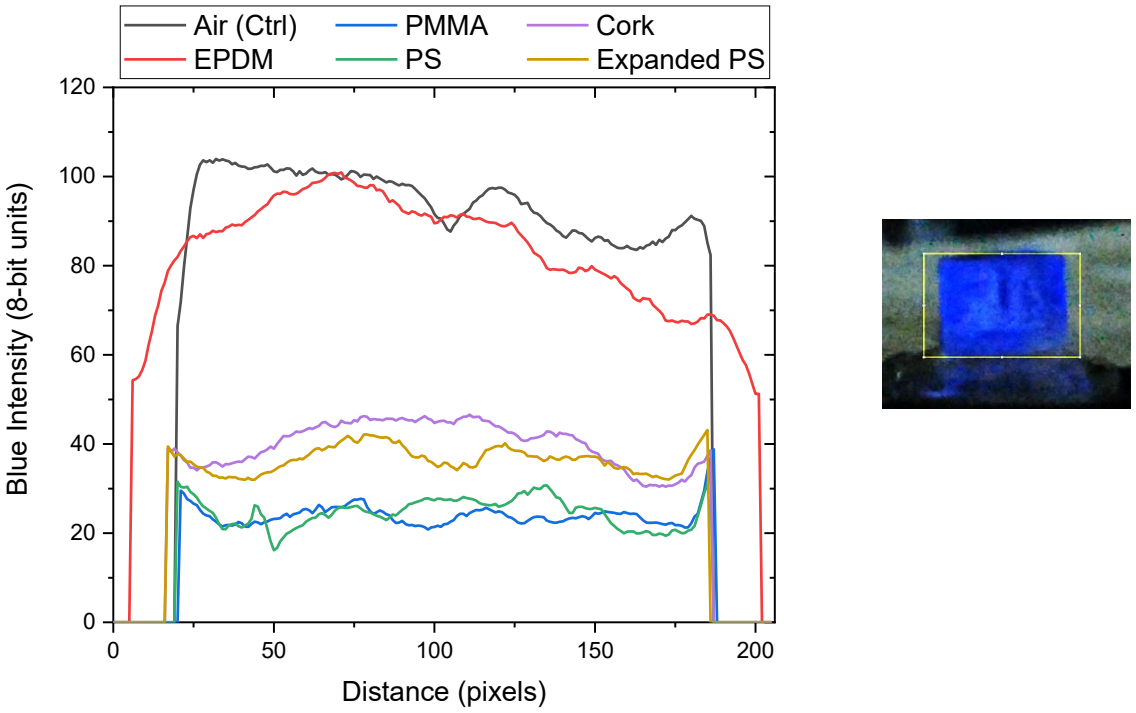

Figure 4.17: Blue intensity profiles of samples reported in Table 4.10 (left) and ROI selected for the analysis (right).

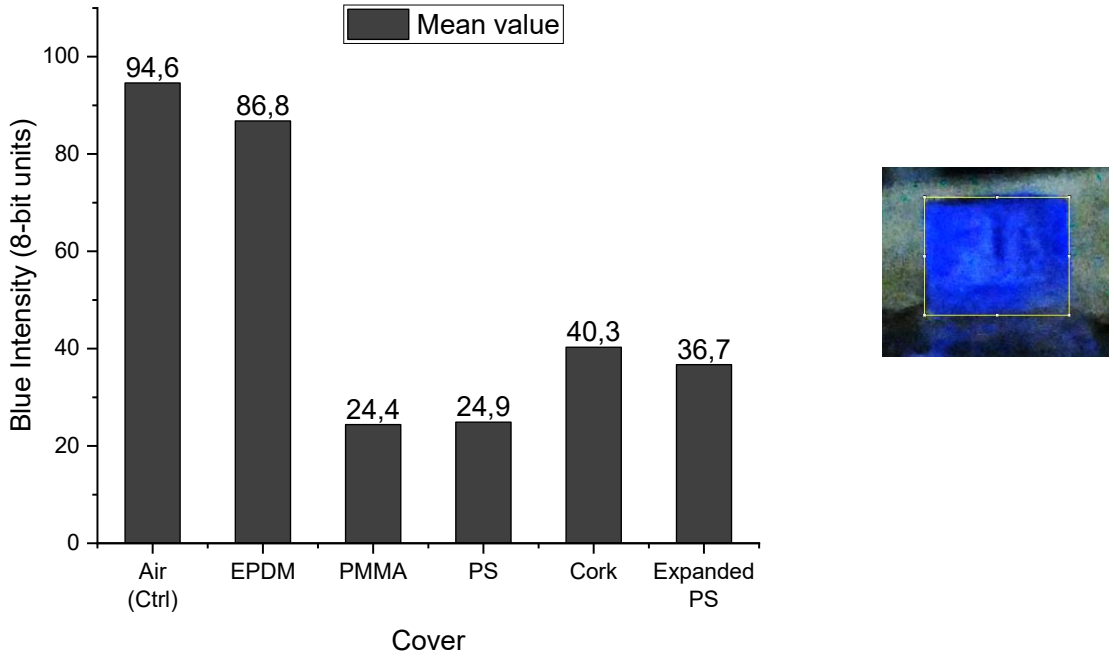

Figure 4.18: Blue intensity mean values of samples reported in Table 4.10 (left) and ROI selected for the analysis (right).

Covers with high acoustic impedance values (PDMS, PS, glass and PMMA, reported in Table 4.8) and relatively higher than the air value, show the effect of SCL suppression that can be seen both from profiles (Figure 4.15) and mean value (Figure 4.16). In details, the difference is

between 50.3 units (Figure 4.16, Ctrl) and 0.9 - 2.9 units (Figure 4.16, other covers). On the other hand, the covers that better mimic the air acoustic impedance (EPDM, cork, expanded PS, reported in Table 4.8) show better results: the sound absorbing material (EPDM) has profile (Figure 4.17, red line) and mean intensity value (Figure 4.18, EPDM) very close to the reference (Figure 4.18, Ctrl). Cork and expanded PS show similar results regarding profile (Figure 4.17, violet and yellow line) and mean value (Figure 4.18), both better than the other types of covers, but with SCL values much lower than the reference and the sound absorbing material.

From these experiments it can be concluded that when the US wave, which is propagating in the solution, encounters a material with higher acoustic impedance with respect to water (PS, glass, PMMA), SCL cannot be seen and measured. The cover in PDMS is a particular case because it shows an acoustic impedance value lower than water, even if very close to it, anyway SCL cannot be seen when it is present. On the other hand, when the US encounters a material with lower acoustic impedance with respect to water (EPDM, cork, expanded PS), SCL is detectable and measurable. A more in-depth physical study on the role of reflection and transmission at the interface water-cover could be conducted, in order to clarify if the US wave that generates SCL is represented by a standing or a travelling wave in the solution.

Finally, it should be noticed that the mean intensity value for the control solution (Figure 4.16 and Figure 4.18) is higher with respect to values obtained in the previous experiment (Figure 4.9) because the volume used in here is higher (3 mL with respect to 2 mL). This result follows the trend emerged before in which SCL increases when the solution volume increases.

Influence of the frequency

In this section, the results regarding the effect of different US frequencies (3 MHz, 1 MHz, 526 KHz, 150 KHz) on the SCL in a single well are reported. Additionally, the effect of some covers is evaluated and confirmed at different frequencies.

Table 4.11: Influence of the US frequency on the SCL in a single well.

Volume (mL)	Frequency (KHz)	Cover	Image
2	3000	Air	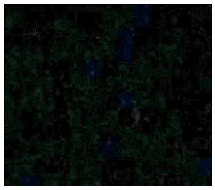

2	526	Air	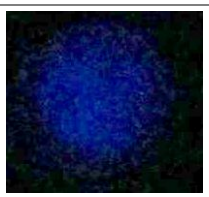
2	150	Air	
3	526	Air (Ctrl)	
3	526	PDMS	
3	526	Glass	
3	526	PS	
3	526	PMMA	
3	150	Air (Ctrl)	

3	150	PDMS	
3	150	Glass	
3	150	PS	
3	150	PMMA	

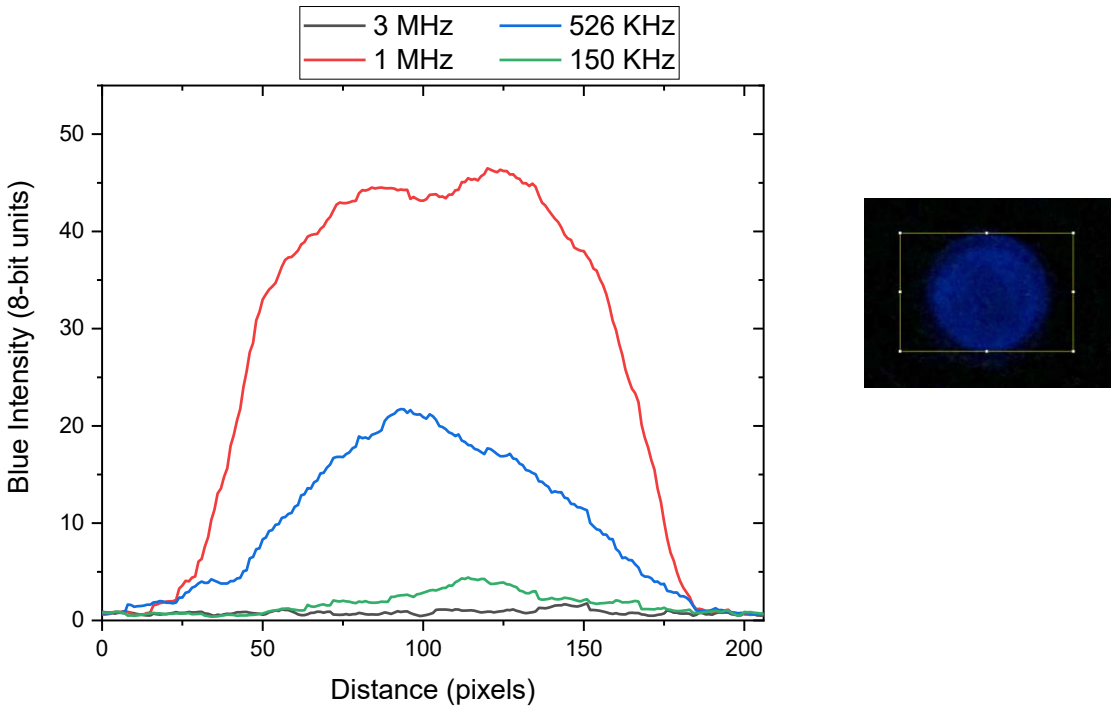

Figure 4.19: Blue intensity profiles of samples with V: 2 mL, different frequencies, cover: Air (left) and ROI selected for the analysis (right).

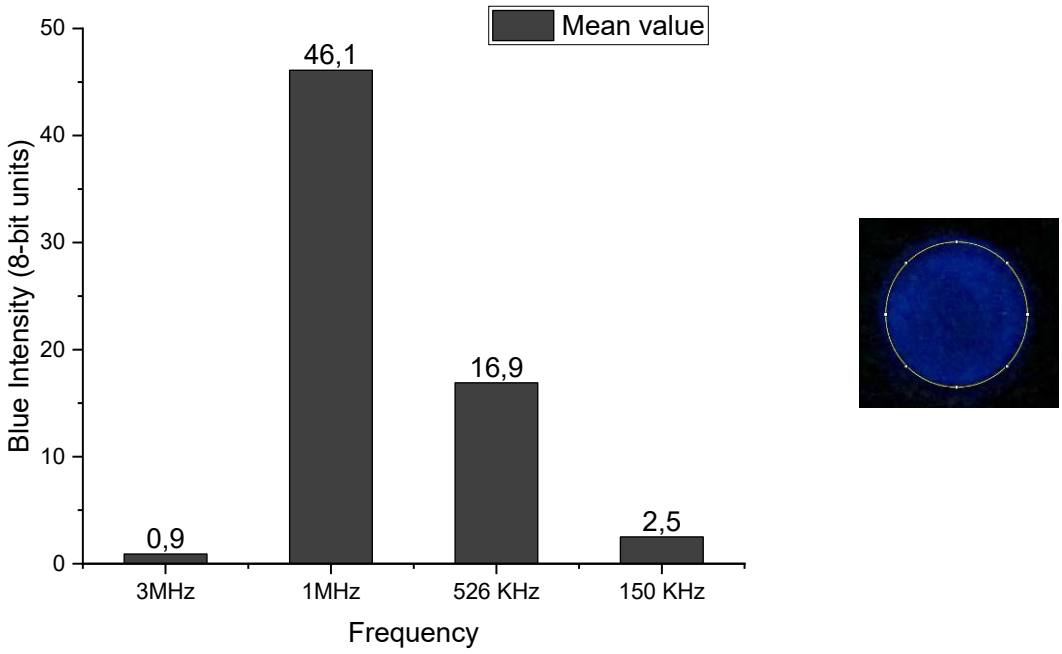

Figure 4.20: Blue intensity mean values of samples with V: 2 mL, different frequencies, cover: Air (left) and ROI selected for the analysis (right).

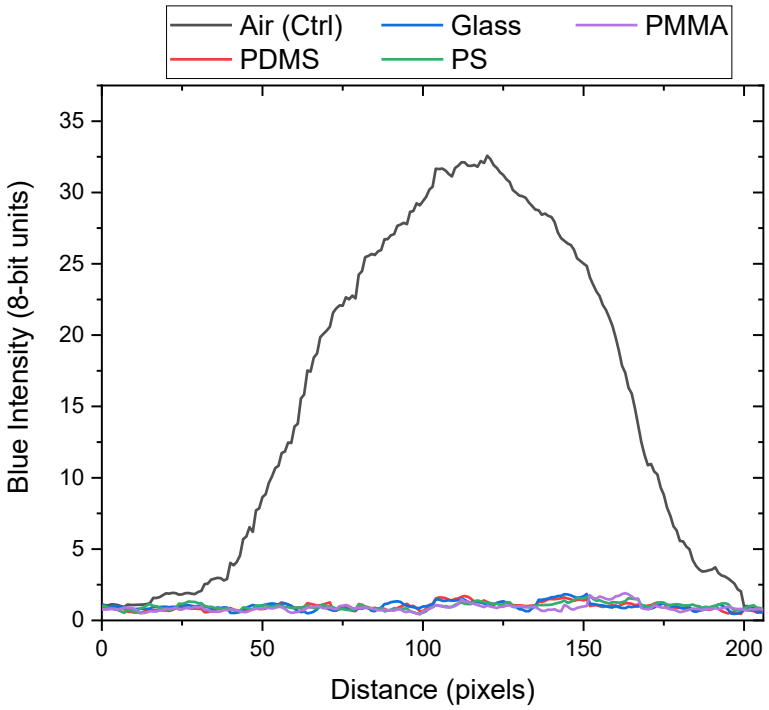

Figure 4.21: Blue intensity profiles of samples with V: 3 mL, f: 526 KHz, different covers.

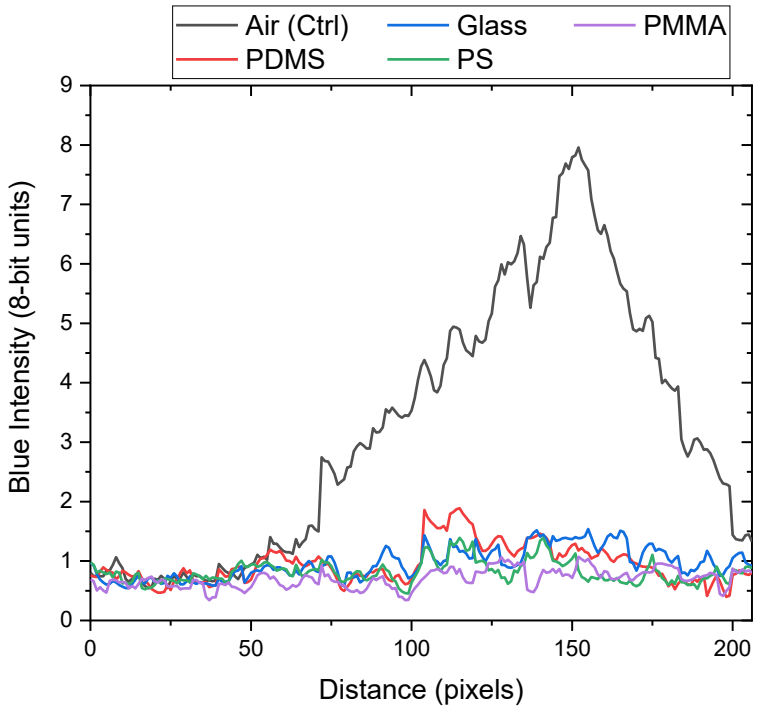

Figure 4.22: Blue intensity profiles of samples with V: 3 mL, f: 150 KHz, different covers.

From the comparison between different frequencies with 2 mL as solution volume (Figure 4.19, Figure 4.20), it is clear that 1 MHz is the frequency with highest performances regarding SCL, while using the highest frequency possible, i.e. 3 MHz, SCL cannot be observed and measured, leading to the worst scenario. In between, 526 KHz shows good SCL levels, and 150 KHz is a bit better than 3 MHz, even if intensity values are too low to detect SCL. It is known that when US frequency decreases, cavitation should increase, and this trend is confirmed going from 3 MHz to 1 MHz, while further decreasing the frequency, the trend is opposed and cavitation seems to decrease. A more detailed study in the range 3 MHz – 150 KHz should be conducted, but it was not possible using this type of transducer in which all the possible working frequencies were tested.

The comparison between different covers using f = 526 KHz (Figure 4.21) and f = 150 KHz (Figure 4.22) confirms their effect of SCL suppression, already observed using 1 MHz as US frequency in the previous section (Figure 4.15, Figure 4.16). The interesting fact is that using 150 KHz, the small SCL effect observed in the control solution without cover is shifted towards the right part of the well (Figure 4.22), even if with very low values. This effect could be related to an anisotropic emission of the transducer at that particular frequency.

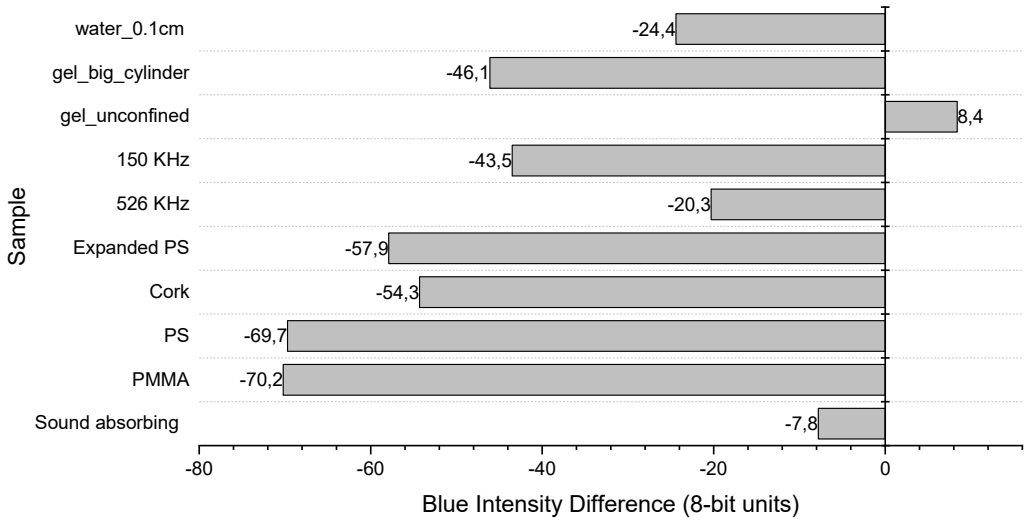

Figure 4.23: Summary of the most important results of this section: blue intensity mean value difference with respect to their reference set-up.

To conclude this section, a summary on the most important results is reported in Figure 4.23. It is clear that the best result was obtained using the gel as spacer, with higher SCL values with respect to the control, while the others spacer were not satisfying. The cover in EPDM shows the best results among the tested covers, defining a possible way to develop future experiments. Regarding the US frequency, 1 MHz remains the best one for obtaining cavitation and subsequent ROS formation.

4.1.4 CELLEX Photopheresis procedural kit – Cartridge

In this first section regarding the CELLEX Photopheresis procedural kit, the SCL was studied in the cartridge, particularly on a portion of the first two channels and the curve connecting them, by comparing the effect of the presence and absence of NPs. The experimental set-up was the following:

- Volume occupied by the solution: 10 mL,
- Sonication and exposure time: 2 min,
- Set – up arrangement: the cartridge was positioned on the inclined plane in order to let the solution fill completely the portion of the two first channels on the transducer and the curve connecting them (Figure 3.2c). The transducer was placed both under the straight part of the channels and under the curve.
- There was no contact of the sonicated part of the solution with air molecules.

Table 4.12: SCL results in the cartridge. Effect of the presence of ZnO NPs.

Solution	Transducer (Piezo) position	Image
Luminol + H_2O_2	Straight part of the channel	
Luminol + H_2O_2 (already sonicated 2 min)	Curve	
Luminol + H_2O_2 + ZnO (already sonicated 4 min)	Straight part of the channel	

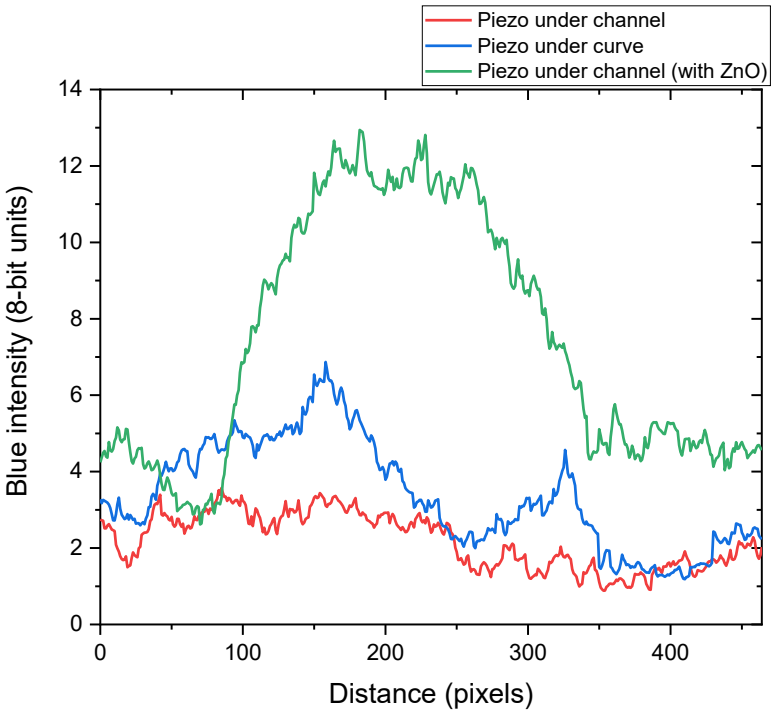

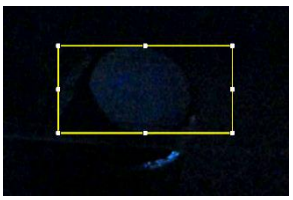

Figure 4.24: Blue intensity profiles of samples reported in Table 4.12 (left) and ROI selected for the analysis (right).

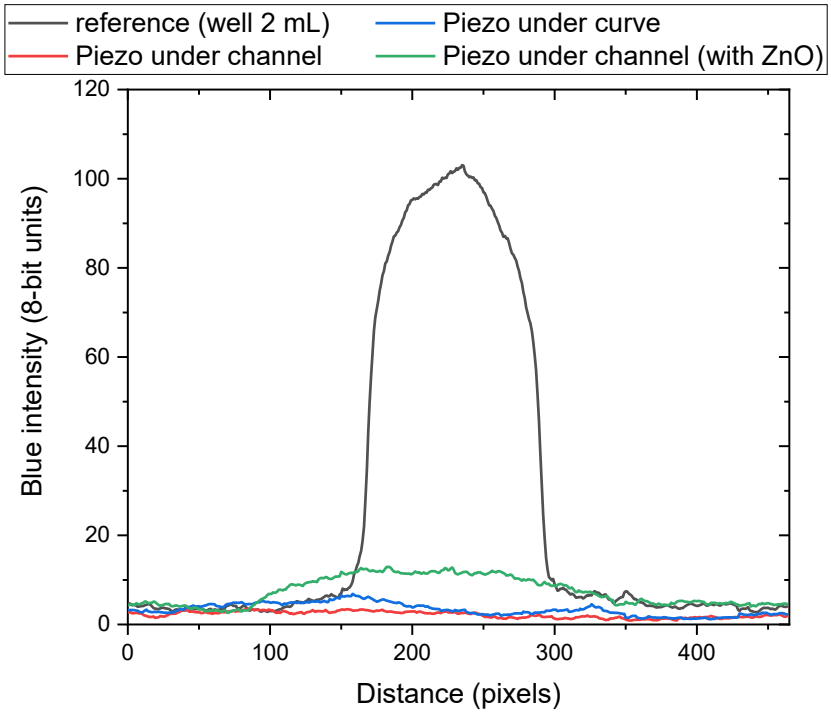

Figure 4.25: Blue intensity profiles of samples reported in Table 4.12 with the addition of a reference sample.

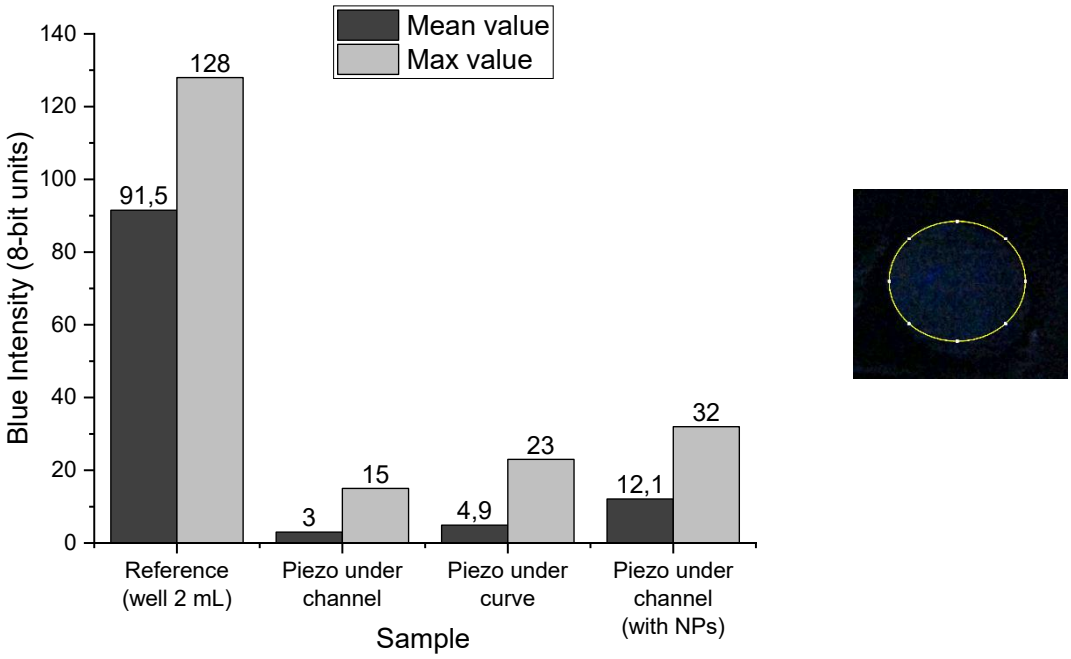

Figure 4.26: Blue intensity statistics of the samples reported in Table 4.12 (left) and ROI selected for the analysis (right).

If we consider only Figure 4.24, the blue intensity profile of the sample with NPs is higher with respect to the profiles of samples without NPs, underlying the effect of ZnO on the production of ROS, even if the values are very low. However, when we compare the last profiles with the reference one (Figure 4.25), it is clear that the intensity values obtained in the cartridge are much more lower than those obtained in the 2-mL-well, as also well depicted from the statistics

(Figure 4.26), where the difference between the reference and the others sample is very high. This difference may be related to many factors that are different in the cartridge: confinement of the fluid between two plates and absence of contact with air molecules, different material and thicknesses of both the plastic of the channel and of the fluid, presence of a bigger system. Moreover, in Figure 4.26 the samples “Piezo under channel” and “Piezo under curve” share similar results, with very small differences, which are probably due to the different position of the transducer with respect to the cartridge and the related different presence of side walls between the middle of the channel and the curve. Finally, it should be considered that the cartridge ruined using 100% of power in the US transducer, probably related to high energy absorbance of the material.

To go further with the tests on the cartridge, SCL was also investigated in different experimental set-up that allow air molecules to be in contact with the sonicated solution in three different ways, in order to estimate their eventual influence on the radicals production. The experimental set-up was the following:

- Sonication and exposure time: 1 min
- Volume occupied by the solution: about 5 mL

Three arrangements were analysed:

1. The transducer was placed under the channel surface and the cartridge was tilted in order to make the solution occupying only a part (about one half) of the channel portion lying on the transducer area (Figure 4.27).

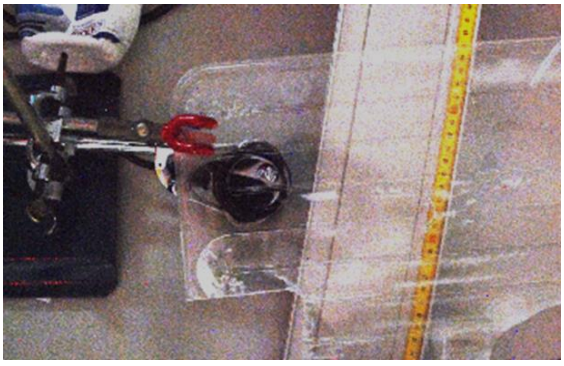

Figure 4.27: First cartridge and transducer arrangement: the Luminol solution occupy only one half of the sonicated channel portion.

2. The transducer was placed under the channel curved edge and the cartridge was tilted in order to make the solution fall to the cartridge edge, in contact with the transducer (Figure 4.28).

Figure 4.28: Second cartridge and transducer arrangement: the Luminol solution occupy the cartridge edge which is sonicated.

3. The transducer was placed under the channel surface and the portion of the cartridge upper plate in correspondence with the transducer area was removed by cutting, in order to obtain an open container with PMMA as bottom material. In this way, the sonicated solution was directly in contact with air during the sonication. Moreover, the solution was held and confined in this portion of the channel by inserting the parafilm around the cut borders of the created experimental area, avoiding solution leaking out (Figure 4.29).

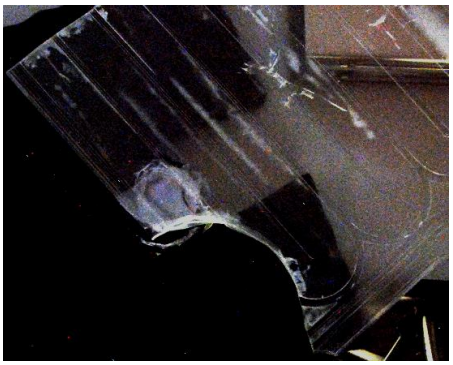

Figure 4.29: Third cartridge and transducer arrangement: the Luminol solution in in the container obtained by the removal of the upper plate of the cartridge, and the transducer is below it.

Table 4.13: SCL in the cartridge: effect of the Luminol solution contact with air molecules.

Experimental set-up	Image	Experimental set-up	Image
Transducer on the channel surface		Open channel	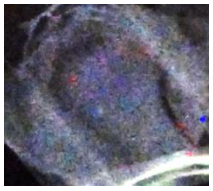
Transducer on the channel edge	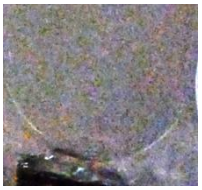	Reference (well 2 mL)	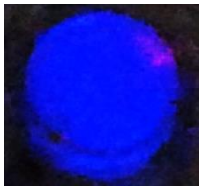

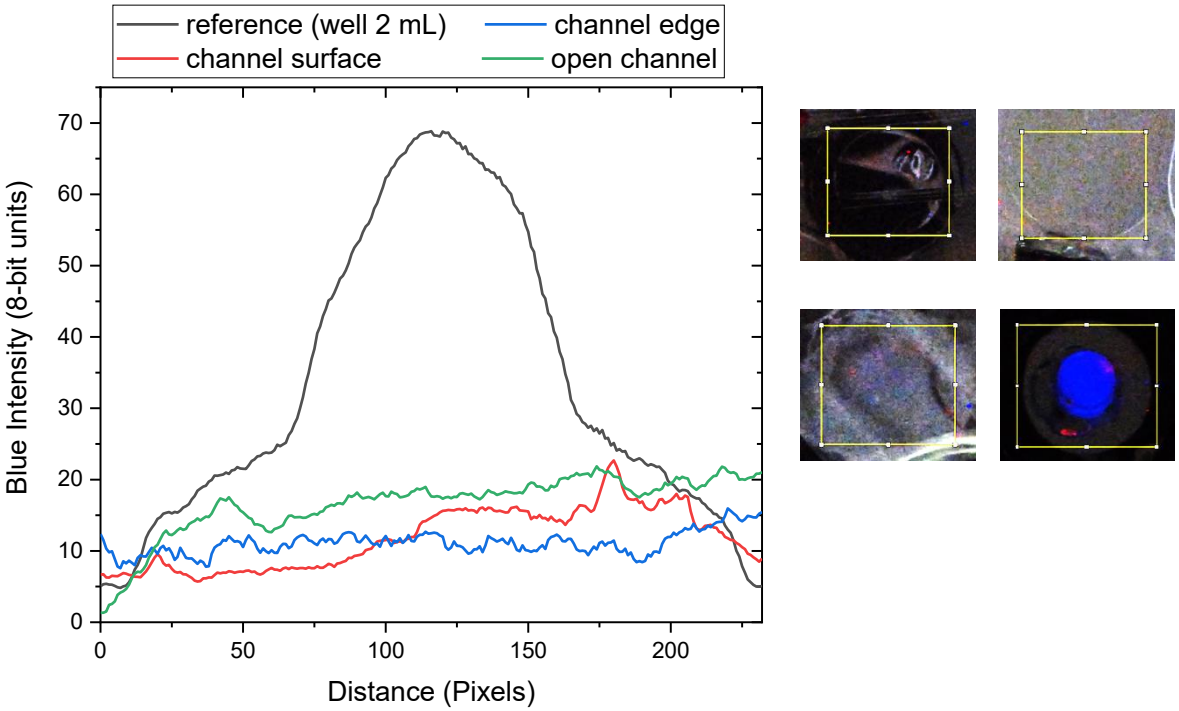

Figure 4.30: Blue intensity profiles of samples reported in Table 4.13 (left) and ROIs selected for the analysis (right).

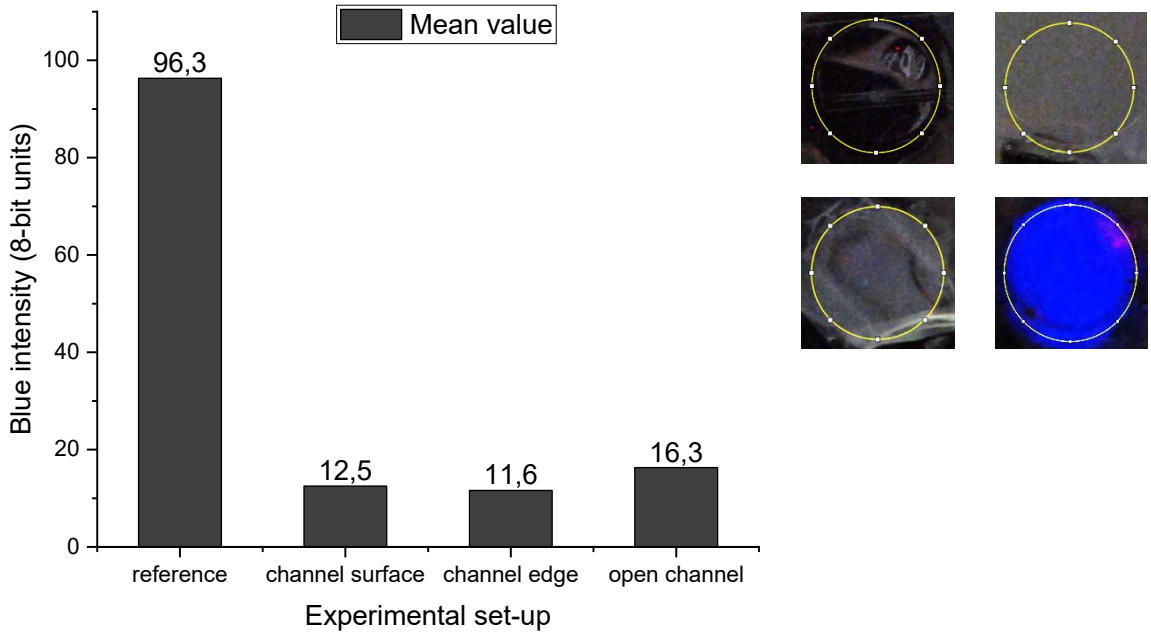

Figure 4.31: Blue intensity mean values of samples reported in Table 4.13 (left) and ROIs selected for the analysis (right).

At first glance, despite the different set-ups allow the solution to be in contact with the air molecules, it can be observed that the SCL reaction inside the cartridge is characterized by extremely low values: it is difficult to recognize blue light points in correspondence to the sonicated region (see images of Table 4.13). Concerning the profiles (Figure 4.30) and the mean value (Figure 4.31), the samples "channel edge" and "open channel" showed higher values due to noise from high luminosity of the environment, that were adjusted by the subtraction of environmental light. One of the possible reasons of the weak detected SCL intensity is the high dispersion and absorption of the US field into the solid part of the set up (i.e. the cartridge and in one case the parafilm), which causes an attenuating effect preventing a strong energy concentration of the field in the solution region. This effect seems to overcome the favourable contact of the solution with air, which on the contrary has given good SCL results in previous experiments.

4.1.5 CELLEX Photopheresis procedural kit – Tubes

In this second section regarding the CELLEX Photopheresis procedural kit, the SCL was studied in the silicon tubes. The experimental wet-up was the following:

- Volume occupied by the solution inside the tubes: about 2 mL in the long tube, about 400 µL in the shortened tube.
- The tubes containing the solution were closed at their ends with parafilm.

- Sonication and exposure times: 2 minutes.
- Four arrangements were analysed with a long portion of the tube and they are reported in Figure 4.32 below.

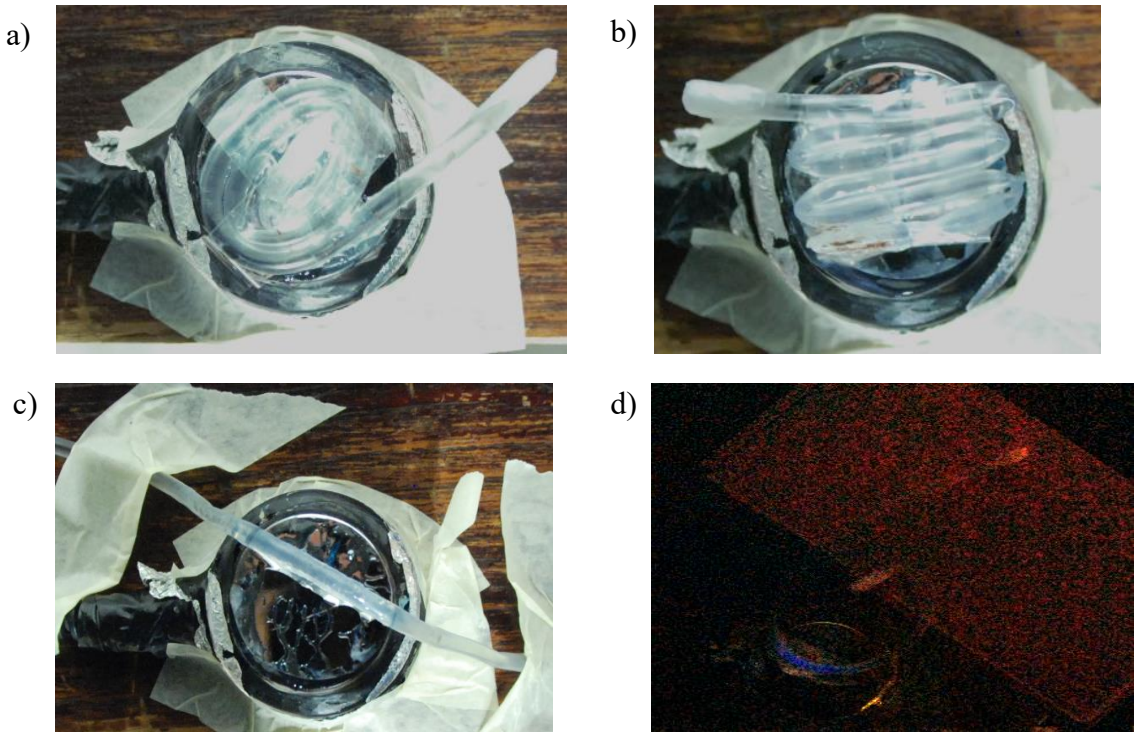

Figure 4.32: a) Spiral shaped tube fixed on transducer with transparent tape. b) Serpentine shaped tube fixed on transducer with transparent tape. c) Single tube leaned on transducer, held it fixed by tape on the transducer plane. d) Single tube leaned on transducer, with external support on the transducer plane to hold it fixed.

- A cut (shortened) portion of the tube was analysed both in contact and using different spacers from the transducer (Figure 4.33 below).

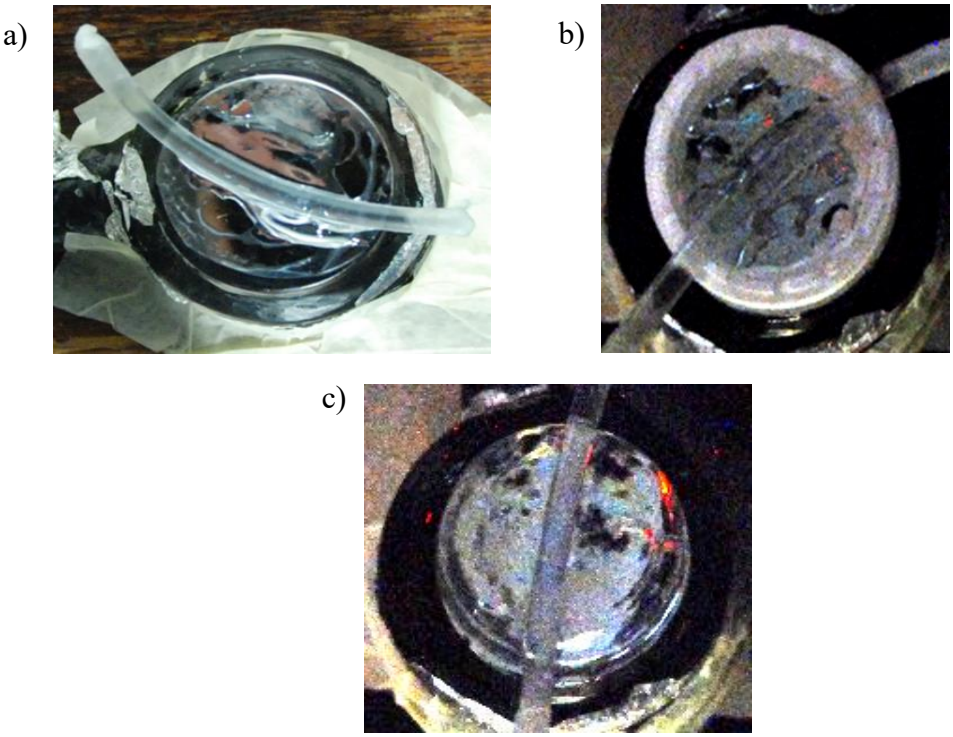

Figure 4.33: a) Contact with the transducer. b) Thick gel layer confined by a plastic cylinder. c) Thick gel layer alone (not confined).

Table 4.14: SCL results in the long portion of the tube and in the reference well.

Experimental set-up	Image	Experimental set-up	Image
Spiral shaped tube		Single tube (fixed with tape)	
Spiral shaped tube (solution already sonicated 2 minutes)		Single tube (fixed with external support)	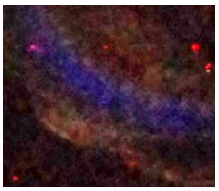
Serpentine shaped tube		Well 2 mL (reference)	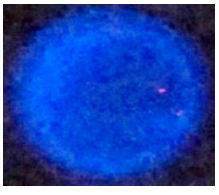

Table 4.15: SCL results in the shortened portion of the tube.

Separation from transducer	Image
Contact	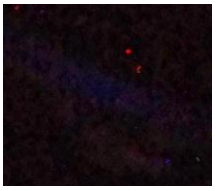
Thick gel layer confined by plastic cylinder (~1cm)	
Thick gel layer unconfined (~1cm)	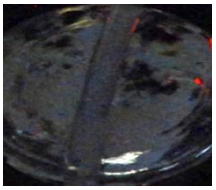

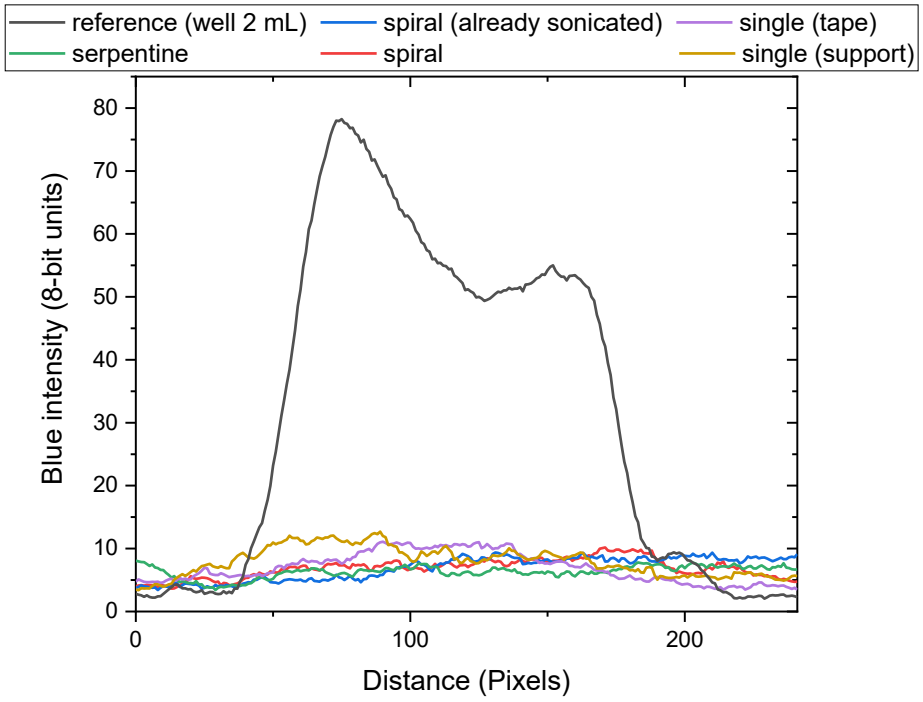

Figure 4.34: Blue intensity profiles of samples in the long portion of the tube, relative to Table 4.14.

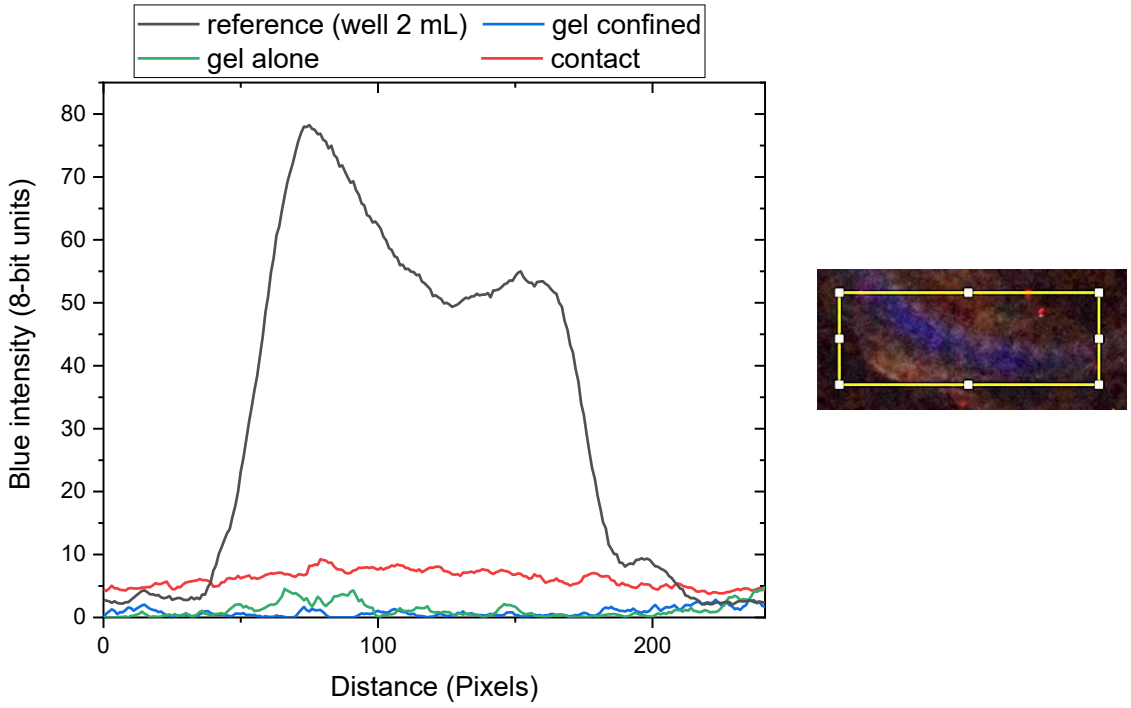

Figure 4.35: Blue intensity profiles of samples in the shortened portion of the tube, relative to Table 4.15 (left). ROI selected for the analysis (right).

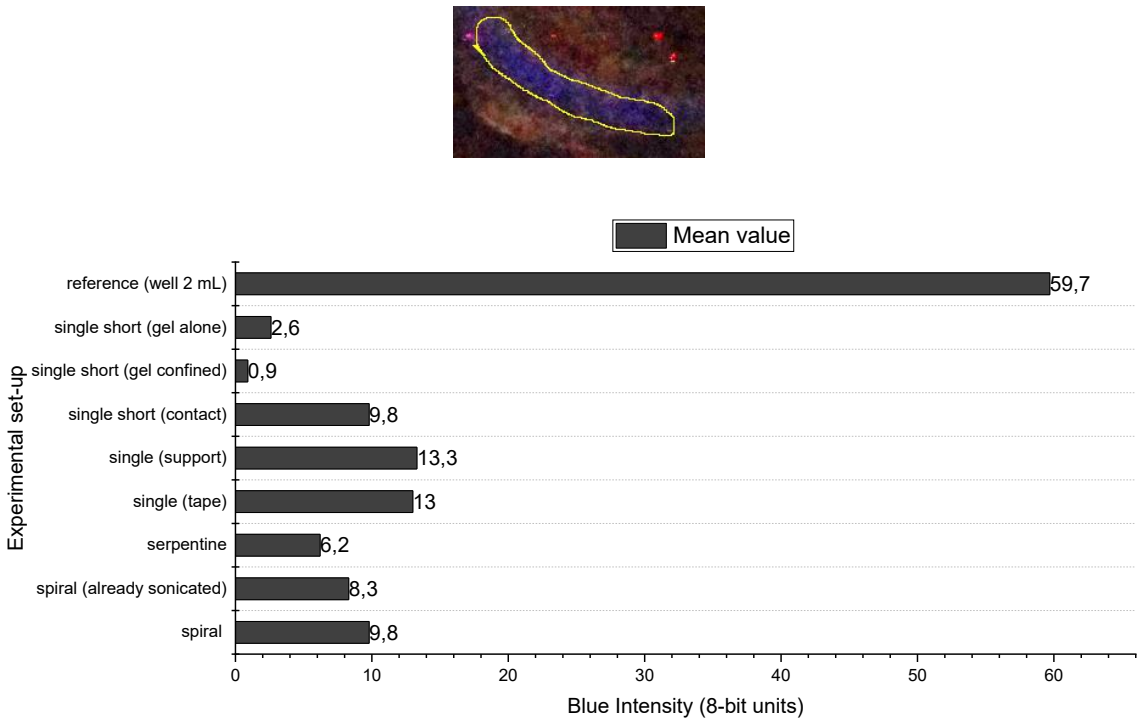

Figure 4.36: Blue intensity mean values of samples in the tube (bottom) and ROI selected for the analysis (top).

First of all, it can be clearly affirmed that the detected blue light intensity produced by the SCL reaction inside the tubes is much lower than the one produced by the reference well (Figure

4.36). This result was expected because previous experiments have revealed that when the solution is covered by a soft material, whose acoustic impedance value is close to the water's one, as in this case for silicone, the radicals production by the sound wave is highly reduced with respect to the contact with air. Among all the tested set-ups, the intensity plots (Figure 4.34, Figure 4.35 and Figure 4.36) show that the best results are obtained when the tube is placed on the transducer without creating any particular shape. This is related to the fact that the bottom surface of a single tube can be better coupled with the transducer by the gel, whereas more complex shapes are more difficult to be held in position and this can allow air to pass between the tubes and the gel, decreasing the coupling. Then, as it was expected, Figure 4.35 shows that the SCL intensity assumes lower values when the tube is separated from the transducer by the confined gel, again related to the energy dispersion of the US field. Finally, from the mean intensity values (Figure 4.36), it can be seen that the separation of the tube from the transducer with a thicker gel layer does not give better result with respect to the case in direct contact. This can be associated to the damping of the US field as it proceeds along the gel layer, reaching the solution with a reduced energy.

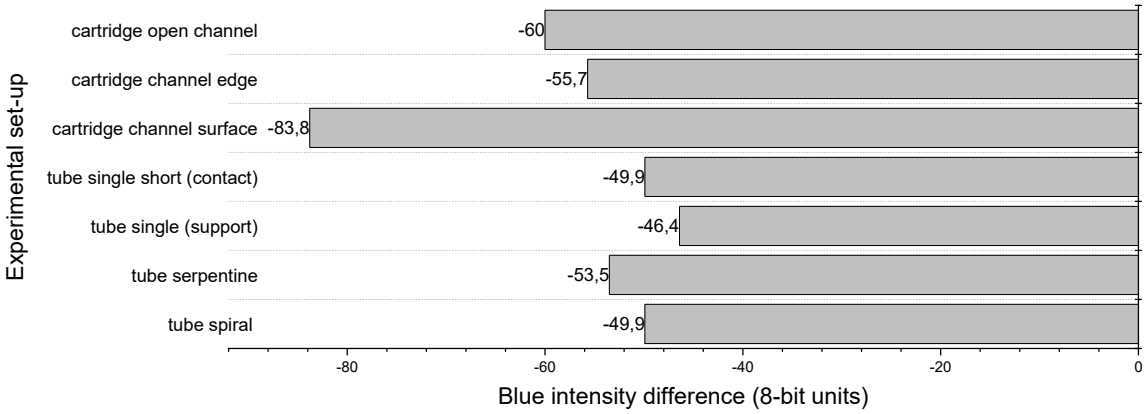

Figure 4.37: Summary of the most important results of this section: blue intensity mean value difference with respect to their reference set-up.

To conclude the sections about the CELLEX Photopheresis kit, a summary of the most important results is reported in Figure 4.37. It is clear that neither the cartridge nor the tubes revealed to be useful for our purposes of obtaining ROS formation in a channel environment already present on the market. However, these results were also important to understand which materials and shape need to be avoided in the development of a future cartridge.

4.2 Electron Paramagnetic Resonance experiments

In this section, the EPR results about the most interesting set-ups previously tested using SCL (i.e. the single well and the cartridge) are reported.

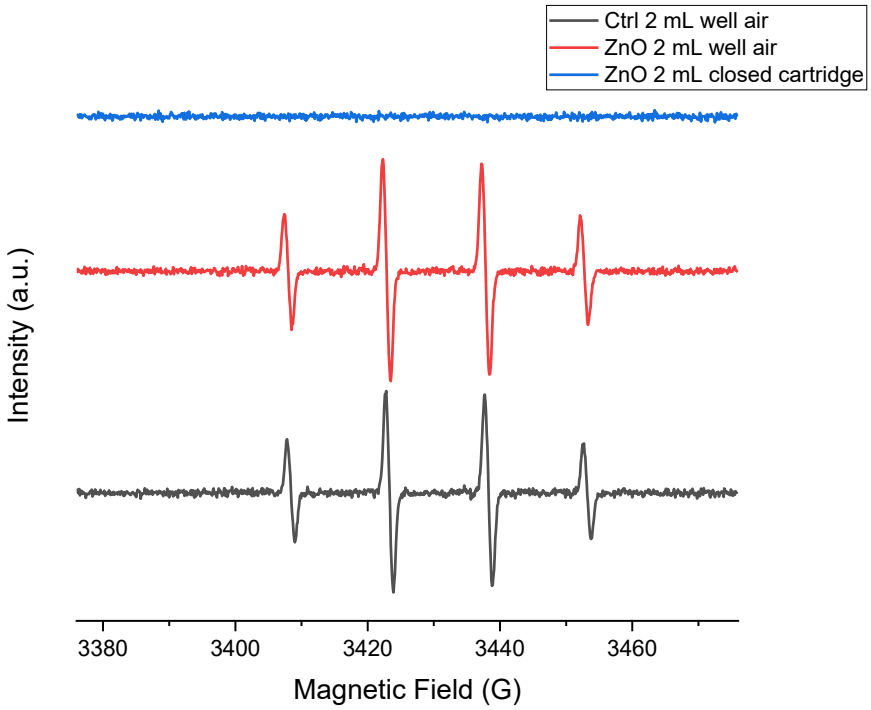

Figure 4.38: DMPO-OH absorption spectra for the samples containing V = 2mL.

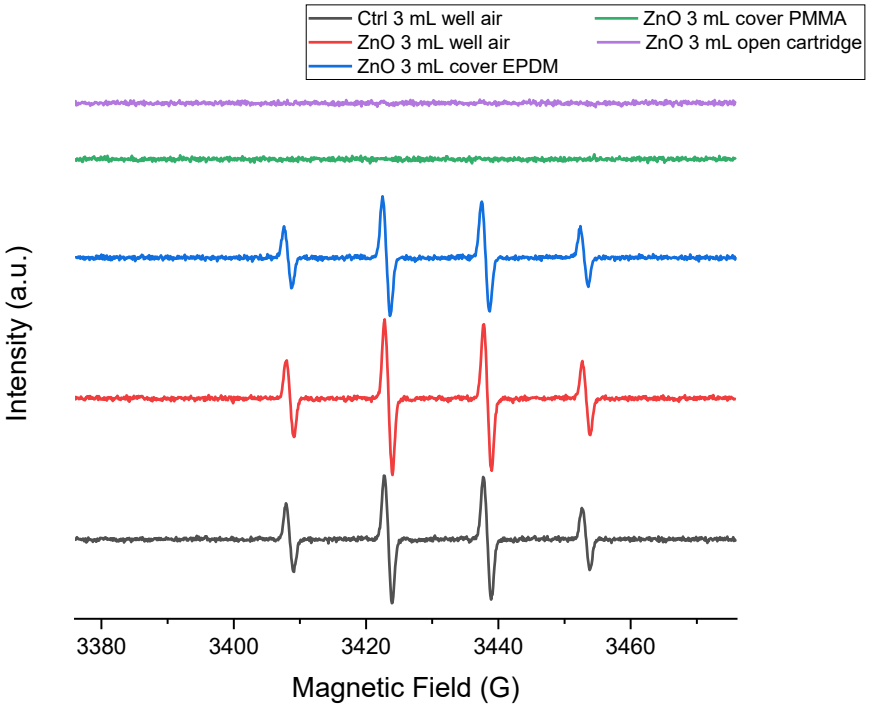

Figure 4.39: DMPO-OH absorption spectra for samples containing V = 3mL.

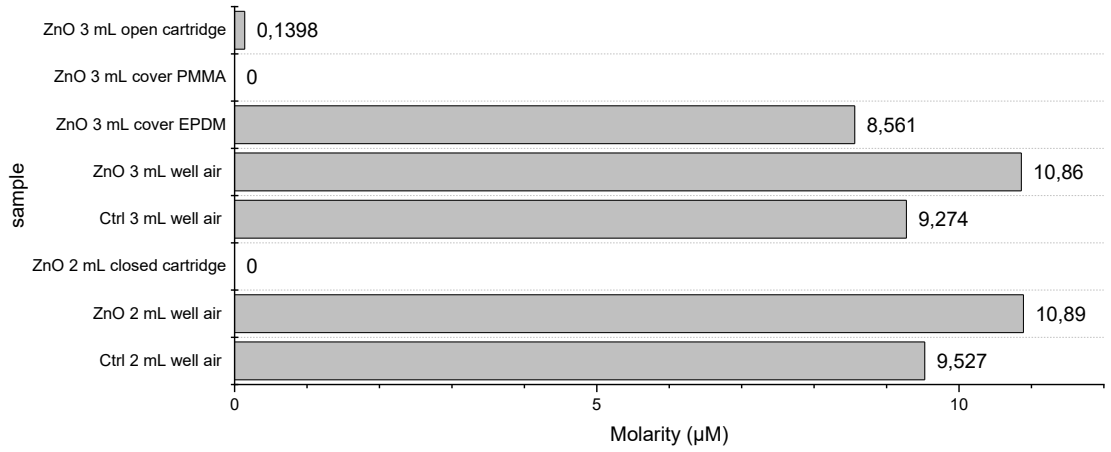

Figure 4.40: Molarity of the OH· radicals present in every sample, measured by the Spin Count of the EPR software.

The obtained absorption spectra (Figure 4.38 and Figure 4.39) are typical of the DMPO-OH construct since they contain 4 different peaks. From Figure 4.38, it is clear that the spectrum obtained in the "closed cartridge" is related to a very low presence of radicals with respect to the other two samples in the well. In fact, the instrument cannot measure the molarity of the radicals in this sample (Figure 4.40, "closed cartridge"). While for the "open cartridge" sample, the spectrum does not show the typical 4-peaks form (Figure 4.39), even though a very low concentration of radicals is detected (Figure 4.40). This last result, anyway, is very low with respect to the control condition in the well that show very good spectra (Figure 4.39) and high amount of radicals (Figure 4.40). It should be considered that the "open cartridge" sample required a bigger volume with respect to the "closed cartridge", in order to be sure that the solution formed a uniform layer that cover all the sonicated part and not only a portion of it.

Considering the effect of the covers on the EPR results, it can be seen that the presence of a cover in EPDM decreases the radical molarity with respect to the control sample, even if it remains quite high. This is different from a cover in PMMA that completely suppress the production of ROS (Figure 4.39 and Figure 4.40). Both these results are in line with the previous results obtained by SCL experiments

Finally, from these results, the effect of ZnO on the production of ROS in a single well can also be extrapolated. In details, the presence of ZnO helps in the radical production, leading to a high molarity (Figure 4.40), and moreover this effect can be observed using both solution volumes, i.e. 2 mL and 3 mL. It should be noticed that the concentration of the spin trap (DMPO) is the same in every sample, for this reason there are no high differences between the results obtained for samples with 2 mL and 3 mL.

As a conclusion, the results in the cartridge and in the well follow the ones obtained using the SCL technique, even though the EPR technique permits to have also quantitative data, which can be useful for a deeper analysis on the effect of these ROS concentration on circulating tumour and healthy cells.

4.3 Temperature measurements

In this section, the results obtained by the temperature measurements are collected and shown.

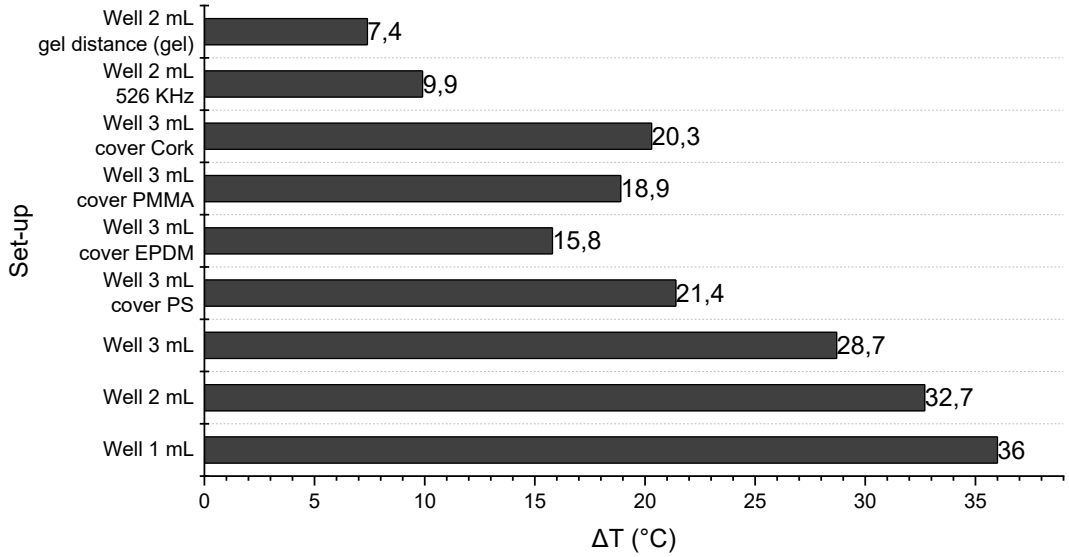

Figure 4.41: Temperature increase measured after the application of US for 1 min on every sample.

First of all, the reference samples (Figure 4.41, well 1, 2, 3 mL) show the highest T increase, with decreasing values by increasing the volume, probably related to higher heat dispersion. The presence of covers reduces the T increase (Figure 4.41, well 3 mL with different covers), due to the lower US energy reaching the solution, also observed and analysed in the previously SCL and EPR experiments. The US frequency has also an impact on the T increase, because at f = 526 KHz the temperature only increases 10 °C. Finally, due to the aqueous composition of the gel, the latter also shows a 7 °C heating when it is used for the distancing from the transducer. This result should be take into account when considering that the best results of SCL were observed when the single well was placed at 1-cm distance using a thick gel layer (Figure 4.23).

In general, the temperature increase associated to the delivery of 100% of the US power is quite high if we consider a further possible application to living cells. This was expected because the SCL studies were performed as a first screening on different set-ups, with the purpose of choosing the best options to pursue in the future of the project.

4.4 Numerical Simulations: Single well

In this section, the results about the numerical simulations in the well environment are shown and discussed. In order to better understand the following plots, in Figure 4.42 below it is shown the domain used in the simulations with the axis orientation. The origin of the axis is placed in the centre of the well's bottom side and the H value (along z axis) of this particular picture is 0.015 m.

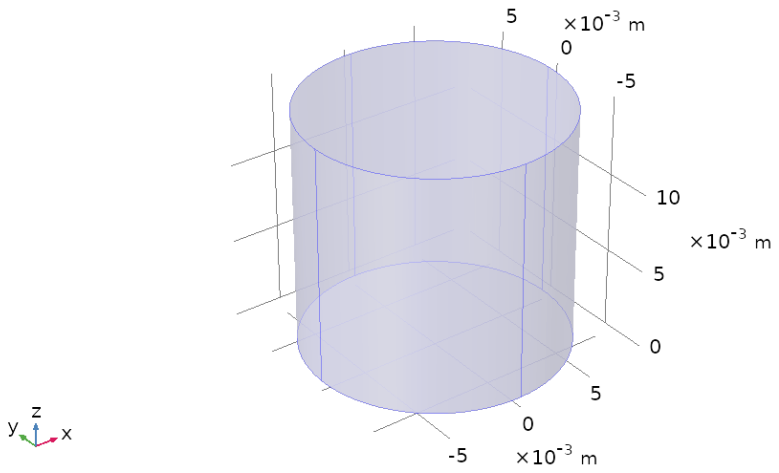

Figure 4.42: Domain used for the simulations: it represents the well filled with 3 mL of volume, corresponding to H = 0.015 m.

Additionally, the figures showing the acoustic field and the intensity magnitude distribution are coloured images, where the colours are linked to a range of the numerical values in the plots, which is shown at the beginning of every Figure.

4.4.1 Influence of the liquid height

The next images represent the acoustic field distribution inside the well with three different volumes, corresponding to three different liquid heights (0.005, 0.01, 0.015 m). In these simulations, the water is always considered in contact with air molecules, represented by the air acoustic impedance boundary condition on the top side of the domain.

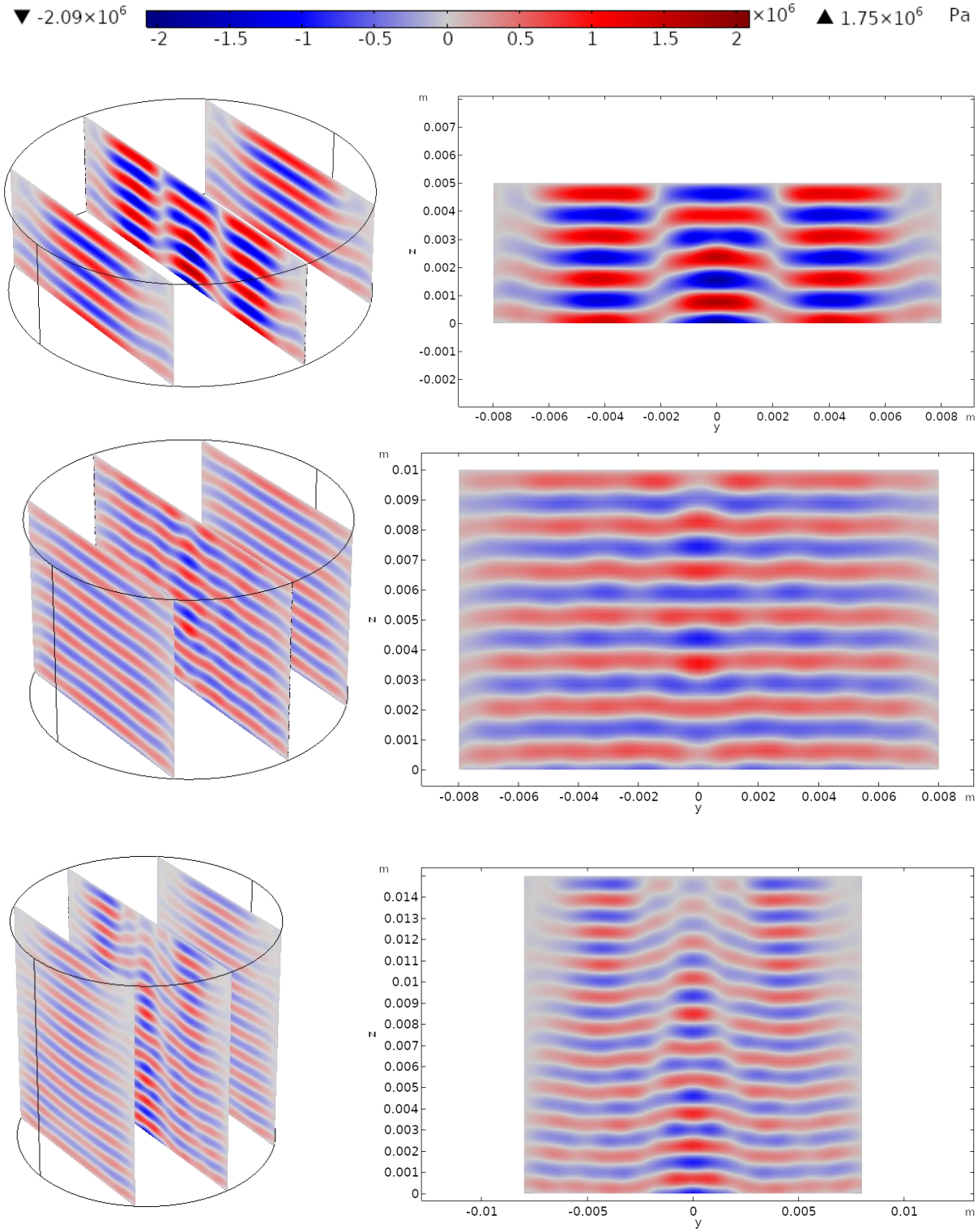

Figure 4.43: Total acoustic pressure field (Pa) in the three different liquid heights: H = 0.005 m (first line), H = 0.01 m (second line), H = 0.015 m (third line). In every line, the first plot on the left represents the acoustic field on three parallel yz-planes and the second plot on the right represents the acoustic field on the central yz-plane.

The US field distribution on the vertical yz-plane (Figure 4.43) shows the propagation of a sound wave, characterized by positive pressure values (red) alternating with negative pressure values (blue). It is clear that the wave shape is influenced by the liquid height: at the lowest

height value (H = 0.005 m) the central part of the well shows a distortion in the wave propagation (Figure 4.43, first line). This distortion is less evident when H is 0.01 m (Figure 4.43, second line), while is again visible at H = 0.015 m (Figure 4.43, third line). From the images that show the three parallel planes (Figure 4.43, left), it can be observed that the distortion of the wave is not visible anymore going towards the lateral side of the domain, so that only the central volume of the well is characterized by it. This result could explain the slight higher SCL intensity observed in the lateral parts of the well (Table 4.5). Moreover, the higher the liquid height, the lower the pressure values, as it can be appreciated by the decrease in colour intensity: at H = 5 mm the highest value reached is 1.75 MPa, while at H = 15 mm the highest value is 0.9 MPa. Furthermore, the pressure decrease is also visible approaching the lateral walls of the well, where the distinction between positive and negative pressure is less pronounced, probably due to the hard material composition of the well and the related damping.

Finally, it can be considered that the overall pressure values obtained in the simulated well environment are in the order of MPa units. According to Apfel et al. (Apfel, 1991), the cavitation threshold in water sonicated at 1 MHz is approximately 0.3 MPa, a value reached and exceeded in all the liquid heights simulated. This result confirms the obtained SCL and the EPR results using 2 mL and 3 mL of solution (corresponding to liquid height of 10 mm and 15 mm in the examined well, respectively); while for 1 mL (corresponding to the liquid height of 5 mm in the examined well), SCL was not observed. However, since the simulation results show that the pressure value exceeded that of cavitation threshold: it can be concluded that the problem was probably the too low amount of Luminol present, but not the cavitation threshold reached.

The next images represent the intensity magnitude distribution inside the well with three different volumes, corresponding to three different liquid heights (0.005, 0.01, 0.015 m).

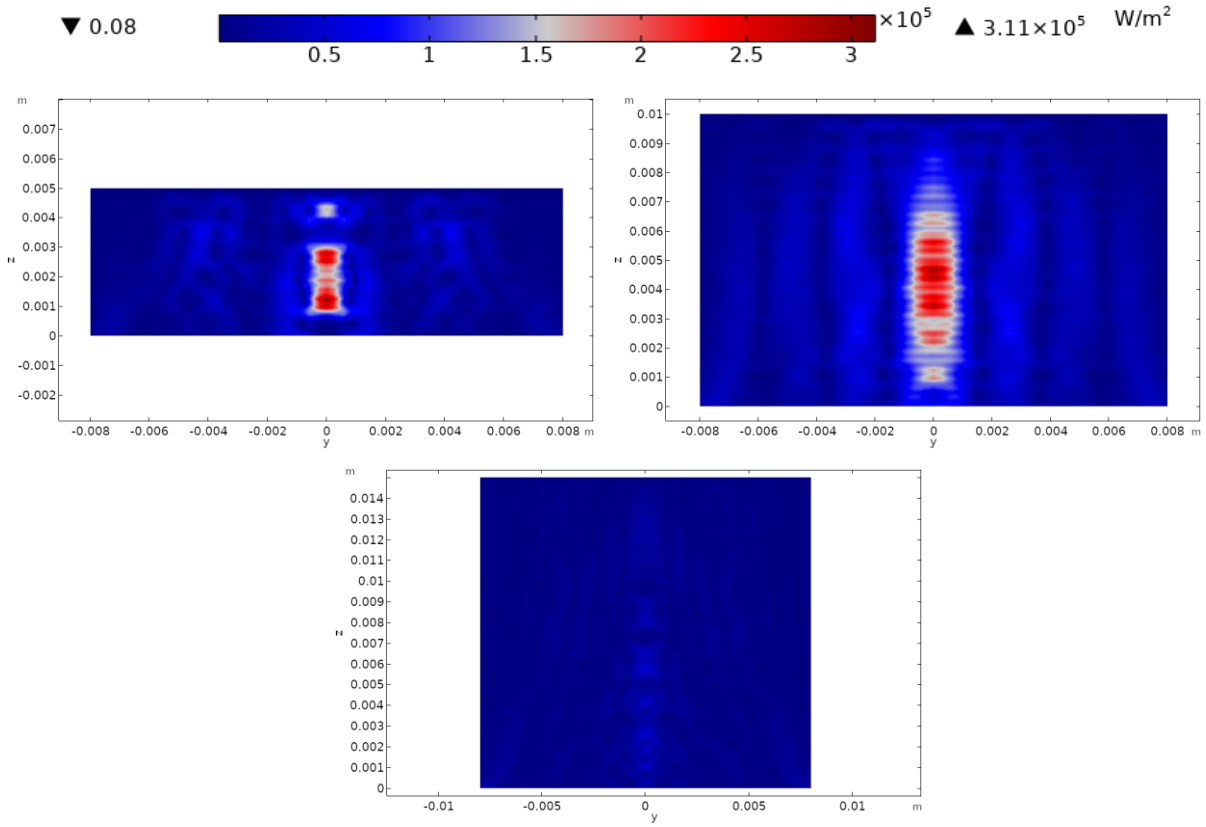

Figure 4.44: Intensity magnitude (W/m2) on the central yz-plane for the three different liquid heights: H = 0.005 m (top left), H = 0.01 m (top right), H = 0.015 m (bottom).

The intensity magnitude distribution on the vertical yz-plane (Figure 4.44) shows a concentration of the intensity in the central part of the domain, probably related to the cylindrical shape of the well and the reflection coming from the lateral walls. The high values obtained in the first two liquid heights (Figure 4.44, top), in the order of magnitude $3 \cdot 10^5$ W/m^2, result to be higher with respect to the input value coming from the transducer (~ $3 \cdot 10^4$ W/m^2). This could be related to the reflection of the energy from both the lateral walls and the air on the top, which permits to reach very high values in a small central volume. On the other hand, the third simulated liquid height (Figure 4.44, bottom) shows a more homogenous distribution of the intensity, whose values are lower with respect to the first two, even if a slightly concentration of higher values could be detected in the centre (light blue area).

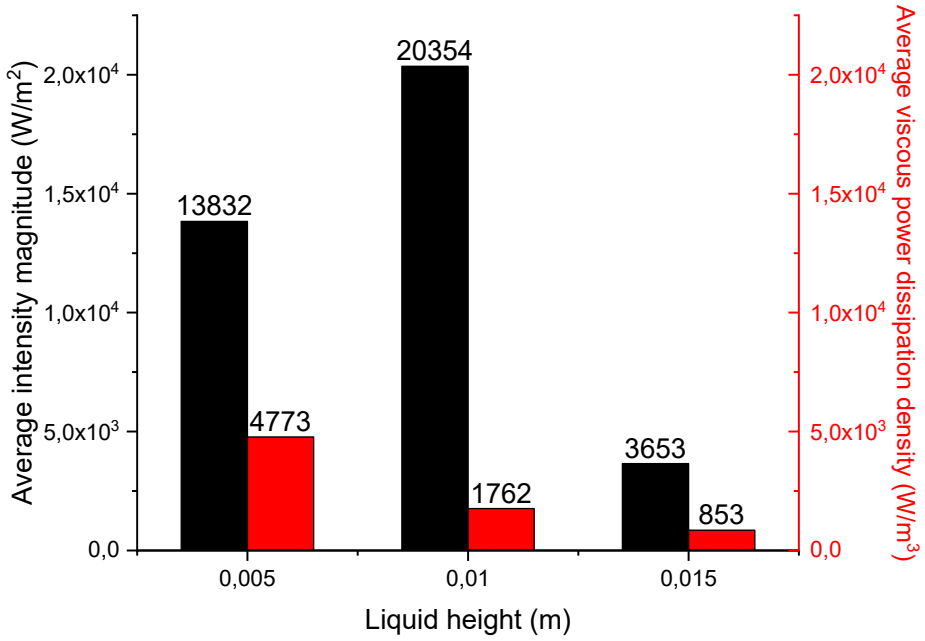

Figure 4.45: Average intensity magnitude (black columns) and power dissipation density (red columns) for the three liquid heights simulated.

The plot above (Figure 4.45) permits to make an additional comparison between the simulated liquid heights. Regarding the average intensity magnitude (Figure 4.45, black columns), the highest value is reached using H = 0.01 m, while the lowest one is represented by H = 0.015 m, as it was expected after the results evidenced in Figure 4.44. All these values are lower with respect to the input intensity coming from the transducer (~ $3 \cdot 10^4$ W/m^2), due to energy dissipation for the presence of a viscous liquid (water in this case). However, thermal dissipations cannot be considered due to the adiabatic assumption of the model, and only viscous dissipations can be studied. It is precisely this parameter that is shown by the red columns in Figure 4.45, namely the average viscous power dissipation density. The highest dissipation value is reached by the lowest liquid height, while increasing the H value, the dissipation decreases. Considering both these parameters, it is interesting to compare them with the results coming from SCL experiments in a single well, where it was almost impossible to detect SCL using an H value of 0.005 m (corresponding to 1 mL). This could be related to both this high power dissipation and the amount of Luminol present in such volume, which was too low to produce SCL. Additionally, the big difference between the intensity magnitude and the power dissipation density in the 0.01m – liquid height could be the key of the very good results obtained by this solution volume in the previous SCL and EPR experiments.

4.4.2 Influence of the cover

The next images represent the acoustic field distribution inside the well with a volume equal to 3 mL (H = 0.015 m) and where the free surface of water is in contact with different materials, simulated by different acoustic impedance boundary conditions. The comparison is divided between air, EPDM and cork (Figure 4.46) and air, PS and glass (Figure 4.47), in the latter a different range of pressure values is used.

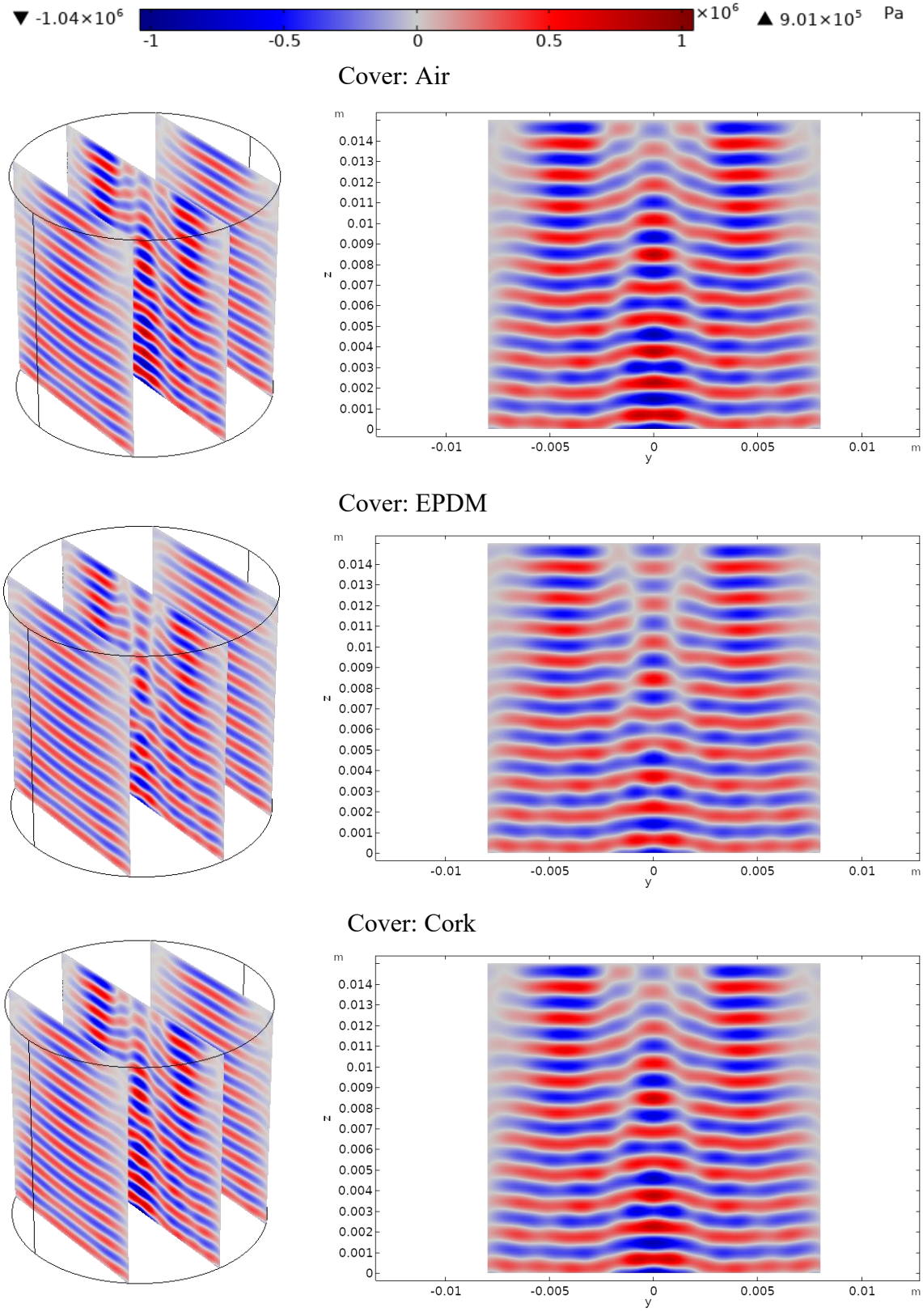

Figure 4.46: Total acoustic pressure field (Pa) in the well covered by: Air (first line), EPDM (second line), cork (third line). In every line, the first plot on the left represents the acoustic field on three parallel yz-planes and the second plot on the right represents the acoustic field on the central yz-plane.

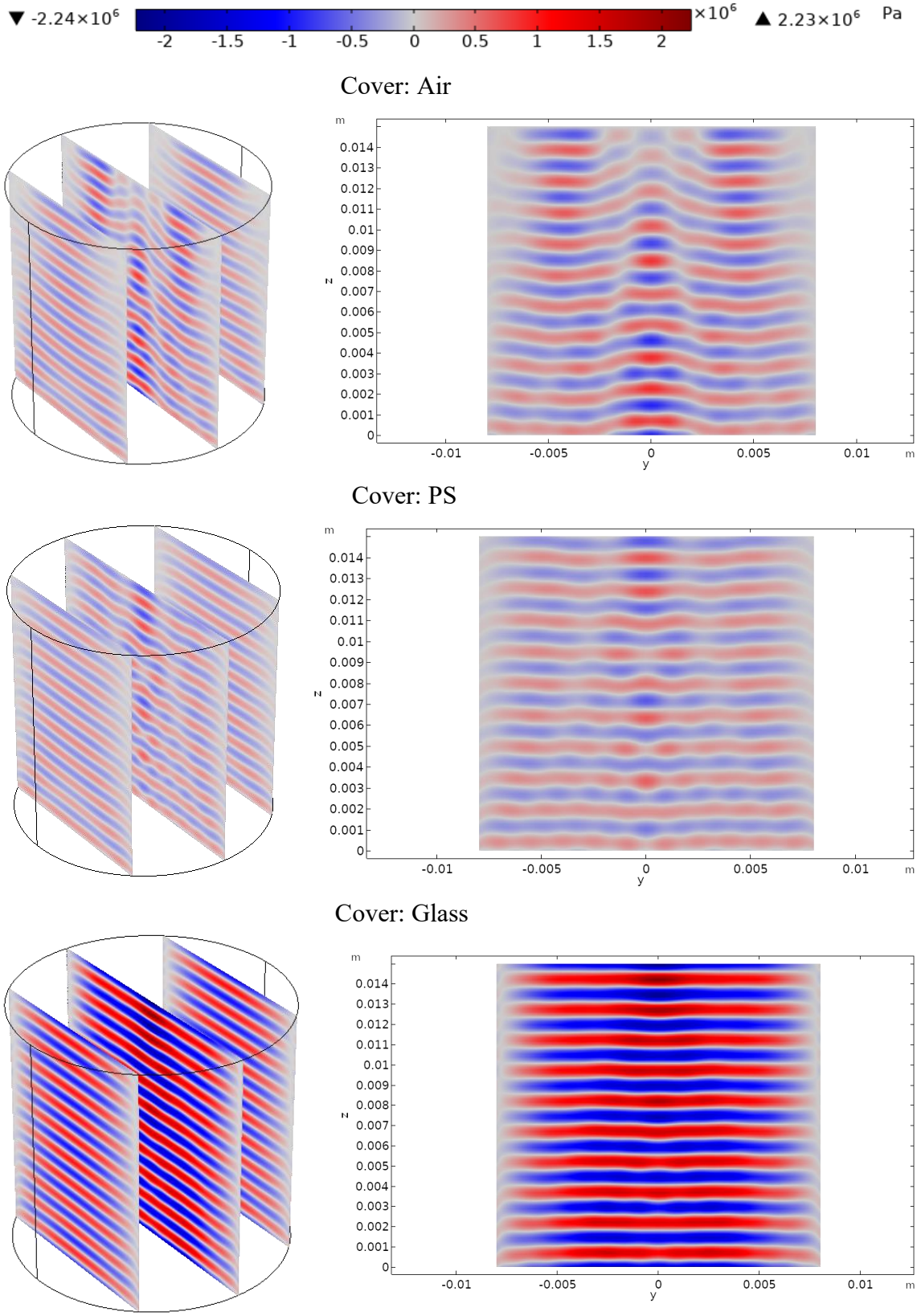

Figure 4.47: Total acoustic pressure field (Pa) in the well covered by: Air (first line), PS (second line), glass (third line). In every line, the first plot on the left represents the acoustic field on three parallel yz-planes and the second plot on the right represents the acoustic field on the central yz-plane.

From Figure 4.46 it is clear that the acoustic field distribution is similar for samples with covers that mimic the air acoustic impedance (EPDM, cork). Particularly, the US wave is characterized by a central distortion with respect to a perfect wave propagation: this is probably due to the reflection at the water-cover interface, characterized by a negative reflection coefficient (see Table 4.8, Air, EPDM, cork). It seems that this type of reflection is related to a change in the phase of the wave, detectable in the central part of the domain.

On the other hand, Figure 4.47 shows that materials like PS and glass, characterized by a higher acoustic impedance with respect to water (see Table 4.8, PS, glass), do not show a central distortion of the wave propagation like in the previous case. PS cover produces pressure values similar to those of air cover, while the glass produces very high pressure values and very good wave propagation. These results are in line with the positive reflection coefficients at the water-cover interface for PS and glass: for PS the R coefficient is lower (R = 0.2) with respect to the glass (R = 0.8), in fact the pressure values produced in the solution are lower too.

Finally, for all the covers simulated, the cavitation threshold of 0.3 MPa (Apfel, 1991) seems to be exceeded, even if cavitation was observed only for covers in EPDM and cork. This result underlines the importance of studying others parameters that take part in the acoustic cavitation and subsequent ROS formation, that were not evaluated so far.

The next images represent the intensity magnitude distribution inside the well with a volume equal to 3 mL (H = 0.015 m).

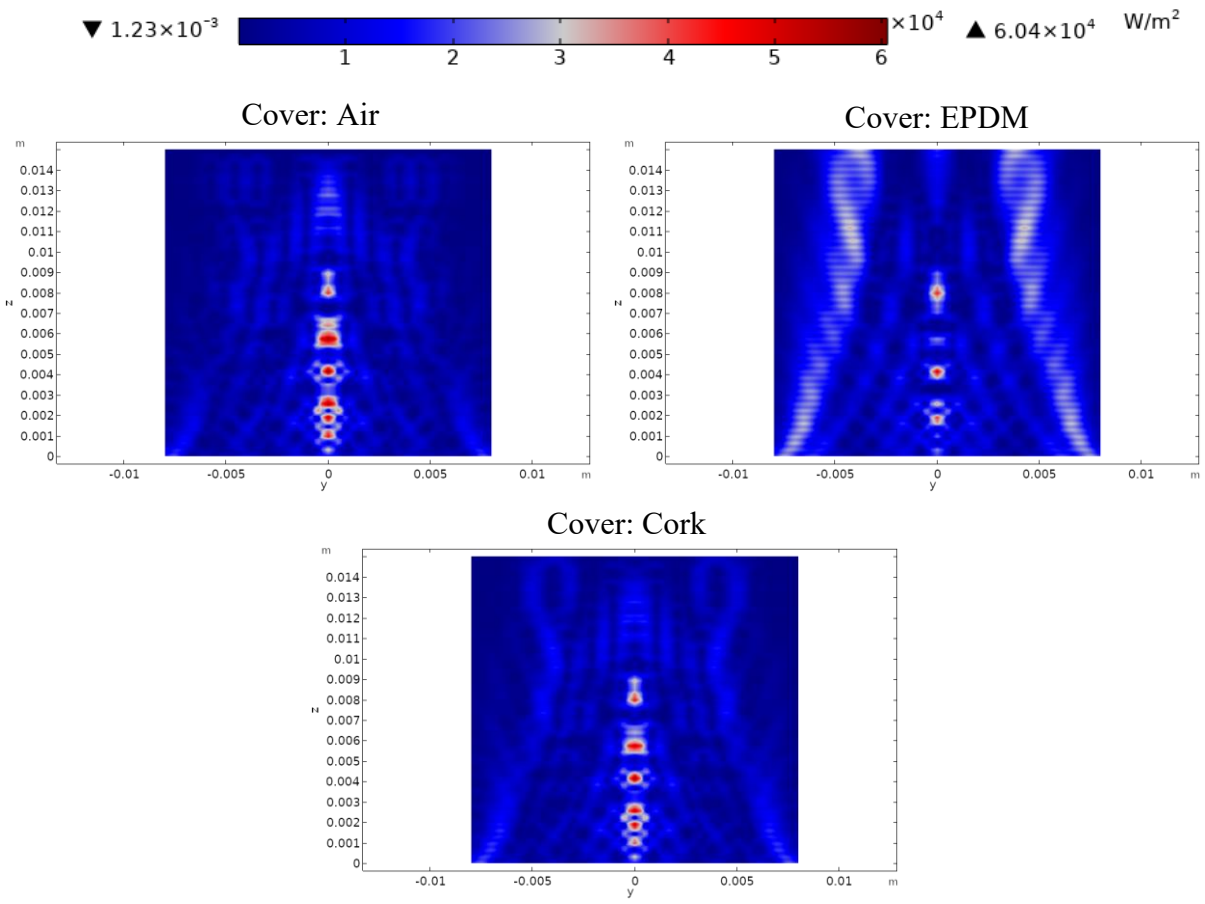

Figure 4.48: Intensity magnitude (W/m²) on the central yz-plane for the three different covers: air (top left), EPDM (top right), cork (bottom).

For the comparison between air, PS and glass, a wider range of intensity values is used, in order to better appreciate the differences between these covers. For this reason, the reference cover (Air) in Figure 4.49 shows differences in colours with respect to the same reference previously exposed in Figure 4.48.

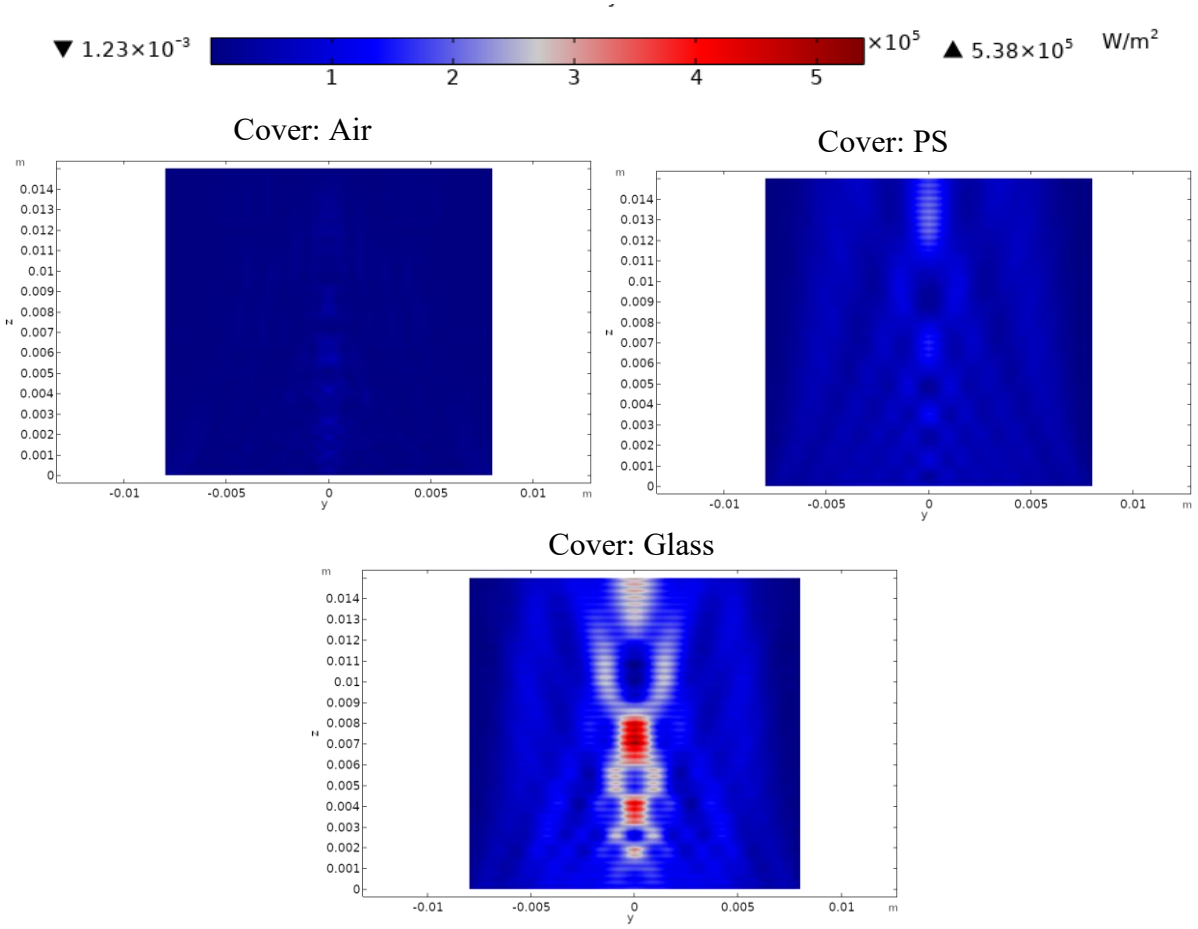

Figure 4.49: Intensity magnitude (W/m²) on the central yz-plane for the three different covers: air (top left), PS (top right), glass (bottom).

Like in the previous investigation of the intensity distribution (Figure 4.44), from both Figure 4.48 and Figure 4.49 it is clear the high intensity concentration in the central part of the domain. Moreover, Figure 4.48 permits to see a similar pattern of intensity for covers that mimic the air acoustic impedance, even if with differences in the values. In contrast, Figure 4.49 shows both the similarity in pattern and the highest intensity values reached by covers in PS and glass.

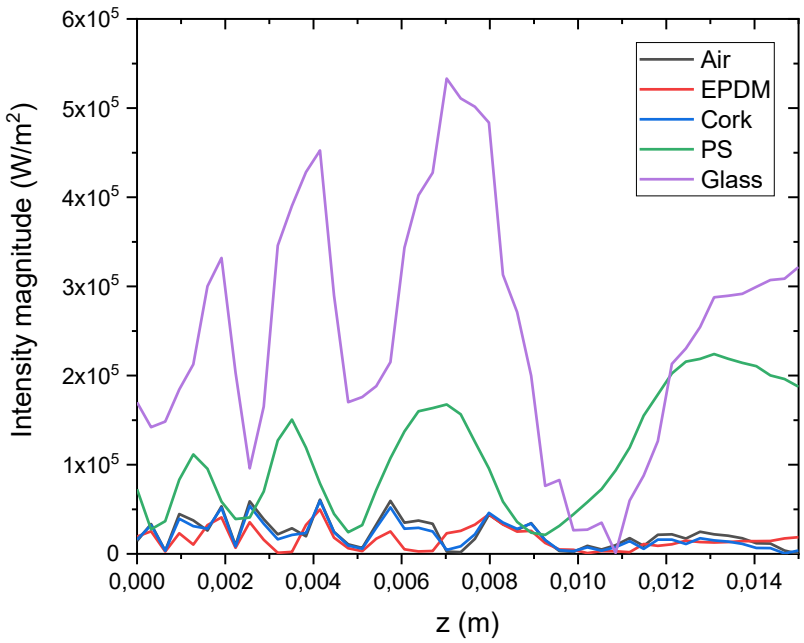

Figure 4.50: Intensity magnitude (W/m²) trend on the vertical line (along z axis) at the centre of the well for all the different covers simulated.

The mentioned similarities in the intensity pattern are also detectable from Figure 4.50 above, which shows the trend in the intensity magnitude on the vertical line (along z axis) in the centre of the domain. PS and glass show a similar pattern with higher values with respect to air, EPDM and cork, which show lower values with another pattern.

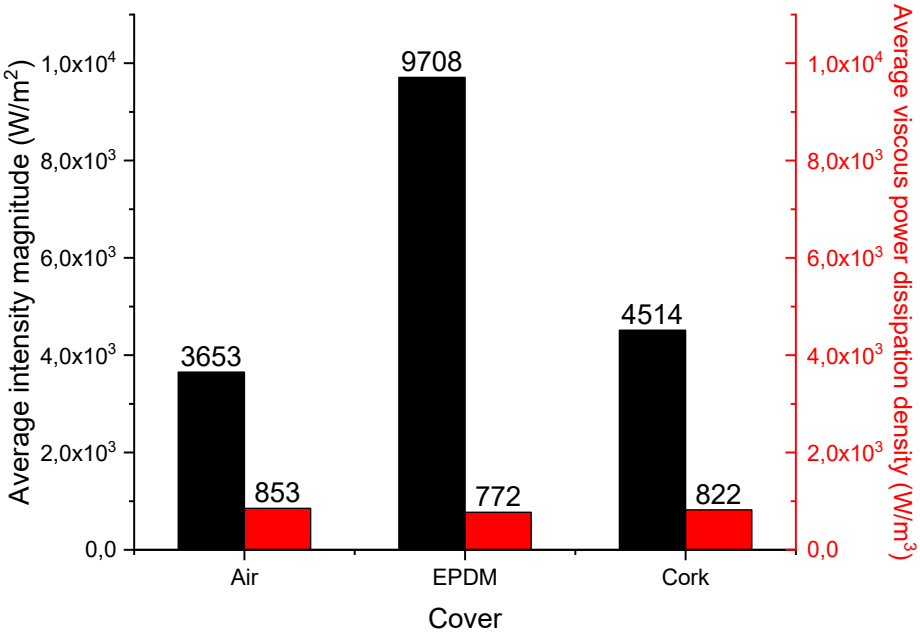

Figure 4.51: Average intensity magnitude (black columns) and power dissipation density (red columns) for the following covers: air, EPDM and cork.

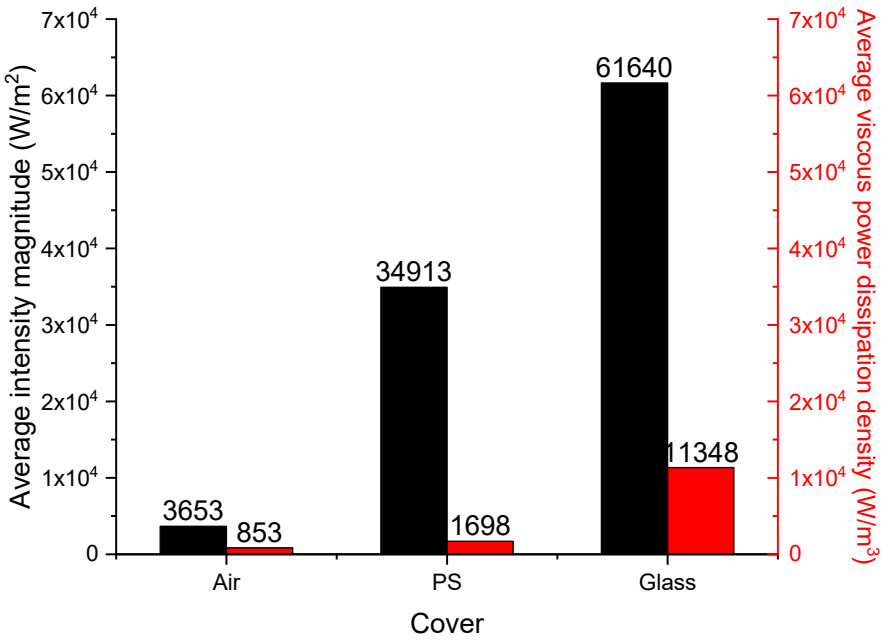

Figure 4.52: Average intensity magnitude (black columns) and power dissipation density (red columns) for the following covers: air, PS and glass.

The covers that mimic air acoustic impedance, namely EPDM and cork, show different results regarding the average intensity (Figure 4.51, black columns), in fact EPDM is characterized by a higher value with respect to cork and air. On the other hand, they share similar values regarding the dissipation density (Figure 4.51, red columns). This result is quite surprisingly, because it seems that EPDM should have better results with respect to air. About this, it should be taken into account that the acoustic characteristics of the EPDM material can be different depending on the composition, and the actual composition of the one used in the laboratory was not clear. For this reason, the average characteristics set in the simulation could have biased the results.

The more rigid covers, namely PS and glass, show very high intensity values with respect to air, but also higher viscous power dissipation density (Figure 4.52), which can be considered, at this point, a crucial element that can influence the acoustic cavitation results. In fact, these two covers were not favourable for the production of ROS and subsequent sonochemiluminescence.

Unfortunately, due to the adiabatic assumption of the model, it was not possible to analyse also the thermal losses and compare them to the temperature measurements previously done. Regarding the viscous dissipation, it emerged as an important parameter and it will surely become more important when the fluid flows will be simulated.

Table 4.16: Additional acoustic characterization for covers simulated in this section.

Cover	Reflection	Transmission	Absorption coefficient (%)
Air	- 1.0	0.0	0.12
EPDM	- 0.6	0.4	67.1
Cork	- 0.9	0.1	20.9
PS	0.2	1.2	94.0
Glass	0.8	1.8	34.2

Finally, an additional acoustic characterization for the interface water-cover studied in this section is exposed in Table 4.16 above: the acoustic reflection and transmission coefficients are taken from Table 4.8, while the absorption coefficient is calculated by the simulation. Table 4.16 shows that air is characterized by very high reflection coefficient (absolute value) and related very low energy absorption, as well as cork. In fact these two materials shared very close results regarding the US field distribution. On the other hand, PS is characterized by a very low reflection and a related very high absorption, which was also detected in the experiments by a high overheating of the cover. EPDM and glass both show quite high reflection coefficient but differences regarding the absorption: in the glass absorption is lower because transmission seems to play an important role. For this last assumption and for the very high intensity values reached when using glass as cover, it could be interesting to study the effect of glass not only as cover, but as container's material. The high transmission of the wave (good for the bottom side of the container), the low energy absorption and good reflection seems to be important for a good US distribution and related acoustic cavitation.

A final consideration should be done regarding the mesh used in these simulations: the size of the elements was not the optimal one for resolving the pressure wave, which for acoustic approaches is usually set dependent to the wavelength. The choice done in this work of a predefined element size, tried to find the best balance between the precision of the results and the computational demand, but for future simulations a better precision could be achieved with the use of a more powerful computer. Furthermore, with the purpose of developing a sort of channel for the treatment of blood, a 2D model could represents a good alternative to the 3D model used in here, leading to a reduction of computational effort and time.

5 Conclusions and future perspectives

The most important conclusions coming from the experiments and the simulations are summarized in this section, with subsequent suggestions for the future developments of the project.

The SCL of Luminol represented a very fast and easy method for a preliminary screening of many experimental set-up. In fact, it permitted to test an already approved cartridge and relative silicon tubes, whose results were not satisfying for the purpose of the project, and for this reason they were abandoned in favour of the polystyrene single well. A deep analysis on the effects of many experimental parameters on the production of ROS in static conditions underlined the importance of the solution volume treated, and related liquid height crossed by the pressure wave: 1 mL (H = 0.5 cm) represents a minimum for the detection of SCL, while 2 mL (H = 1 cm) and 3 mL (H = 1.5 cm) shows the better performances. Even if the SCL could also be observed at 1-cm distance from the transducer (using gel as spacer), the best scenario was represented by the contact with the transducer. Moreover, with the purpose to develop a future cartridge, the bottom thickness of the well (1.7 mm) seemed to be thin enough to be crossed by the US and the material above the solution needed to be carefully chosen because it plays an important role in the reflection or absorption of the wave. The best results were obtained when the solution was in contact with air, which seemed to produce the right conditions for the acoustic cavitation. Following this line, materials that mimic the air acoustic impedance showed good results and they could be used as alternatives to the air. On the other hand, the confinement of the fluid with rigid materials showed disappointing results. Moreover, 1 MHz was confirmed as the optimal US frequency for obtaining SCL.

The EPR technique permitted to validate the results obtained by SCL and to obtain quantitative measurements on the ROS production, in fact the ROS concentration in the well with 2 and 3 mL of solution was between 8 and 10 μM. These results confirmed both the analysis on the commercialized cartridge and the polystyrene single well. Furthermore, they underlined the importance of the same experimental parameters previously emerged and it could be interesting to study their effect on circulating tumour cells, with the development of future in-vitro experiments.

The temperature measurements added information regarding the heating of the sonicated solution, which was in the range 15 – 20 °C: too high values if we consider a future application on living cells, but predictable considering the high US intensities.

Finally, the numerical simulations added some physical information about the pressure wave trend and the energy distribution in the single well environment, which were not possible to understand only from the experiments. It was confirmed that the US wave propagates perpendicular with respect to the transducer surface, with slight perturbations in the central part of the domain when the liquid was in contact with air, which, however, were not problematic for cavitation. The pressure values obtained were in the order of magnitude of MPa units, and they were enough to exceed the cavitation threshold at 1 MHz. Despite this, cavitation was not observed in some experiments, for this reason others physical aspects should be taken into account to better understand the phenomenon. For example, the viscous energy dissipation seems to be an interesting parameter as it showed lower values (~ 800 W/m^3) with soft covers, and higher values (1000 – 11000 W/m^3) using more rigid covers. Moreover, the US intensity resulted concentrated in the centre of the well, and it could reach higher values ($3 – 5 \cdot 10^5$ W/m^2) with respect to the input intensity. These results were important to clarify the effect of variables that influence the acoustic cavitation and the subsequent ROS formation, such as the liquid volume and the reflection of the material above the liquid: positive coefficients generated a regular pressure variation, while the negative ones were related to a distortion of the pressure wave. Finally, the glass emerged as a valid alternative to the PS, for this reason the future experiments could be set for testing this material.

Figure 5.1: SCL in a glass container: container in vertical position and Luminol solution in contact with open air and (left), container in horizontal position and Luminol solution in contact with the air closed inside it (right).

Following what emerged from the simulations results, Figure 5.1 above represents the first future perspective of this project: the testing of acoustic cavitation in glass containers. These

SCL results seem promising and different containers could be tested, with dimensions going from the bigger test tubes to the smaller Pasteur pipettes.

Given the importance of the air in the cavitation results, different geometrical set could be tested: for example using the air in the form of bubbles inside the solution, which could also represent cavitation nuclei helping the process itself; this could be achieved by insufflating air in the sonicated solution.

An important aspect is represented by the NPs used: this Master Thesis only focused on non-functionalized ZnO, even if, for the right targeting of cancer cells, smart and targeted nanoconstruct should be tested, such as the ZnO-NH_2 and lipid-coated ZnO-NH_2 developed by the TrojanNanoHorse Research group, showing high colloidal stability and ability to carry air bubbles thanks to the surface functionalization.

The next most important step should be the passage from static to dynamic conditions. From the experimental point of view, it could be pursued by the coupling of the proper container with a peristaltic pump, where different flow rates could be analysed, in order to understand which is the best one for obtaining cavitation. From the simulations point of view, dynamic conditions could be simulated by the coupling of the pressure interface we used with the interface that can simulate the fluid flows in the container by solving the Navier-Stokes equation.

In conclusion, the present Master Thesis represented a preliminary study for the “XtraUS” project giving the right indications for the development of a future extracorporeal treatment technology.

Acknowledgments

I would like to thank everyone who help me in the realization of this project. First of all an extraordinary thanks to my supervisor Prof. Valentina Alice Cauda for the opportunity to work with her research group and for her guidance along all the development of the project. Then a great thanks also to Prof. Giancarlo Canavese for the very useful suggestions and indications during the experimental work. A great thank must go to all the staff of the TNH Lab for the support and cordiality shown.

Finally a special thanks to my family, for the economic help and the loving support during my university career, and to Laura for being always by my side.

Bibliography

(2020, 11 06). Retrieved from rxlist: https://www.rxlist.com/8-mop-drug.htm#description

(2020, 11 05). Retrieved from BiologyForums: https://biology-forums.com/index.php?PHPSESSID=lducc8ol2n28rur3v49od8p6a5&action=gallery&sa=view&id=1244

Akita, Y. W. (2007). The effect of psoralen plus ultraviolet A in vitro in HUT-78 enhances by 5-aminolevulinic acid. *Photodermatology , photoimmunology & photomedicine* , 23(2-3), 95 97.

Alexandre, F. &. (2010). Circolazione extracorporea. *EMC-Tecniche Chirurgiche-Chirurgia Generale*, 10(1), 1-22.

Apfel, R. E. (1991). Gauging the likelihood of cavitation from short-pulse, low-duty cycle diagnostic ultrasound. *Ultrasound in medicine & biology*, 17(2), 179-185.

Beekers, I. v. (2018). Acoustic characterization of a vessel-on-a-chip microfluidic system for ultrasound-mediated drug delivery. *IEEE transactions on ultrasonics, ferroelectrics, and frequency control*, 65(4), 570-581.

Bennett, M. J.-C. (2013). Oxygen delivery during cardiopulmonary bypass (and renal outcome) using two systems of extracorporeal circulation: a retrospective review. *Interactive cardiovascular and thoracic surgery*, 16(6), 760-764.

Berardi, U. &. (2015). Acoustic characterization of natural fibers for sound absorption applications. *Building and Environment*, 94, 840-852.

Budde, H. K. (2014). Modified extracorporeal photopheresis with cells from a healthy donor for acute graft-versus-host disease in a mouse model. *PloS one*, 9(8), e105896.

Canavese, G. A. (2018). Nanoparticle-assisted ultrasound: a special focus on sonodynamic therapy against cancer. *Chemical Engineering Journal*, 340, 155-172.

Chang, K. Y. (2016). The impact of blood flow rate during hemodialysis on all-cause mortality. *The Korean journal of internal medicine*, 31(6), 1131.

Cheng-Huang Su, H.-I. Y.-Y.-H. (2008). Nonviral Technologies for Gene Therapy in Cardiovascular Research. *International Journal of Gerontology*, 35-47.

Chieregato, K. A. (2015). Evaluation of lymphocytes inactivation by extracorporeal photopheresis using tetrazolium salt based-assay. *Transfusion and Apheresis Science*, 53(2), 242-245.

Cho, A. J. (2018). Extracorporeal Photopheresis—An Overview. *Frontiers in Medicine*, 5, 236.

Corzo, B. A.-H. (2018). Effect of carbon tetrachloride on the luminol sonochemiluminescence reaction kinetics during multibubble cavitation. *Ultrasonics sonochemistry*, 48, 281-286.

Čunderlíková, B. V. (2014). Modification of extracorporeal photopheresis technology with porphyrin precursors. Comparison between 8-methoxypsoralen and hexaminolevulinate hexaminolevulinate in killing human T-cell lymphoma cell lines in vitro. *Biochimica et Biophysica Acta (BBA)-General Subjects*, 1840(9), 2702-2708.

Davies, M. J. (2016). Detection and characterisation of radicals using electron paramagnetic resonance (EPR) spin trapping and related methods. *Methods*, 109, 21-30.

Delaronde-Wilton, G. J. (2008). *U.S. Patent No. 11/662,354.*

Edelson, R. B. (1987). Treatment of cutaneous T-cell lymphoma by extracorporeal photochemotherapy. *New England Journal of Medicine*, 316(6), 297-303.

Edelson, R. L. (1988). Light-activated drugs. *Scientific American*, 259(2), 68-75.

Evrard, B. D. (2010). CFSE flow cytometric quantification of lymphocytic proliferation in extracorporeal photopheresis: use for quality control. *Transfusion and Apheresis Science* , 42(1), 11-19.

Fei, Y. F. (2018). Morphological structure, rheological behavior, mechanical properties and sound insulation performance of thermoplastic rubber composites reinforced by different inorganic fillers. *Polymers*, 10(3), 276.

Gara, S. (2004). *U. S. Patent No. 10/742,343.*

Garban, F. C. (2012). Extracorporeal photopheresis as a curative treatment strategy in non epidermotropic T-cell lymphoma and large granular lymphocyte leukemia. *Annals of oncology*, 23(9), 2386-2390.

Gatza, E. R. (2008). Extracorporeal photopheresis reverses experimental graft-versus-host disease through regulatory T cells. *Blood*, 112(4), 1515-1521.

George, J. F. (2008). Role for CD4+ CD25+ T cells in inhibition of graft rejection by extracorporeal photopheresis. *The Journal of heart and lung transplantation*, 27(6), 616-622.

Golab, H. D.-W. (2007).). Effects of cardiopulmonary bypass circuit reduction and residual volume salvage on allogeneic transfusion requirements in infants undergoing cardiac surgery. *Interactive cardiovascular and thoracic surgery*, 6(3), 335-339.

Goussetis, E. V. (2012). Update on the mechanism of action and on clinical efficacy of extracorporeal photopheresis in the treatment of acute and chronic graft versus host disease in children. *Transfusion and Apheresis Science*, 46(2), 203-209.

Guillermic, R. M. (2019). A PDMS-based broadband acoustic impedance matched material for underwater applications. *Ultrasonics*, 94, 152-157.

Hassell, D. R. (2001). Optimizing dialysis dose by increasing blood flow rate in patients with reduced vascular-access flow rate. *American journal of kidney diseases*, 38(5), 948-955.

Hawass, A. M. (2015). Multi-layer protective armour for underwater shock wave mitigation. *Defence Technology*, 11(4), 338-343.

Hawkins, C. L. (2014). Detection and characterisation of radicals in biological materials using EPR methodology. *Biochimica et Biophysica Acta (BBA)-General Subjects*, 1840(2), 708-721.

Hickey, E. K. (2006). Effects of circuit miniaturization in reducing inflammatory response to infant cardiopulmonary bypass by elimination of allogeneic blood products. *The Annals of thoracic surgery*, 81(6), S2367-S2372.

Horvath, J. S. (1994). Expanded polystyrene (EPS) geofoam: an introduction to material behavior. *Geotextiles and Geomembranes*, 13(4), 263-280.

Iperen, H. V. (1993). An animal model and new photosensitizers for photopheresis. *Photochemistry and photobiology*, 58(4), 571-574.

Ippoliti, F. P. (2019). Comparative spallation performance of silicone versus Tygon extracorporeal circulation tubing . *Interactive cardiovascular and thoracic surgery*, 29(5), 685-692.

Jacob, M. C. (2003). Quality control for the validation of extracorporeal photopheresis process using the Vilbert–Lourmat UV-A irradiation's system. *Transfusion and apheresis science*, 28(1), 63-70.

Judson, G. T. (1970). *Washington, DC: U.S Patent No. 3,489,145.*

Junior, F. U. (2017). Does the roller pump adjustment in cardiopulmonary bypass settings influence hemolysis? *The International journal of artificial organs*, 40(3), 118-122.

Kauer, M. B.-M. (2017). Visualization and optimization of cavitation activity at a solid surface in high frequency ultrasound fields. *Ultrasonics sonochemistry*, 34, 474-483.

Kim, H. J. (2009). Effect of ultrasound irradiation on solvent extraction process. *Journal of Industrial and Engineering Chemistry*, 15(6), 919-928.

Klassen, J. (2010). The role of photopheresis in the treatment of graft-versus-host disease. *Current Oncology*, 17(2), 55.

Klima, J. F.-F.-G. (2007). Optimisation of 20 kHz sonoreactor geometry on the basis of numerical simulation of local ultrasonic intensity and qualitative comparison with experimental results. *Ultrasonics sonochemistry*, 14(1), 19-28.

Knobler, R. &. (2003). Extracorporeal photochemoimmunotherapy in cutaneous T-cell lymphoma. *Transfusion and apheresis science*, 28(1), 81-89.

Knobler, R. B. (2009). Extracorporeal photopheresis: past, present, and future. . *Journal of the American Academy of Dermatology*, 61(4), 652-665.

Knobler, R. B.-P. (2014). Guidelines on the use of extracorporeal photopheresis. . *Journal of the European Academy of Dermatology and Venereology*, 28, 1-37.

Lakatos, Á. &. (2013). Investigation of thickness and density dependence of thermal conductivity of expanded polystyrene insulation materials. *Materials and structures*, 46(7), 1101-1105.

Laulhé, M. L.-R. (2019). A standardized methodical approach to characterize the influence of key parameters on the in vitro efficacy of extracorporeal photopheresis. *Plos one*, 14(3), e0212835.

Lee, K. H. (1988). *Washington, DC: U.S. Patent No. 4,737,140.*

Lin, E. C. (2018). Circulating tumor cells: diagnostic and therapeutic applications. *Annual review of biomedical engineering*, 20, 329-352.

Louisnard, O. (2012). A simple model of ultrasound propagation in a cavitating liquid. Part I: Theory, nonlinear attenuation and traveling wave generation. *Ultrasonics sonochemistry*, 19(1), 56-65.

Luo, S. T. (2015). A novel minimal invasive mouse model of extracorporeal circulation. . *Mediators of inflammation*.

Maeda, A. S. (2005). Intravenous infusion of syngeneic apoptotic cells by photopheresis induces antigen-specific regulatory T cells. *The Journal of Immunology*, 174(10), 5968-5976.

McMurray, H. N. (1999). Mechanistic and spatial study of ultrasonically induced luminol chemiluminescence. *The Journal of Physical Chemistry A*, 103(20), 3955-3962.

Misra, M. (2005). The basics of hemodialysis equipment. *Hemodialysis International*, 9(1), 30-36.

Muller, P. B. (2012). A numerical study of microparticle acoustophoresis driven by acoustic radiation forces and streaming-induced drag forces. *Lab on a Chip*, 12(22), 4617-4627.

Murphy, G. S. (2009). Optimal perfusion during cardiopulmonary bypass: an evidence-based approach. *Anesthesia & Analgesia*, 108(5), 1394-1417.

Mustieles, M. J. (2020). Peripheral venous access devices for apheresis: 16-gauge is not always needed. *Transfusion*, 60(3), 607-612.

Neppiras, E. A. (1980). Acoustic cavitation. *Physics reports* , 61(3), 159-251.

Perotti, C. &. (2015). A concise review on extracorporeal photochemotherapy: Where we began and where we are now and where are we going! *Transfusion and Apheresis Science*, 52(3), 360-368.

Piccirillo, N. P. (2018). Mononuclear cell collection for extracorporeal photopheresis: Concentrate characteristics for off-line UV-A irradiation procedure. *Journal of clinical apheresis*, 33(3), 217-221.

Piccirillo, N. P. (2019). Inline extracorporeal photopheresis: evaluation of cell collection efficiency. *Transfusion*, 59(12), 3714-3720.

Racca, L. L. (2020). Zinc Oxide Nanocrystals and High-Energy Shock Waves: A New Synergy for the Treatment of Cancer Cells. *Frontiers in Bioengineering and Biotechnology*, 8, 577.

Rafik, H. A. (2018). The impact of blood flow rate on dialysis dose and phosphate removal in hemodialysis patients. *Saudi Journal of Kidney Diseases and Transplantation*, 29(4), 872.

Rangarajan, H. G. (2013). The use of novel Therakos™ Cellex® for extracorporeal photopheresis in treatment of graft-versus-host disease in paediatric patients. *British journal of haematology*, 163(3), 357-364.

Ravagli, E. &. (2018). Optical and electrical characterization of biocompatible polymeric lines for hemodialysis applications. *Materials*, 11(3), 438.

Rawles, T. A. (2007). *Washington, DC: U.S. Patent No. 7,291,124.*

Rivas, D. F. (2012). Sonoluminescence and sonochemiluminescence from a microreactor. *Ultrasonics sonochemistry*, 19(6), 1252-1259.

Rooze, J. R. (2011). Effect of resonance frequency, power input, and saturation gas type on the oxidation efficiency of an ultrasound horn. *Ultrasonics sonochemistry*, 18(1), 209-215.

Sabri, F. S. (2013). In vivo ultrasonic detection of polyurea crosslinked silica aerogel implants. *PloS one*, 8(6), e66348.

Saez, V. F.-F.-G. (2005). Chacterization of a 20 kHz sonoreactor. Part I: analysis of mechanical effects by classical and numerical methods. *Ultrasonics sonochemistry*, 12(1-2), 59-65.

Santambrogio, L. L. (2009). Determination of pump flow rate during cardiopulmonary bypass in obese patients avoiding hemodilution. *Journal of cardiac surgery*, 24(3), 245-249.

Sarkar, M. &. (2017). Basics of cardiopulmonary bypass. *Indian journal of anaesthesia*, 61(9), 760.

Schooneman, F. (2003). Extracorporeal photopheresis technical aspects. . *Transfusion and apheresis science*, 28(1), 51-61.

Serrick, C. J. (2003). Quality of red blood cells using autotransfusion devices: a comparative analysis. *Journal of Extracorporeal Technology*, 35(1), 28-34.

Shao, Z. W. (2010). Numerical simulation of standing waves for ultrasonic purification of magnesium alloy melt. *Transactions of Nonferrous Metals Society of China*, 20, s382-s387.

Shibaguchi, H. T. (2011). Sonodynamic cancer therapy: a non-invasive and repeatable approach using low-intensity ultrasound with a sonosensitizer. *Anticancer research*, 31(7), 2425-2429.

Skov, N. R. (2019). 3D modeling of acoustofluidics in a liquid-filled cavity including streaming, viscous boundary layers, surrounding solids, and a piezoelectric transducer. *Aims Mathematics*, 4(1), 99-111.

Spigarelli, L. V. (2020). Numerical study of the effect of channel aspect ratio on particle focusing in acoustophoretic devices. *Scientific reports*, 10(1), 1-11.

Swift, A. L. (2019). Strategies to avoid intraoperative blood transfusion. *Anaesthesia & Intensive Care Medicine*, 20(3), 142-146.

Takagi, Y. H. (2007). Relaxation of polystyrene near the glass transition temperature studied by acoustic measurements. *Journal of the Physical Society of Japan*, 76(2), 024604.

Taverna, F. C. (2015). Biological quality control for extracorporeal photochemotherapy: Assessing mononuclear cell apoptosis levels in ECP bags of chronic GvHD patients. *Journal of Clinical Apheresis*, 30(3), 162-170.

Tiong, T. J. (2017). Comparison of sonochemiluminescence images using image analysis techniques and identification of acoustic pressure fields via simulation. *Ultrasonics sonochemistry*, 36, 78-87.

Tsou, J. K. (2008). Role of ultrasonic shear rate estimation errors in assessing inflammatory response and vascular risk. *Ultrasound in medicine & biology*, 34(6), 963-972.

Tudela, I. S.-G.-G. (2014). Simulation of the spatial distribution of the acoustic pressure in sonochemical reactors with numerical methods: a review. *Ultrasonics sonochemistry*, 21(3), 909-919.

Vighetto, V. A. (2019). The synergistic effect of nanocrystals combined with ultrasound in the generation of reactive oxygen species for biomedical applications. *Frontiers in Bioengineering and Biotechnology*, 7, 374.

Vyas, N. M. (2019). Which parameters affect biofilm removal with acoustic cavitation? A review. *Ultrasound in medicine & biology*, 45(5), 1044-1055.

Wang, X. J. (2012). Comparison of the effects of three cell saver devices on erythrocyte function during cardiopulmonary bypass procedure—a pilot study. *Artificial organs*, 36(10), 931-935.

Warnock, D. F. (1982). Modification of the Haemonetics Cell Saver for optional high flow rate autotransfusion. *The American Journal of Surgery*, 143(6), 765-768.

Wiesenack, C. L. (2004). Four years' experience with a miniaturized extracorporeal circulation system and its influence on clinical outcome. *Artificial organs*, 28(12), 1082-1088.

Wippermann, J. A. (2005). Comparison of minimally invasive closed circuit extracorporeal circulation with conventional cardiopulmonary bypass and with off-pump technique in CABG patients: selected parameters of coagulation and inflammatory system. *European journal of cardio-thoracic surgery*, 28(1), 127-132.

Xu, G. N. (2020). Acoustic Characterization of Polydimethylsiloxane for Microscale Acoustofluidics. *Physical Review Applied*, 13(5), 054069.

Yarham, G. C. (2011). Evaluating the 'next generation'of cell salvage-will it make a difference? *Perfusion*, 26(4), 263-270.

Yasui, K. K. (2007). FEM calculation of an acoustic field in a sonochemical reactor. *Ultrasonics sonochemistry*, 14(5), 605-614.